Ultracold atoms in optical lattices

A thesis submitted in partial fulfilment of

the requirements for the degree of

Doctor of Philosophy

by

Deepak Gaur

(Roll No. 18330008)

Under the supervision of

Prof. Angom Dilip Kumar Singh

Department of Physics, Manipur University, India

and Programme supervisor

Prof. Navinder Singh

Theoretical Physics Division

Physical Research Laboratory, Ahmedabad, India

DEPARTMENT OF PHYSICS

INDIAN INSTITUTE OF TECHNOLOGY GANDHINAGAR

2023

Dedicated to

My beloved parents and family,

for your unconditional love and support

Declaration

I declare that this written submission represents my ideas in my own words and where others' ideas or words have been included, I have adequately cited and referenced the original sources. I also declare that I have adhered to all principles of academic honesty and integrity and have not misrepresented or fabricated or falsified any idea/data/fact/source in my submission. I understand that any violation of the above will be cause for disciplinary action by the Institute and can also evoke penal action from the sources which have thus not been properly cited or from whom proper permission has not been taken when needed.

Deepak Gaur
30/05/2024

Signature

Name: Deepak Gaur

(Roll No: 18330008)

CERTIFICATE

It is certified that the work contained in the thesis entitled **Ultracold atoms in optical lattices** by Mr. Deepak Gaur (Roll No. 18330008), has been carried out under my supervision and that this work has not been submitted elsewhere for a degree.

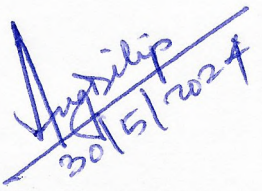

Prof. Angom Dilip Kumar Singh
Department of Physics,
Manipur University ,
Canchipur - 795003,
Manipur, India.
(Thesis Supervisor)

Acknowledgments

I would like to express my deepest gratitude to the numerous individuals and organizations who have played a pivotal role in the completion of this Ph.D. thesis. This research endeavor has been a challenging yet immensely rewarding journey, and I am profoundly thankful for the support and encouragement I have received along the way. I take this opportunity to express my sincere acknowledgements to them.

First and foremost, I extend my heartfelt appreciation to my academic supervisor Prof. Angom Dilip Kumar Singh, whose unwavering guidance, scholarly insights, and valuable teachings have been instrumental throughout this research. Your mentorship has not only enriched my academic experience but also shaped me into a better researcher.

Within Dilip's group, we have fostered a bond that extends beyond the academics, and blossoms into a friendship akin to family. I am deeply indebted to my immediate seniors in the group - Hrushi, Soumik and Rukmani - despite your busy schedule, you have always accommodated lengthy time for me, be it scientific discussions or patiently listening to the hurdles in my life. I cherish our time together working in the same group. Even after leaving the group for your future academic journey, I feel extremely happy that we are still bonded in same way. Soumik and Rukmani, you have taught me various numerical codes and endowed me with the computational and academic writing skills. With Hrushi, I have shared most of my office time with valuable discussions on my research problems. The constant access to you for exchange of ideas have been a great boon to me. To be frank, I never felt a senior-junior relationship but like a friend open to all kind of discussions. I am also thankful to my seniors Kuldeep Suthar, Sukla Pal, Arko Roy and Sandeep Gautam; for valuable ideas and suggestions into my research problems.

I express my sincere gratitude to my programme supervisor Prof. Navinder Singh for your guidance and insightful recommendations that helped me gaining a wealth of knowledge. I would also like to thank my DSC members - Prof. Namit Mahajan, Dr. Ketan Patel, and Dr. Ramitendranath Bhattacharyya, for their invaluable feedback. The interactions and discussions with them have been immensely beneficial to my research journey.

I wish to convey my appreciation for the assistance I've received from PRL. My heartfelt gratitude goes to the Department of Space, Government of India, for their generous research grant that sustained my tenure at PRL. Additionally, I would like to express my sincere thanks to Prof. Anil Bhardwaj, the Director of PRL, for his unwavering support in ensuring access to top-notch research facilities. I am deeply indebted to the High-Performance Computing facility at PRL - the Vikram-100 and the Param Vikram-1000 HPC cluster facility and the CNIT team members for their diligent support. Special thanks to of Mr. Jigar Raval and Mr. Bhavin whose exceptional expertise in HPC matters have helped me a lot. I am grateful to the Dean Academic affairs, the Head Academic Services for providing me the necessary administrative and academic support over the years at PRL. I extend my thanks to Nishtha Ma'am and the other library staff for efficiently managing the library, handling book grants, and managing journal subscriptions. I sincerely appreciate Dr. Bhushit Vaishnav, the head of academics, for his invaluable support in academic matters. I would like to express my gratitude to the medical staffs at PRL - Dr. Samir Dani, Dr. Sheetal Patel and their team. I am also grateful to the canteen staff, the CMG group, the security group and the house-keeping staff. Thank you Richa ma'am for taking care a lot of student related matters.

I am grateful to the faculties of the Theoretical Physics Division - Prof. H. Mishra, Prof. S. Meant, Prof. J. Bhatt, Prof. S. Goswami, Prof. N. Mahajan, Prof. P. Konar, Dr. K. Patel, Dr. P. Dutta, Dr. S. Seth, for providing me such a nice working research environment. I have enjoyed discussions and participations in various departmental activities with - Dr. A. Chatterjee, Anshika, Vishal, Pravin, Sourav, Soumita, Debashis Saha, Dayanand, Anupam, Supriya, Bharathiganesh, Saurabh, Debashis Pachhar, Gurucharan, Deepanshu. I appreciate interactions with Prof. Rejish Nath, Prof. Subroto Mukerjee, Dr. Salman Silotri, Prof. Brajesh Mani, Prof. B. Prasanna Venkatesh and Prof. Udaysinh Bhosale during my Ph.D. tenure. I express my gratitude to Prof. Barbara Capogrosso-Sansone for providing the QMC data used in the Thesis.

Life is truly a joyful and lively journey when accompanied by friends. To start with I thank Vibhor, Nirmal, Sunil, Vikas, Yogesh, Daya, Raja ji - you are on my speed-dial list with whom I have shared a tonn of conversations during this journey. Thank you

batch of 2018 - Monika, Akansha, Naval, Namita, Yash, Arijit, Sandeep, Pranav, Anju, Siddhartha, Rai, Deva, Sanjeet, Supriyo, Anupam, for being a part of this research journey. This team has been always present in times of need. We share a lot of joyful moments which will last forever. I thank my fellow seniors and juniors - Priyank, Harish, Ritu, Shivani, Abhay, Sushant, Sana, Madhu, Parta, Shawlee, Ojha ji, Birendra, Saumya, Himanshu, Aravind, Rithvik, Vipin, Rekha, Shreya, Tanya, Vardaan, Wafikul, Priya bhabhi, Kittu Santunu, Mallika, Kartika, Sukumar - for making this place feel homely. Thanks to Pardeep, Dani, Vasu, Suraj, Palki, Kohenjit, Laxmi, Bhumika and Momin with whom I have shared some vacational trips during academical visits. A special heartfelt thanks to Meghna, for offering hand-cooked tasty meals frequently. Together I have learnt valuable cooking lessons. You have been my emotional support during unpleasant times. Thank you for being a constant factor on which I can count on anytime. You have made these years a memorable journey.

I cannot express sufficient gratitude to my family members for their boundless and unwavering love, as well as their unwavering support throughout my academic journey. To my dear parents, Mummy and Papa, you have consistently been my most significant pillars of strength. Thank you for putting your constant faith in me, despite the outcomes. I also want to extend my heartfelt thanks to Suman Di and Sumit Jiju, Neeraj Bhai and Himani Bhabhi, and Ankit for their unconditional love and blessings. Your support has been a constant stream of power during this journey. Special shout-out to the little ones, Shristu, Kannu and Trinay baby, with all my love.

Deepak

Abstract

The exploration of the quantum phases of ultracold quantum gases have emerged as one of the contemporary pursuits in the realm of condensed matter physics. This is motivated by the emergence of novel phases of matter at these extreme conditions. For bosonic quantum gases, the remarkable phenomenon of Bose-Einstein condensation occurs when cooled to quantum degeneracy. This phenomenon is characterized by the macroscopic occupation of the lowest energy single-particle state. More importantly, the physics of strongly interacting regime can be probed when the ultracold atoms are confined in optical lattices. These engineered systems are clean, have minimal interaction with the surroundings, and allows unprecedented control over the system parameters in experiments. In particular, the experimental progress and control in introducing artificial gauge fields have made these systems ideal candidates for probing certain topological quantum phases. An example is the fractional quantum Hall (FQH) effect. These phases are of interest for potential applications in quantum technologies.

In this thesis, we present an exact diagonalization method we have developed and is well suited to study ultracold atoms in optical lattices. The method is apt for soft-core bosons, and to implement constraints for reducing the basis set size. In addition, with minimal changes, it can be modified to cluster mean-field method. In this thesis, we have investigated and characterized the FQH states using these methods. We model the system using the Bose-Hubbard model (BHM) with appropriate complex hopping terms. We show that the $\nu = 1/2$ FQH state emerges as the ground state. We identify the state using the two-point correlation function, and the topological order is verified by calculating the many-body Chern number. In addition, we find that the spatial bipartite entanglement entropy follows the area law, and calculate the topological entanglement entropy. We find that the long-range interaction preserves the FQH state and stabilizes it from the competing metastable phases.

We also investigate the non-equilibrium dynamics that ensue when a parameter of the Hamiltonian is quenched across a quantum phase transition (QPT). We, in particular, focus on the quench dynamics across the Mott-insulator to superfluid QPT of the BHM by quenching the hopping strength for constant chemical potential at the tip of the Mott lobe and below it. Using this, we study the validity of Kibble-Zurek mecha-

nism (KZM). It is related to the critical slowing down near the critical point of a continuous phase transitions, leading to the breakdown of adiabaticity. The KZM predicts a universal power-law nature of specific quantities, such as the correlation length and the number of defects generated in the quench across the spontaneous symmetry-breaking transition. We have studied the quench dynamics with the single-site Gutzwiller mean-field and cluster Gutzwiller mean-field methods and calculate the exponents of the power-law scalings. We notice that the critical exponents obtained from these studies are close to the equilibrium values. The critical exponent associated with the divergence of the system's characteristic time approaches the equilibrium value with larger cluster sizes.

Abbreviations

2D	Two-dimensional
BEC	Bose-Einstein condensate
BHM	Bose-Hubbard model
CGMF	Cluster Gutzwiller mean-field
eBHM	Extended Bose-Hubbard model
ED	Exact diagonalization
FQH	Fractional quantum Hall
GP	Gross-Pitaevskii
IQH	Integer quantum Hall
KZ	Kibble-Zurek
KZM	Kibble-Zurek mechanism
MBCN	Many-body Chern number
MI	Mott insulator
NN	Nearest neighbor
PBC	Periodic boundary conditions
QH	Quantum Hall
QMC	Quantum Monte-Carlo
QPT	Quantum phase transition
SF	Superfluid
SGMF	Single Site Gutzwiller mean-field
TPC	Two-point correlation

Contents

List of Figures

List of Tables

Chapter 1

Introduction

The novel experimental advances in laser cooling and trapping techniques have led to the experimental achievement of Bose-Einstein condensation in dilute atomic gas of bosonic alkali atoms in 1995 [1–3]. This remarkable milestone was honored with the 2001 Nobel Prize in physics and led to other experiments for realizing Bose-Einstein condensates (BECs) with different atoms [4–6]. The BEC is a state of matter arising from the macroscopic occupation of the bosonic particles in the lowest single-particle state of the system. The realization of BECs in experiments has opened a new frontier for investigating the quantum many-body physics at a macroscopic scale in the laboratories [7–12]. The BECs are created in experiments by cooling the dilute atomic gases close to zero temperature with a typical density of $10^{13} - 10^{15}$ atoms per cm^{-3}. The ultralow density suppresses three-body collisions and prevents solidification of the gas. The low density, however, also implies weak inter-atomic interactions and limits the experimental investigations to the weakly-interacting regime. Nevertheless, the strongly interacting regime is accessible when BECs are loaded in the optical lattices. The optical lattices are periodic potentials of light formed by interference of counter-propagating laser beams. This allows for the study of strongly interacting quantum many-body phases like the Mott-insulator [13, 14]. These quantum phases and the associated quantum phase transitions have been observed in the experiments with optical lattices [15]. The ultracold atoms trapped in optical lattice resemble the quantum many-body system of electrons in a periodic lattice potential or condensed matter systems. In addition, these systems are clean, free from defects and allow superb control

over several system parameters. This makes these systems excellent proxies to study various phenomena in condensed matter systems. They have been used to study novel quantum phases like the supersolid phase [16–19], the physics of phase separation in binary mixtures [20–22], and collective excitations [23, 24], to name a few. Ultracold atoms are, however, charge neutral and hence lack the effect of Lorentz force arising from external electromagnetic fields. This shortcoming can be remedied with the implementation of artificial gauge fields in optical lattices [25, 26]. With this, the physics emerging from the Lorentz force can be simulated, and topological states like quantum Hall (QH) can be explored with ultracold atoms in optical lattices. The QH states are of immense importance due to the robustness of the state protected by symmetry. Observing these states require very low temperatures and high magnetic fields, making it difficult to observe the QH states associated with high flux in condensed matter systems. High magnetic flux can be realized with the optical lattices, which makes them good candidates to observe novel QH states. Recently, $\nu = 1/2$ bosonic fractional quantum Hall state has been experimentally realized with ultracold atoms in the optical lattice [27]. This remarkable realization opens the door to the creation of other QH states.

In this chapter, we begin with a brief discussion of the classical and quantum Hall effects. This is followed by studies of bosonic QH states with ultracold atoms in optical lattices. Finally, towards the end of the chapter, we discuss the non-equilibrium dynamics following a parameter change in the Hamiltonian, which drives these systems across the Mott insulator to superfluid QPT.

1.1 Classical Hall effect

The Hall effect is a phenomenon which occurs when a two-dimensional (2D) electron gas is placed in a perpendicular magnetic field, and a current flows along the plane. This results in the development of a transverse voltage, called the Hall voltage, perpendicular to both the magnetic field and the current. The Hall resistivity, defined as the Hall voltage per unit longitudinal current, varies linearly with the strength of the magnetic field, while the diagonal resistivity is zero. This behaviour was first discov-

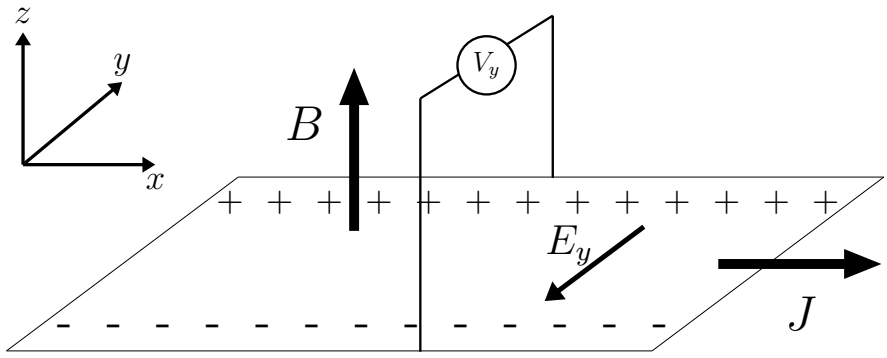

Figure 1.1: A schematic illustration of the classical Hall effect for electrons confined in a 2D $xy-$ plane. The current J flowing along x direction, under a perpendicular magnetic field B, generates transverse electric field E_y and the Hall voltage V_y.

ered by Edwin Hall in 1879 and is known as the classical Hall effect [28]. The classical physics explains this effect as a consequence of the cyclotronic motion of the electrons under the Lorentz force.

Consider an electron gas restricted in the 2D $xy-$ plane and subjected to an external magnetic field $\mathbf{B} = B\hat{z}$ perpendicular to the plane. Let a constant current $\mathbf{I} = I\hat{x}$ flow along the longitudinal direction, then the magnetic field induces a voltage along the transverse y direction. A schematic illustration of this phenomenon is shown in Fig. 1.1. This phenomenon or the Hall effect, can be explained using classical physics with the electronic motion governed by the Lorentz force

$$m\frac{d}{dt}\mathbf{v} = -e(\mathbf{E} + \mathbf{v} \times \mathbf{B}). \tag{1.1}$$

Here m, e are the mass and charge of the electron, respectively, and $\mathbf{v}$ and $\mathbf{E}$ represent the electron velocity and the electric field, respectively. The steady state solution corresponding to $\dot{\mathbf{v}} = 0$ gives a constraint $\mathbf{E} = -\mathbf{v} \times \mathbf{B}$. Assuming ρ_0 as the equilibrium density of electrons, the current density defined by $\mathbf{J} = -e\rho_0\mathbf{v}$ for the steady state becomes

$$J_x = -\frac{e\rho_0}{B}E_y, \text{ and } \quad J_y = \frac{e\rho_0}{B}E_x. \tag{1.2}$$

Thus, a current along the x-direction is deflected and bends along the y-direction due to the magnetic field. This results in the piling up of electrons along the edges in the finite y-direction with an electric field E_y. The electric field E_y keeps growing till it cancels

the bending due to the magnetic field. The associated voltage along the y-direction is the Hall voltage. The Hall resistivity is defined as

$$\rho_{xy} \equiv \frac{E_y}{J_x} = \frac{B}{e\rho_0}, \tag{1.3}$$

is linearly proportional to the external magnetic field B. The longitudinal resistivity $\rho_{xx} \equiv E_x/J_x = 0$ in the above calculations. Considering the effects of electronic collisions with the lattice or impurities as described by the Drude model with a scattering term, the Hall resistivity is still given by Eq. (1.3). However, the longitudinal resistivity is now modified as $\rho_{xx} = m/(e^2\rho_0\tau)$, with τ being the mean free time.

A century later, in the year 1980, the experiments by Klitzing, Dorda and Pepper led to the discovery of plateaus in the plot of Hall resistivity against the magnetic field [29]. The Hall resistivity at these plateaus corresponded to the integer multiples of e^2/h. The integral quantization of the Hall resistivity can be explained by treating the electrons as quantum objects described by quantum mechanics. This effect was subsequently known as the integer quantum Hall (IQH) effect. Soon after, in 1982 Tsui, Stormer, and Gossard discovered the quantization of Hall resistivity at fractional multiples of e^2/h [30]. This effect is known as the fractional quantum Hall (FQH) effect. The basic requirement to explain the FQH effect is the electronic correlations, which is not required to explain the IQH effect. Fig. 1.2 shows the plateaus in Hall resistivity for various integer and fractional quantum Hall states.

1.2 Quantum Hall effect

The quantum Hall (QH) effect is the quantization of the Hall resistivity with strong magnetic fields at very low temperatures. At such temperatures, the quantum effects become prominent, and the electrons can't be treated as classical particles. Thus, a quantum mechanical treatment of the electrons is essential. The Hamiltonian for a free electron moving in a 2D plane under an external perpendicular magnetic field is given by

$$H = \frac{1}{2m}(\mathbf{p} + e\mathbf{A})^2. \tag{1.4}$$

Here, $\mathbf{p} = -i\hbar\nabla$ is the momentum operator, and $\mathbf{A}$ is the vector potential satisfying $\nabla \times \mathbf{A} = B\hat{z}$. In the Landau gauge, $\mathbf{A} = Bx\hat{y}$, the translation symmetry along y-

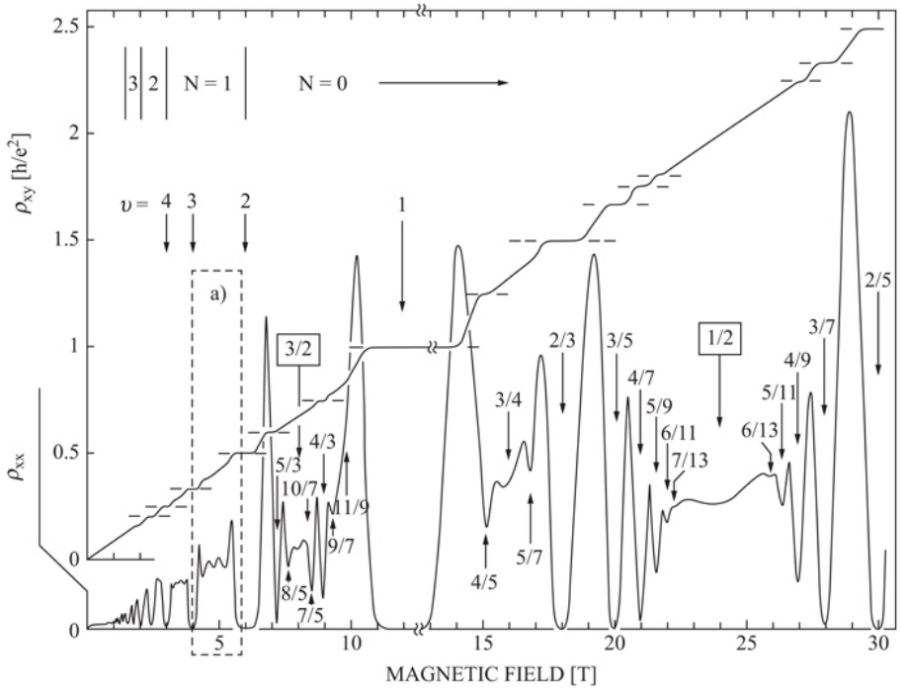

Figure 1.2: The Hall resistivity ρ_{xy} shows plateaus at various integer and fractional filling factors ν, with simultaneous vanishing of the diagonal resistivity ρ_{xx}. Plateaus at integer and fractional values of ν correspond to the integer quantum Hall and fractional quantum Hall states, respectively. Reprinted figure from [Willett *e*t al., PRL **59**, 1776 (1987).] Copyright © 1987, American Physical Society.

direction is respected. So along y, the plane waves are the required solutions. We thus consider the eigenfunctions of Hamiltonian in Eq. (1.4) of form $\Psi_k(x,y) = e^{iky}\psi_k(x)$ with

$$H\Psi_k(x,y) = \frac{1}{2m}\left[p_x^2 + (\hbar k + eBx)^2\right]\Psi_k(x,y) \equiv H_k\Psi_k(x,y). \tag{1.5}$$

The Hamiltonian H_k resembles the Hamiltonian of a 1D harmonic oscillator, but with a shifted centre

$$H_k = \frac{p_x^2}{2m} + \frac{m\omega_c^2}{2}(x + kl_B^2)^2. \tag{1.6}$$

Here, $\omega_c = eB/m$ is the cyclotron frequency, and $l_B = \sqrt{\hbar/(eB)}$ represents a characteristic length scale, called the magnetic length. The energy eigenvalues of the system, referred to as Landau levels, is given by

$$E_n = \left(n + \frac{1}{2}\right)\hbar\omega_c, \quad n \in \{0, 1, 2, \cdots\}. \tag{1.7}$$

The Landau levels are highly degenerate. Each state is BA/Φ_D fold degenerate; here, $\Phi_D = 2\pi\hbar/e$ is the Dirac flux quanta, and A is the area of the system. The degeneracy is thus equal to the total number of flux quanta in the system. With this concept of Landau levels, let us see how the integer quantization of Hall resistivity can be understood.

1.2.1 Integer quantum Hall effect

Experimentally, the IQH effect is observed at quantized values of Hall resistivity [29], given by

$$\rho_{xy} = \frac{1}{\nu}\frac{2\pi\hbar}{e^2}, \quad \nu \in \{1, 2, 3, \cdots\}. \tag{1.8}$$

Comparing this with the classical Hall resistivity in Eq. (1.3), we get $\rho_0 = \nu B/\Phi_D$, which suggests completely filled ν Landau levels. The quantity $\nu = \rho_0\Phi_D/B$ represents the filling factor of the state. Thus, the IQH effect at filling ν is observed when ν Landau levels are completely filled. At fixed electron density, this will occur at special values of magnetic field. In experiments, the IQH is observed as plateaus for a range of magnetic field values [29]. The origin of these plateaus is ascribed to the role of impurities in the system. The weak disorder effects broaden the Landau levels and turn many of the states at the far edge of the bands to localized states. The IQH effect corresponds to the plateaus in the Hall resistivity at integer values of filling factor ν. However, in the experiments, various plateaus are observed for the Hall resistivity with vanishing longitudinal resistivity at fractional values of ν as shown in Fig. 1.2. This is the FQH effect which arises due to the electronic correlations.

1.2.2 Fractional quantum Hall effect

The FQH plateaus for $\nu = 1/3$ and $2/3$ were the first ones to be observed in experiments. Later, various other plateaus were observed for $\nu = 1/5$, $2/5$, $3/7$, $4/9$, $\cdots$, $4/3$, $5/3$, $7/5$, $5/2$, $12/5$, $\cdots$ in the lowest and higher Landau levels [31]. In the presence of the inter-electron electrostatic interaction, the macroscopic degeneracy of the Landau levels is lifted and also broadens the levels. It can, then, open spectral gaps at fractional values of ν [32, 33]. Weak disorder effects can then in-

troduce localized states in the gap, which is responsible for the observed plateaus in Hall resistivity. Thus, for the FQH effect, the various energy scales follow the hierarchy $\hbar\omega_c \gg E_{\text{Coulomb}} \gg V_{disorder}$. Although a complete theoretical understanding of the FQH effect is lacking, various theories which capture the relevant physics of the FQH effect have been proposed. The first theoretical explanation of the FQH effect at $\nu = 1/m$ for odd m was given by Laughlin in 1983 based on the many-body wavefunction proposed based on physical insights [32]. Another theory based on the concept of composite fermions was proposed by Jainendra Jain in 1989 [33]. With this, the FQH effect of electrons can be understood as the IQH effect for composite fermions. The excitations of FQH states are anyons and possess fractional electronic charge. The quantum statistics for anyons is different from the Bose-Einstein statistics obeyed by bosons or the Fermi-Dirac statistics obeyed by fermions.

This covers a brief theoretical background on the quantum Hall effect. As previously discussed, the observation of QH states requires very low temperatures, and a very high magnetic flux is required for the $\nu < 1$ FQH states. Because of this and various other advantages, ultracold atoms in optical lattices are excellent systems for studying the QH effect. Various theoretical studies exist for the realization of bosonic IQH states with the optical flux lattice [34], with correlated hopping on honeycomb lattice [35] and with interacting two-component bosons [36]. The investigations on realization of bosonic FQH states have gained wider attention. In the next section, we describe the ultracold atoms in optical lattice and discuss some of the previous studies of FQH states in these systems.

1.3 Ultracold atoms in optical lattice

Optical lattices are periodic potentials of light synthesized by the interference of counter-propagating lasers. Due to the atom-light interaction, the ultracold gas exposed to lasers develops an induced dipole moment, leading to a periodic potential due to the AC-Stark shift. The lasers are chosen to be red-tuned, thus avoiding the dissipations arising from the absorption of photons by the condensed atoms. In this setting, the atoms occupy the minima of the potential. The depth of the potential well is propor-

tional to the intensity of the laser. The atoms are trapped around the potential well, thus forming a lattice with the lattice constant proportional to the wavelength of the laser. Various lattice geometries like the honeycomb, triangular, kagome lattices can be synthesized by tuning the angle between the counter-propagating lasers [37–42]. Additionally, by employing an additional set of lasers in orthogonal directions, the dimensionality of the lattice can be changed. The ability to control the inter-atomic interactions, number of atoms and systematic introduction of defects in an otherwise clean environment offers great experimental tunability. As discussed earlier, the strongly interacting regime can be accessed by reducing the itinerancy of the atoms. This is possible by increasing the depth of the potential well, leading to a localized Mott insulator (MI) phase. In the opposite limit, a completely delocalized coherent superfluid (SF) phase exists. These two quantum phases are separated by a QPT and have been observed in the experiments [15, 43]. Theoretically, the system can be described by the Bose-Hubbard model [13, 14], a bosonic analogue of the Hubbard model [44]. The model describes the competition between the hopping tendency and the on-site interactions, which determines the quantum phases. The recent experimental advancements have allowed the realization of BECs of dipolar atoms like chromium, dysprosium, erbium and europium [45–52]. These dipolar atoms interact with a long-range dipole-dipole interaction. The BHM can be extended with an additional term corresponding to dipolar interactions. The extended BHM (eBHM) supports quantum phases with periodic modulation in density, like the incompressible density-wave and the novel supersolid phase [53–55]. Chapter 2 provides a description of the BHM and its quantum phases. In this chapter, we also discuss some of the numerical mean-field methods used in this thesis to obtain the ground state quantum phases of BHM and its extensions.

Being charge neutral, ultracold atoms trapped in optical lattices cannot experience a Lorentz force necessary for observing topological phases like quantum Hall, spin Hall effect and a multitude of other effects. However, the effect of magnetic field on the ultracold atoms can be simulated with the realization of artificial gauge fields due to development of novel experimental techniques like the laser-assisted tunnelling [25, 26] and dynamical shaking [56]. In addition, with optical lattices the magnetic flux piercing a unit cell can be tuned to significantly large values owing to the larger

lattice constant $\approx 1\mu m$. This helps in realizing several FQH states which are otherwise difficult to observe in condensed matter systems due to the requirement of very high magnetic fields $\approx$ 100T. Theoretically, with the implementation of artificial gauge fields in optical lattices, nearest neighbour hopping of atoms leads to the development of a phase. In other words, the hopping strength picks up a phase $e^{i2\pi\alpha}$ via Peierls substitution [57, 58], with α being the magnetic flux piercing the unit cell. The gauge fields also affect other quantum phases of ultracold atoms. For instance, the parameter regimes of localized phases are enhanced owing to the cyclotronic motion of atoms [59, 60]. The single-particle spectrum in the presence of a magnetic field, given by the Landau levels in the continuum, are modified in the optical lattice. This is due to the discreteness of the lattice. The energy spectrum has a fractal structure known as the Hofstadter butterfly [58]. Thus, the FQH physics is different in the optical lattice, particularly for large α limit where the discreteness of the lattice compared to the magnetic unit cell becomes more apparent.

1.3.1 Exact diagonalization for bosons in optical lattice

The mean-field description does not capture the correlation effects in a quantum many-body systems accurately and are not suitable to study strongly correlated states. In addition, for strongly correlated quantum phases like the FQH states with large α, respecting the magnetic translational symmetry requires exact calculations within the magnetic unit cell. The use of exact diagonalization (ED) for ultracold atoms in optical lattices is possible for small sized lattices, owing to the exponential growth of the Hilbert space with the lattice size. This can be understood as follows. The hopping of particles in the lattice can be described by coupled occupation number basis of the form $|n_1, n_2, \cdots n_{N_s}\rangle$, where, n_i represents the particle occupancy at the ith lattice site amongst the total N_s lattice sites. If we restrict the maximum allowed single-site occupancy to N_b, the total number of distinct basis states is $N_b^{N_s}$. Thus, it can be seen that the number of basis states grows exponentially with the lattice size. Although, the Hamiltonian conserves the total particle number, for fixed particle sectors the size of Hilbert space can still be quite large. The ED method involves the construction of the basis states and evaluating the Hamiltonian matrix with this basis set. A numeri-

cal diagonalization then gives the eigenvalues and eigenstates of the system. For most of the studies at low temperatures, the knowledge of few low-energy states is sufficient. This simplification allows for relatively fast numerical diagonalization using the well-known Lanczos algorithm. There exist several tutorials and reviews on the ED technique [61–63], and it has been extensively studied for the spin-systems [64, 65]. In Chapter 3, we discuss our implementation of ED based on a hierarchy of states. This implementation allows for easy imposition of additional constraints to filter the basis states. This can lead to a significant reduction in the size of Hilbert space in certain cases. In this thesis, we use the ED method for characterizing the topological order in bosonic FQH states and studying the bi-partite entanglement of these states. The cluster Gutzwiller mean-field (CGMF) method, which we implement as an extension of the ED method, is used to identify the FQH states as the ground state in optical lattice against other competing quantum phases. With this brief description of the numerical ED method, let us discuss some of the previous works on bosonic FQH in optical lattices.

1.3.2 FQH states with ultracold atoms

Early works on FQH states used rotating BECs to mimic the effects of Lorentz force [66, 67]. This was motivated by the study showing that the FQH state with filling factor $\nu = 1/2$ is the ground state for a bosonic gas with N particles rotating at very high total angular momentum $L = N(N-1)$ in isotropic parabolic trap [68]. In the rotating frame, the effects of the Coriolis force are analogous to the Lorentz force. However, with rotating BECs, the energy gap between the ground state and excited states is small and can affect the stability of the state. As discussed earlier, with optical lattices, the strongly interacting regime is accessible with higher energy gap. And with the implementation of artificial gauge fields, these systems are better candidates for studying QH states. This has led to various proposals to realize bosonic analogues of FQH states in optical lattice and the details are covered in some of the excellent reviews [69–72].

A theoretical proposal for realizing bosonic FQH state by melting a Mott-insulator phase in a superlattice potential was put forward in Ref. [73]. In this work, ED study

shows the ground state as FQH state with an excellent overlap with the Laughlin wavefunction for $\alpha \lesssim 0.3$. For larger α, the ground state may still be FQH but different from Laughlin wavefunction. This ambiguity is resolved with the identification of the FQH state through many-body Chern number, which is non-zero for topological phases like FQH, as reported in Ref. [74]. For $\nu = 1/2$ filling, the ground state is observed to be FQH state till $\alpha < 0.4$, suggesting the FQH physics to be different in a lattice compared to the continuum. Bilayer FQH states at high synthetic magnetic fields have been theorized in Ref. [75]. For BHM, the FQH states are predicted to emerge in the vicinity of the Mott lobes [76, 77]. Several numerical studies exist on the bosonic FQH states in optical lattices [78–82]. Most recently, the $\nu = 1/2$ bosonic FQH state was realized experimentally for the first time with ultracold ^{87}Rb atoms in an optical lattice [27]. This remarkable achievement shall boost the realization of FQH states at other fillings in optical lattices.

It is interesting to investigate the bosonic FQH states in optical lattice with the dipolar interactions. With dipolar interactions truncated to nearest-neighbor (NN) interaction, bosonic FQH states have been explored in the vicinity of Mott lobes in Ref. [59], with the effective Hamiltonian for the excess particle in the single-site Gutzwiller mean-field prescription. With the mean-field theory, a vortex solid state is obtained in the absence of NN interactions. And finite NN interactions destabilize the vortex solid state by favouring a featureless homogeneous state, termed as Bose metal. Using the Chern-Simons theory, the authors propose a Chern-Simons wavefunction that describes the FQH state and is preferred as the strength of NN interactions is increased. In Ref. [74], ED study reveals that the energy gap between the ground state and excited state increases with the strength of dipolar interactions. And, the topological order of ground state survives with dipolar interactions. The larger energy gap is beneficial in experimental realization of FQH states. Motivated by this, Chapter 4 investigates the possibility of obtaining FQH states as ground states in optical lattices. With the CGMF method, the parameter regimes are explored where FQH state appears as ground state against the competing superfluid state. The topological order of the FQH state is identified by calculating the many-body Chern number. And, the effect of dipolar interactions is studied on the stability of the FQH state.

1.4 Quantum quench dynamics

The ability to control and manipulate the behaviour of quantum systems is at the core of developing quantum technologies and exploring novel quantum phenomena. These manipulations allow us to prepare particular states of the system by adiabatically changing the parameters of an initial state. In other words, the dynamics and out-of-equilibrium phenomenon becomes important. The out-of-equilibrium dynamics of quantum systems and their response under changes in the underlying Hamiltonians have been extensively studied. And, important questions pertaining to the thermalization and equilibriation of isolated quantum systems are addressed. The quantum systems can be driven out of their equilibrium states by coupling to an external environment, thus allowing for exchange of energy and particles. The dynamics of the system is governed by a non-unitary evolution due to the open system condition. Another way to induce the non-equilibrium behaviour is by a quantum quench, which involves changing the parameters of the Hamiltonian and allows studying the closed system unitary dynamics. The non-equilibrium dynamics with quantum quenches across continuous quantum phase transition have been linked to the Kibble-Zurek mechanism. It describes the formation of defects during symmetry-breaking phase transitions [83–86]. Ultracold atoms trapped in optical lattices provide an excellent experimental platform for investigating non-equilibrium dynamics in controlled settings. The precise control over the parameters of the system allows for the creation of a variety of quantum states and their evolution under a quantum quench. Moreover, these systems exhibit remarkable isolation from their environment, making them ideal for studying the closed system dynamics and exploring fundamental quantum phenomena. This has been demonstrated with the experimental observation of MI-SF QPT in these systems [15, 43]. The quench dynamics of quantum systems have been studied for understanding the thermalization and relaxation of quantum systems [87, 88], phase ordering kinetics and domain growth laws [89–91], and entanglement growth following a quench [92, 93].

1.4.1 Kibble-Zurek mechanism

KZM is an important theoretical framework describing the universality of the non-equilibrium dynamics under a slow quench across the continuous phase transition. KZM predicts that the spontaneous symmetry breaking when the system crosses the critical point during the dynamics leads to the formation of topological defects. For most transitions, the defect density follows a universal power law behaviour with the quench rate. It is governed by the equilibrium critical exponents [85, 86]. The central idea of KZM is that near the critical point, the relaxation time diverges, and the adiabaticity in the evolution breaks down, however slow the quench. This is referred to as critical slowing down. KZM draws its inspiration from the works of Tom Kibble in the context of cosmology [83]. In the early universe after the Big Bang, the universe went through various stages of thermal phase transitions. Due to the spontaneous symmetry breaking across the continuous phase transition, an order parameter develops in the symmetry broken state. However, the local choices of the order parameter are correlated on a length scale determined by the relativistic causality, and would form domains. The uncorrelated order parameter across different domains will thus constitute topological defects at the meeting point of these domains. Zurek extended the Kibble's idea to non-relativistic condensed matter systems like He^4 by identifying that the critical slowing down near phase transitions can play a role similar to the relativistic causality [84, 94]. Using the power-law divergence of the equilibrium correlation length and relaxation time near the critical point, Zurek predicted universal scaling laws for the size of correlated domains and the defect density as a function of the quench rate. These constitute the Kibble-Zurek (KZ) scaling laws and the predictions have been experimentally tested for thermal phase transitions in superfluid He [95–97] and various other condensed matter systems [98–107].

Originally, KZM was developed to describe the continuous symmetry breaking in thermal phase transitions. Subsequently, KZM was extended to describe the dynamics across QPTs [108]. The extension of KZM to QPTs is not trivial, the nature of fluctuations driving the phase transition being quantum in nature compared to the dissipative thermal fluctuations. For the quantum systems, the energy gap between the ground state and the first excited state vanishes at the quantum critical point leading to the

breakdown of adiabaticity during the evolution. This is in close resemblance to the critical slowing down for the thermal phase transitions. The predictions of KZM were tested for the 1D quantum Ising model in Ref. [108]. The applicability of KZM theory in describing the dynamics of the simplest quantum two-level model, the Landau-Zener model was shown in Ref. [109]. Several other theoretical [109–125] and experimental [126–131] works have emerged in recent times on the KZM.

1.4.2 Quench dynamics of ultracold atoms

Early investigations on the non-equilibrium dynamics of ultracold atoms were studied in the weakly interacting regime for BECs trapped in harmonic potential traps [126, 132–136]. And the predictions of KZM have been tested for quenches across the BEC transition [137–140]. The quench dynamics across QPT with ultracold atoms have been investigated in various theoretical [94, 108, 110, 112, 141–144] and experimental works [129–131, 145–148]. The experiment in Ref. [145], investigated the quench across the MI-SF QPT for inhomogeneous BHM in 3D optical lattice. The quench was performed by continuous tuning of the ratio of hopping strength to interaction energy, driving an initial MI phase into SF phase across the generic phase transition. The quench rate was carefully chosen to be slow to avoid excitation of atoms into higher vibrational states of the lattice potential. Using the time-of-flight imaging, the excitation density in the post-quenched state was measured. The excitation density and energy produced from quench was found to have a power law dependence on quench rate suggesting a KZM mechanism for the defect generation. However, the power law exponents differ significantly from the KZM prediction. The disagreement was attributed to a number of factors like the inhomogeneous nature of the gas, different nature of excitations or due to thermal effects at low but finite temperatures. Another experiment [146] explored the dynamics across MI-SF QPT in 1D optical lattice using ^{39}K atoms. The initial MI phase was quenched into SF phase by linearly decreasing the lattice depth. The ramp times or the quench rate is chosen to ensure no mass transport, leading to the QPT at fixed density. The coherence length of the atoms was determined from the width of the interference peaks obtained from time-of-flight absorption images. It was observed that coherence length follows a power-law only

for intermediate range of the quench rate. And the power-law exponent deviates from the KZM prediction and infact is dependent on the final value of U/J at which the quench is terminated. Even on the theoretical front, the discrepancy in the power law exponents for MI-SF QPT is still unresolved [142, 144]. Motivated by this, we have investigated the quench dynamics across the MI-SF QPT in BHM for generic transition (away from the tip of Mott lobe) and at the multicritical point. Chapter 5 reports the results obtained from the single-site Gutzwiller mean-field (SGMF) and CGMF methods.

1.5 Highlights of the thesis

The highlights of research work presented in this thesis are as follows:

- We have presented a novel implementation of the exact diagonalization technique for solving the ground state of bosonic particles in lattice models. The ED technique can be easily extended for the CGMF studies.
- The described implementation of ED allows for filtering of the basis states according to some clever constraints. These constraints are based on some apriori expectations from the ground state. Depending upon the constraints, a significant reduction in the Fock-space is possible. This is quite important for ED studies, where the Fock-space grows exponentially with the system size.
- We have extended the developed ED technique for calculating the reduced density matrix for spatial bi-partitioning of the lattice. Using this, we have investigated the area law for the entanglement entropy and also studied the topological entanglement entropy in the FQH states.
- We have studied the bosonic FQH effect in optical lattice. With CGMF, we have investigated the parameter regimes where FQH states can exist as the ground state against the competing superfluid state. The two-point correlation function revealed signatures of a gapped bulk and gapless edges, which are consistent with the FQH state. The topological order of FQH state is investigated by calculating the many-body Chern number.

- We have explored the effect of dipolar interactions on the stability of bosonic FQH states in optical lattice. We find that the dipolar interactions stabilize the FQH state against the competing SF state.

- We have examined the quantum quench dynamics across the MI-SF QPT at the multicritical point and for a generic transition below the tip of the Mott-1 lobe with SGMF. We have obtained the KZ scaling laws for the impulse-adiabatic crossover time and the vortex density. The dynamically obtained critical exponents differs from their equilibrium counterparts.

- With CGMF method, we revisited the quench across the MI-SF QPT. In contrast to the SGMF, the CGMF captures the evolution of the quenched state in the "impulse" regime of KZM. The mismatch between the dynamically obtained critical exponent z and its equilibrium value decreases with increase in the size of clusters used in CGMF.

1.6 Overview of the chapters

The overview of the chapters in the rest of the thesis is as follows.

- Chapter 2 describes the BHM, and its ground-state quantum phases. We then describe the numerical mean-field methods, SGMF and CGMF, that are used in this thesis for obtaining the ground state quantum phases of BHM and its extension. Towards the end, we discuss the time-dependent Gutzwiller equations used for studying the dynamical evolution of the quantum state.

- Chapter 3 discusses a novel implementation of the exact-diagonalization technique for solving the ground state for the system of bosonic particles in a lattice. The proposed technique allows for significant reduction in the Fock-space with the ability to impose some clever constraints for filtering out the basis states. Towards the end, we demonstrate the technique for studying the entanglement properties of the bosonic FQH states.

- Chapter 4 discusses the FQH effect in optical lattice. We have investigated the parameter regimes where FQH states occur as the ground state. We have charac-

terized the FQH state by studying the two-point correlation function. The topological order in the state is demonstrated by calculating the many-body Chern number. Afterwards, the effect of dipolar interactions on FQH states is discussed. We find that it preserves the topological order and stabilizes the FQH states against the competing superfluid states.

- Chapter 5 discusses the quantum quench dynamics across the MI-SF QPT of the BHM. The quenches are performed for the generic transition and across the multi-critical point. We have investigated the validity of KZM and obtained the KZ scaling relations with the SGMF and CGMF methods. The CGMF method captures the evolution of the quenched state in the "impulse" regime of KZM which is otherwise absent in the SGMF theory. The obtained power law exponents have a mismatch compared to the KZM predictions. However, the mismatch between the dynamically obtained critical exponent z and its equilibrium value decreases with the increase in the size of clusters used in CGMF.

- Chapter 6 states the conclusions of the thesis and the future research directions that can be pursued.

Chapter 2

Theoretical and Numerical methods

The experimental realization of BECs of dilute atomic gases at ultracold temperatures ($\approx 10^{-9}$ K) has initiated a new era in the field of atomic and molecular physics [149]. In general, cooling of gases to ultracold temperatures leads to the formation of solid phase. To overcome solidification and achieve BECs, atomic gases need to be dilute. Very low densities ($10^{13} - 10^{15}$ atoms per cm^{-3}) imply that the inter-atomic interaction is weak. The system of such a weakly interacting Bose gases is well described by the Gross-Pitaevskii (GP) equation [150, 151]. However, the GP framework is not applicable to the strongly-interacting systems. By trapping the ultracold gases in optical lattices, the itinerancy of the atoms can be reduced by increasing the depth of potential wells. This effectively drives the system to the strong-interaction regime [15]. These systems are versatile finite quantum many-body systems and offer a very good control over various system parameters. Using these systems, it is thus possible to explore various phenomena associated with quantum many-body systems at a macroscopic scale in the laboratories [149, 152, 153]. Many such advantages offered by these systems make them an excellent choice as quantum simulators to explore quantum many-body physics. These systems can be described theoretically by the Bose-Hubbard model and its variants.

The BHM describes the system of interacting ultracold gas of bosonic atoms in a lattice. This is a minimal model with a nearest neighbor hopping term to represent the kinetic energy, and an on-site potential term arising from the interatomic contact interaction potential [13, 154]. The latter is because of the fact that at low densities

and temperatures, the interatomic interaction is well described by contact interaction. The BHM supports two quantum phases as the ground state of the system, the Mott-insulator and the superfluid phases, in various parameter regimes. These phases are separated by a quantum phase transition, which has been demonstrated experimentally [15, 43]. The BHM can be modified and extended with appropriate terms according to the system of study, and this may lead to the emergence of new quantum phases. The system of ultracold gases in optical lattices is versatile and allows the engineering of a variety of exotic and novel quantum phases [149, 154–156]. For example, in the case of dipolar atoms, approximation with nearest-neighbour interaction leads to the emergence of two new quantum phases. These are the density wave and supersolid phases [157]. The BHM can also be adapted to model the effect of magnetic fields on the atoms for the investigation of the Hall effect. The hopping amplitudes in the BHM are then modified by an appropriate lattice-site dependent phase factor. With this, the extended model can support the quantum Hall states.

In this chapter, we shall first derive the BHM from a second-quantized Hamiltonian with a general two-body interaction, which describes interacting bosonic gases in optical lattice. We shall discuss the ground-state quantum phases supported by the BHM and the numerical methods employed for obtaining the ground-state of the system. These include the mean-field methods based on the Gutzwiller ansatz, namely the single-site Gutzwiller mean-field (SGMF) and the cluster-Gutzwiller mean-field methods. At the end, we shall discuss the phase diagram of BHM. Finally, we discuss the time-dependent Gutzwiller equations used for studying the time evolution of quantum phases.

2.1 Bose-Hubbard model

The second-quantized Hamiltonian which described neutral bosonic atoms in a lattice potential with a general two-body interaction can be written as

$$\begin{aligned}\hat{H} &= \int \mathrm{d}\mathbf{r}\hat{\Psi}^\dagger(\mathbf{r})\left(-\frac{\hbar^2}{2m}\nabla^2 + V^{\mathrm{latt}}(\mathbf{r}) + V^{\mathrm{trap}}(\mathbf{r})\right)\hat{\Psi}(\mathbf{r}) \\ &\quad + \frac{1}{2}\int \mathrm{d}\mathbf{r}\mathrm{d}\mathbf{r}'\hat{\Psi}^\dagger(\mathbf{r})\hat{\Psi}^\dagger(\mathbf{r}')U_{\mathrm{int}}(\mathbf{r}-\mathbf{r}')\hat{\Psi}(\mathbf{r}')\hat{\Psi}(\mathbf{r}). \qquad (2.1)\end{aligned}$$

Here, $\hat{\Psi}^{\dagger}(\mathbf{r})$ and $\hat{\Psi}(\mathbf{r})$ are the bosonic creation and annihilation field operators, respectively, which satisfy the canonical commutation relations. The lattice potential due to the sinusoidal standing wave formed by counter-propagating lasers is of form $V^{\text{latt}}(\mathbf{r}) = V_o \sin^2(2\pi x/\lambda)$ along the spatial degrees of freedom, with λ being the wavelength of the laser and V_o is the measure of the AC Stark effect, which depends on the laser intensity and the polarizability of the atoms [132, 155]. The additional trapping potential $V^{\text{trap}}(\mathbf{r})$ is applied to limit the spatial extent of the condensate atoms within the optical lattice. Otherwise, the atoms shall tunnel across the lattice sites and escape from the optical lattice. For ultracold dilute gases, the interatomic interaction can be approximated as a contact potential given by [155]

$$U_{\text{int}}(\mathbf{r}-\mathbf{r}') = \frac{4\pi\hbar^2 a_s}{m}\delta(\mathbf{r}-\mathbf{r}'), \tag{2.2}$$

where, m is the mass of the atoms and a_s is the s-wave scattering length. It is useful to expand the field operators in the Wannier basis, formed by the wavefunctions centred around the lattice sites. Assuming the *tight-binding limit* for the case of deep lattice potential, the Wannier functions are localized at the lattice sites. The depth of the lattice potential also ensures that the energy band gap between the lowest and higher Bloch bands is large compared to the other relevant energy scales of the system. Thus, for deep lattices and at ultracold temperatures, the dynamics of the system is approximated to be frozen to the lowest band only. In the *lowest-band approximation*, we can thus expand the field operators in terms of the Wannier functions of the lowest Bloch band as [14, 149, 158]

$$\hat{\Psi}(\mathbf{r}) = \sum_i w_0(\mathbf{r}-\mathbf{R_i})\,\hat{b}_i, \tag{2.3}$$

where, i is the lattice site index, $\hat{b}_i$ is the bosonic annihilation operator at the ith lattice site, and $w_0(\mathbf{r}-\mathbf{R_i})$ is the lowest band Wannier function centered at the ith lattice site whose spatial coordinates are given by $\mathbf{R_i}$. The bosonic creation (annihilation) operators $\hat{b}_i^{\dagger}$ ($\hat{b}_i$) satisfy the usual canonical commutation relations

$$\left[\hat{b}_i, \hat{b}_j^{\dagger}\right] = \delta_{i,j}, \quad \left[\hat{b}_i^{\dagger}, \hat{b}_j^{\dagger}\right] = \left[\hat{b}_i, \hat{b}_j\right] = 0. \tag{2.4}$$

The vanishing overlap between the Wannier functions of distant lattice sites allows the hopping to be restricted to the NN sites (denoted by $\langle i,j\rangle$) with the hopping strength

$$J_{ij} = -\int \mathrm{d}\mathbf{r} w_0^*(\mathbf{r}-\mathbf{R_i})\left(-\frac{\hbar^2\nabla^2}{2m} + V^{\text{latt}}(\mathbf{r}) + V^{\text{trap}}(\mathbf{r})\right) w_0(\mathbf{r}-\mathbf{R_j}), \tag{2.5}$$

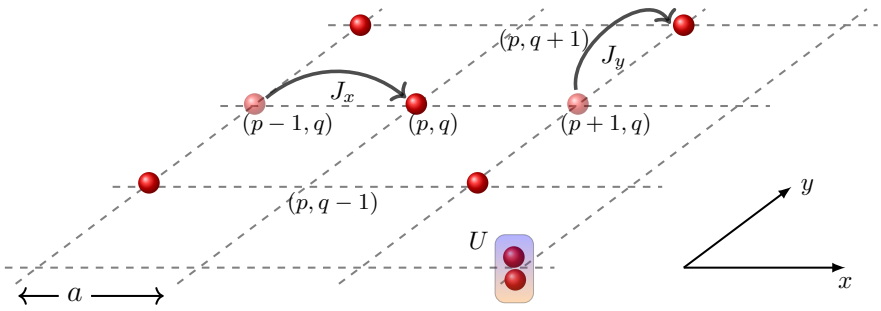

Figure 2.1: A schematic illustration of the NN hopping and onsite interaction terms in BHM for a 2D lattice.

and similarly, $\epsilon_i = J_{ii}$ is the on-site one body potential which represents the potential offset for the case of a non-uniform lattice. The two-body inter-atomic interaction potential term can be considered as a local or onsite and its strength is

$$U = \frac{4\pi\hbar^2 a_{\rm s}}{m} \int \mathrm{d}\mathbf{r} |w_0(\mathbf{r} - \mathbf{R_i})|^4. \tag{2.6}$$

Thus, in the tight-binding limit and with the lowest-band approximation, the Hamiltonian in Eq. (2.1) in terms of the Wannier basis gives the BHM Hamiltonian

$$\hat{H}_{\rm BHM} = -\sum_{\langle i,j \rangle} J_{ij} \hat{b}_i^\dagger \hat{b}_j + \frac{U}{2} \sum_i \hat{n}_i(\hat{n}_i - 1) + \sum_i \epsilon_i \hat{n}_i, \tag{2.7}$$

where, $\hat{n}_i = \hat{b}_i^\dagger \hat{b}_i$ is the occupation number operator. In the grand-canonical ensemble, a term corresponding to the chemical potential (μ) of the gas is added to the Hamiltonian in Eq. (2.7) to fix the total number of atoms in the lattice. The BHM Hamiltonian is then given by

$$\hat{H}_{\rm BHM} = -J \sum_{\langle i,j \rangle} \hat{b}_i^\dagger \hat{b}_j + \frac{U}{2} \sum_i \hat{n}_i(\hat{n}_i - 1) - \mu \sum_i \hat{n}_i. \tag{2.8}$$

where, we have replaced the NN hopping strength J_{ij} by J for a homogeneous lattice and have dropped the term corresponding to the potential offset in a non-uniform lattice.

The different terms of the BHM Hamiltonian for a 2D square lattice considered in this thesis are schematically shown in Fig. 2.1. The lattice site index i then refers to the spatial coordinates (p, q) and the NN site corresponding to the (p, q)th site now

represents an element of the set $\{(p+1,q),\,(p-1,q),\,(p,q+1),\,(p,q-1)\}$. In the schematic diagram, the hopping strengths along the x and y directions are assumed to be different, and this corresponds to anisotropic hopping strengths. Unless otherwise specified, we shall always assume isotropic and homogeneous hopping strengths J and drop any redundant subscripts throughout this thesis.

To understand the ground state quantum phases of the BHM, let us consider two extreme regimes of the system parameters. In the strongly interacting parameter regime $J/U \to 0$, we can neglect the hopping term in the BHM Hamiltonian. Since the Hamiltonian has only occupation number operators, the ground state is of the form

$$|\Psi_{J=0}\rangle = \prod_i |n\rangle_i \,. \tag{2.9}$$

This describes the MI phase with n atoms at each lattice site. The integer commensurate density is fixed by the chemical potential of the gas. In the opposite regime $U/J \to 0$ which corresponds to the weakly interacting regime, the ground state corresponds to a superfluid where all the N_p particles occupy the zero momentum state of the lowest Bloch band. This superfluid state has the wavefunction [149, 158]

$$|\Psi_{U=0}\rangle = \frac{1}{\sqrt{N_p!}}\left(\frac{1}{\sqrt{N_s}}\sum_i \hat{b}_i^\dagger\right)^{N_p} |0\rangle_i \,, \tag{2.10}$$

where, N_s is the number of lattice sites. Thus, at the extreme values of the parameter J/U, BHM supports a localized MI phase and a delocalized SF phase. And, there exists a quantum phase transition between the two phases at some critical value of J/U. To explore the ground-state quantum phases of the BHM, we need to solve for the ground state of the Hamiltonian.

Theoretical exploration of BHM includes various theoretical methods, for instance, the Bogoliubov techniques for the case of weak interactions [159], perturbative methods for strongly interactions systems [160, 161], Gutzwiller mean-field approaches [14, 162], field-theoretic investigations [163–165], among others. The ground state properties of such systems have also been examined through various numerical techniques such as the Density Matrix Renormalization Group methods [166, 167] and Quantum Monte-Carlo methods [168]. Now, we shall describe some numerical methods used in this thesis for studying these systems.

2.2 Numerical methods to solve BHM

The Hamiltonian in Eq. (2.8) couples NN sites through the hopping term consisting of bilinear operators. Therefore, a natural basis for expressing the Hamiltonian matrix is provided by coupled Fock-state basis, which is the direct product of the single-site Fock-state basis and corresponds to the configuration of lattice occupancies. For a $K \times L$ system, the basis state has the form

$$\prod_{p,q} |n\rangle_{p,q} \equiv |n_{1,1}, \cdots n_{p,q}, \cdots n_{K,L}\rangle \,. \tag{2.11}$$

The wavefunction of the system in the coupled Fock-state basis is then expressed as the linear combination

$$|\Psi\rangle = \sum_{\substack{n_{1,1} \\ \cdots \\ n_{p,q} \\ \cdots \\ n_{K,L}}} C_{n_{1,1},\cdots n_{p,q},\cdots n_{K,L}} \, |n_{1,1}, \cdots n_{p,q}, \cdots n_{K,L}\rangle \,. \tag{2.12}$$

The ground-state wavefunction is obtained by diagonalizing the Hamiltonian matrix. This method of obtaining the eigenspectrum from the one-time diagonalization of the Hamiltonian matrix is called the exact-diagonalization method. However, the Fock-space spanned by the coupled basis states grows exponentially with the size of the lattice. Thus, the techniques like ED demands heavy computational resources [61, 62]. In Chapter 3, we discuss in detail the numerical implementation of an ED method we have developed. Alternatively, an approximate description of the ground state phases can be obtained using the mean-field descriptions. In this approach, the bilinear operators are approximated by a single site operator times the mean-field of the NN site. The mean-field approximation leads to a drastic reduction in the Fock-space and simplifies the calculations.

2.2.1 Single-site Gutzwiller mean-field theory

In the SGMF theory, the bosonic operators are decomposed in terms of a mean-field and a fluctuation as [162, 169]

$$\hat{b}_i = \phi_i + \delta\hat{b}_i, \tag{2.13a}$$

$$\hat{b}_i^\dagger = \phi_i^* + \delta\hat{b}_i^\dagger. \tag{2.13b}$$

Here, $\phi_i = \langle \hat{b}_i \rangle$ and $\phi_i^* = \langle \hat{b}_i^\dagger \rangle$ are the mean fields at the ith lattice site and are the expectation values of the bosonic operators taken with respect to the ground state. The residual fluctuations are represented by the operators $\delta\hat{b}_i$ and $\delta\hat{b}_i^\dagger$. With these decompositions, the bilinear operator in the hopping term can be rewritten as

$$\hat{b}_i^\dagger \hat{b}_j = \hat{b}_i^\dagger \phi_j + \phi_i^* \hat{b}_j - \phi_i^* \phi_j, \tag{2.14}$$

where we have neglected the term which is second order in the fluctuation operators. The mean-field BHM Hamiltonian can now be written as a sum of single site Hamiltonians, $\hat{H}_{\rm MF} = \sum_{p,q} \hat{h}_{p,q}$ with the single site Hamiltonian given by

$$\begin{aligned} \hat{h}_{p,q} \;=\; & -J\left(\phi_{p+1,q}^* \hat{b}_{p,q} + \phi_{p-1,q} \hat{b}_{p,q}^\dagger - \frac{1}{2}\phi_{p+1,q}^* \phi_{p,q} - \frac{1}{2}\phi_{p-1,q}\phi_{p,q}^* + \text{H.c.}\right) \\ & -J\left(\phi_{p,q+1}^* \hat{b}_{p,q} + \phi_{p,q-1} \hat{b}_{p,q}^\dagger - \frac{1}{2}\phi_{p,q+1}^* \phi_{p,q} - \frac{1}{2}\phi_{p,q-1}\phi_{p,q}^* + \text{H.c.}\right) \\ & + \frac{U}{2}\hat{n}_{p,q}(\hat{n}_{p,q} - 1) - \mu \hat{n}_{p,q}. \end{aligned} \tag{2.15}$$

The mean-filed Hamiltonian is a direct sum of the single site Hamiltonians coupled through the mean-fields of the NN sites. Following the *Gutzwiller ansatz*, the total wavefunction of the system can be written as a product of single site wavefunctions expanded in terms of the Fock-state basis [170]

$$|\Psi_{\rm GW}\rangle = \prod_{p,q} |\psi\rangle_{p,q} = \prod_{p,q} \sum_{n=0}^{N_{\rm b}-1} c_n^{(p,q)} \, |n\rangle_{p,q} \, . \tag{2.16}$$

For the occupation number $n_{p,q}$ at lattice site (p,q), the corresponding state $|n\rangle_{p,q}$ constitutes the Fock-state basis and $c_n^{(p,q)}$ represent the coefficients. The total number of Fock-state basis used in the expansion of the single-site wavefunction is set by the cut-off value $N_{\rm b}$. It should be noted that the *Gutzwiller ansatz* is followed exceptionally well by the localized phases in the strongly interacting regime and provides a reasonable description of the non-localized phase near the MI-SF phase boundary. The two quantum phases of BHM are distinguished by the SF order parameter $\phi = (1/N_s)\sum_{p,q} \phi_{p,q}$. It is zero in the MI phase since, at each site, only one Fock-state contributes. However, in the SF phase ϕ is non-zero as many Fock-states contribute. From the ground state wavefunction, the mean-field is

$$\phi_{p,q} = \langle \Psi_{\rm GW} | \hat{b}_{p,q} | \Psi_{\rm GW} \rangle = \sum_{n=1}^{N_{\rm b}-1} \sqrt{n} c_{n-1}^{(p,q)^*} c_n^{(p,q)}. \tag{2.17}$$

Similarly, one can obtain other observables like the average occupancy at any lattice site by calculating $\langle \hat{n}_{p,q} \rangle$.

The Hamiltonian in Eq. (2.15) depends on three parameters, namely, J, U and μ, and can be rescaled by any one of these. After rescaling the Hamiltonian by the on-site interaction strength, the parameters which determine the ground state of the system are J/U and μ/U. To obtain the ground-state of the Hamiltonian for chosen values of J/U and μ/U, we start with an appropriate initial guess for the unknown mean-field $\phi_{p,q}$ and construct the Hamiltonian matrix in the Fock-state basis. The matrix is tri-diagonal of size $N_b \times N_b$. The Hamiltonian matrix is then diagonalized using the standard linear algebra package LAPACK [171], to obtain the ground state eigenvector. From this, we can calculate an improved estimate for the mean-field $\phi_{p,q}$. This procedure is repeated for all the lattice sites. The calculated mean-field is used as an improved guess for the mean-field in the next iteration. The iterations are continued till the mean-field converges upto a desired accuracy. For this, we consider the average in the difference of $\phi_{p,q}$ between two successive iterations $\Delta\phi^{\mathrm{i}}_{p,q} = \sum_{p,q}(|\phi^{\mathrm{i}}_{p,q} - \phi^{\mathrm{i+1}}_{p,q}|)/N_s$ as the convergence parameter and condition for convergence is set as $\Delta\phi^{\mathrm{i}}_{p,q} \leqslant 10^{-9}$. Here, N_s is the total number of lattice sites, and the superscripts i and $i+1$ indicate the iteration step. The Fock-space cutoff N_b is chosen as a sufficiently large value (~ 10) such that the computed results are unchanged for any larger choice of the cutoff. To minimize the finite-size effects and obtain the results in the thermodynamic limit corresponding to an infinite lattice, periodic boundary conditions (PBC) are employed along the two spatial directions. The SGMF method gives qualitative features of the quantum phases of BHM and the MI-SF phase boundary. However, it has a shortcoming associated with the poor accounting of the inter-site correlations because of the mean-field approximation.

2.2.2 Cluster Gutzwiller mean-field theory

In the CGMF theory, the mean-field decomposition of the hopping terms is applied only at selective bonds, while at the other bonds, the hopping term is treated exactly. This improves the description of the inter-site correlations in the state [172]. In this method, a 2D lattice with spatial dimensions $K \times L$ is tiled with small clusters of

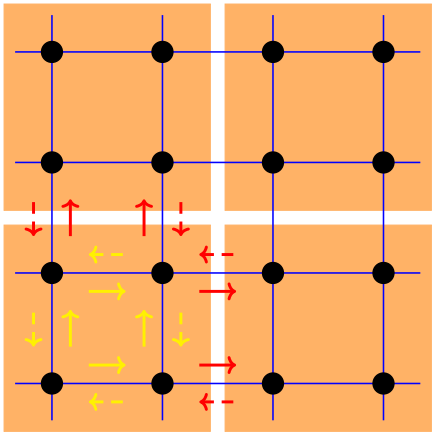

Figure 2.2: Schematic of a 4×4 lattice tiled up by clusters of size 2×2. The solid (dashed) yellow colored arrows represent the exact hopping term (hermitian conjugate) within the cluster. The solid (dashed) red arrows represent the inter-cluster hopping term (hermitian conjugate).

dimensions $M \times N$. The hopping between the sites within the cluster is treated exactly, while for the sites at the boundary, the inter-cluster hopping is treated within the mean-field prescription. This is shown schematically in Fig. 2.2, where a 4×4 lattice is titled using 2×2 clusters. The NN hoppings for the bottom-leftmost cluster are marked with solid arrows and the dashed arrows represent the hermitian conjugate hopping. The yellow colored arrows represent intra-cluster hopping, which is treated exactly. The inter-cluster hoppings, shown with red colored arrows, are represented with the mean-field approximations. With this prescription, the total Hamiltonian can be written as a sum over the cluster Hamiltonians $\hat{H}_{\mathrm{CGMF}} = \sum_C \hat{H}_C$ with the cluster Hamiltonian

$$\begin{aligned}
\hat{H}_C \;=\; & {\sum_{p,q\in C}}' -J\left[\hat{b}^\dagger_{p+1,q}\hat{b}_{p,q} + \mathrm{H.c.}\right] + {\sum_{p,q\in C}}' -J\left[\hat{b}^\dagger_{p,q+1}\hat{b}_{p,q} + \mathrm{H.c.}\right] \\
& + \sum_{p,q\in \delta C} -J\left[\phi^*_{p\pm1,q}\left(\hat{b}_{p,q} - \frac{1}{2}\phi_{p,q}\right) + \mathrm{H.c.}\right] \\
& + \sum_{p,q\in \delta C} -J\left[\phi^*_{p,q\pm1}\left(\hat{b}_{p,q} - \frac{1}{2}\phi_{p,q}\right) + \mathrm{H.c.}\right] \\
& + \sum_{p,q\in C}\left[\frac{U}{2}\hat{n}_{p,q}\left(\hat{n}_{p,q}-1\right) - \mu\hat{n}_{p,q}\right].
\end{aligned} \tag{2.18}$$

Here, the prime over the summations denotes a restricted sum over the bulk sites (p, q) of cluster C such that its NN site $(p+1, q)$ in the first summation or $(p, q+1)$ in the

second summation belong to the same cluster C. The summation over sites $(p,q) \in \delta C$ indicates the sites at the boundary of the cluster such that its NN site lies outside the cluster. The NN of site $(p,q) \in \delta C$ corresponds to the site $(p-1,q)$ and $(p+1,q)$ on the left and right boundary, respectively. Similarly, the site $(p,q-1)$ and $(p,q+1)$ correspond to the bottom and top boundaries, respectively. In the hopping term, the operators of these NN sites are replaced by the mean-field ϕ.

The Hamiltonian matrix corresponding to $\hat{H}_C$ can be constructed in the coupled Fock-state basis $\prod_{p,q\in C} |n\rangle_{p,q} \equiv |n_1 n_2 \cdots n_{MN}\rangle$, where the lattice sites within the cluster are labelled by indices 1, 2, $\cdots$ MN. Since at each lattice site, the occupancy can take any value from the N_b possible choices, the coupled Fock-state basis are $N_b^{M\times N}$ in number. This exponential scaling of the coupled Fock-state basis with the cluster size limits the use of larger sized clusters, which can improve the description of the inter-site correlations. However, with some information about the expected ground state, some constraints can be imposed, and the coupled Fock-state basis can be filtered. This process of state-reduction can significantly reduce the dimension of the coupled Fock-state basis and the computational load in the estimation of the ground-state. Using the *Gutzwiller ansatz*, the ground state of the entire system can be written as

$$|\Psi_{\mathrm{GW}}\rangle = \prod_{\alpha=1}^{W} |\psi_\alpha^C\rangle = \prod_{\alpha=1}^{W} \sum_{n_1 n_2 \cdots n_{MN}} c^{(\alpha)}_{n_1 n_2 \cdots n_{MN}} |n_1 n_2 \cdots n_{MN}\rangle \,. \tag{2.19}$$

Here, α labels the different clusters with total number of cluster used in tiling the lattice being $(K \times L)/(M \times N)$ and $c^{(\alpha)}_{n_0 n_1 \ldots n_{m'}}$ are the complex coefficients of the coupled Fock-states.

Similar to the SGMF, the matrix diagonalization is done self-consistently. With an initial guess for the mean-field $\phi_{p,q}$ the cluster Hamiltonian matrix is constructed for each cluster. This matrix is a sparse matrix as for a given Ket state, the total number of Bra states related by the hopping terms are bounded by the total number of bonds in the cluster. With such a large number of zero elements in the matrix, the Lanczos algorithm [173–175] (offered by packages like ARPACK [176]) can be employed for diagonalization to obtain the ground state. The local SF order parameter $\phi_{p,q} = \langle \hat{b}_{p,q} \rangle$ is obtained from the ground-state wavefunction and serves as an improvement over the initial guess of the mean-field in the next iteration. The iterations are continued

till the mean-field converges upto a desired level of accuracy ($\sim 10^{-9}$). The finite-size effects are reduced by taking the PBC along both the spatial dimensions, thereby mimicking the thermodynamic limit. More details about the CGMF can be found in [82, 177]. The results obtained from the CGMF provide significant improvements over the SGMF results and approach the quantum Monte-Carlo (QMC) results with clusters of large sizes [172, 177].

2.3 Phase Diagram of BHM

To benchmark the numerical techniques used in this Thesis, we obtain the ground-state phase diagram of BHM using SGMF and CGMF methods. As mentioned earlier, the BHM Hamiltonian can be scaled with the on-site interaction strength U. Then, the Hamiltonian has two free parameters, μ/U and J/U. The competition between these two energies determines the ground state quantum phase of the system. The plot in Fig. 2.3 shows the zero temperature phase diagram of BHM in the μ/U vs J/U plane. As expected, the MI phase appears in the strongly interacting regime $J/U \ll 1$. In the MI(1) phase, all lattice sites have exactly unit occupancy of bosons. This phase appears for $0 \leqslant \mu/U \leqslant 1$, and forms a lobe in the phase diagram. The MI phases with higher integer commensurate occupancy exists for higher values of μ/U. In Fig. 2.3, the MI-SF phase boundary has been obtained for the SGMF (blue curve) and CGMF with 2×2 cluster (green curve), and 2×3 cluster (red curve). With larger clusters, the MI-SF phase boundary shifts to higher J/U, particularly near the tip of the Mott lobe. With the improvement in the description of the correlation effects in the quantum phase using larger clusters in the CGMF calculations, the quantum critical point approaches the QMC values as can be seen for MI(1) lobe shown in Fig. 2.3. The QMC data for MI(1) lobe, used in Ref.[178], is obtained from personal communication with Prof. Barbara Capogrosso-Sansone.

This advantage of CGMF over SGMF, however, comes at the cost of larger sized Fock-space. The size grows exponentially with the cluster size and demands more computational resources. The SGMF and CGMF with appropriate cluster sizes are used depending on the quantum phase of interest. The MI-SF phase boundary is ob-

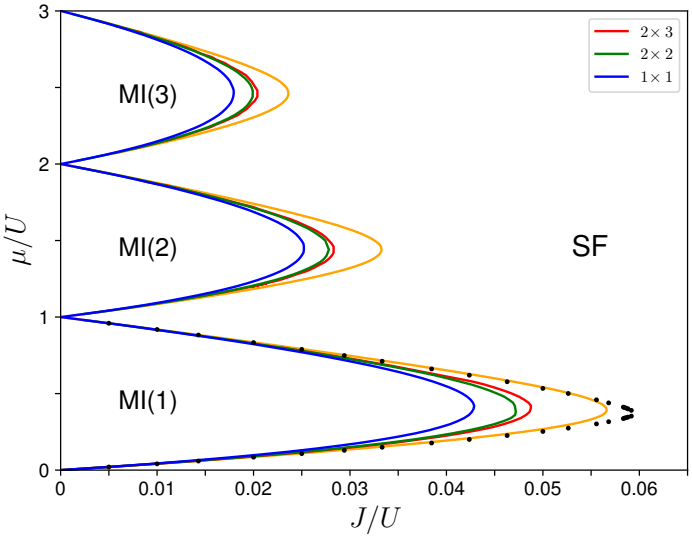

Figure 2.3: Phase diagram of BHM in μ/U vs J/U plane. Blue colored phase boundary is obtained with SGMF method (labelled as 1×1). The MI-SF phase boundary increases with CGMF, as shown with green and red colors for calculations with 2×2 and 2×3 clusters, respectively. Orange colored line represents phase boundary calculated using 3×3 cluster with exact hopping along x-direction. Black open circles are QMC results from Ref [178]. (The data is obtained from personal communication with Prof. Barbara Capogrosso-Sansone.)

tained using the SF order parameter $\phi = \langle \hat{b} \rangle$, which can distinguish the two quantum phases. It is zero in the Mott phase, while in the SF phase ϕ is non-zero. At the tip of the Mott lobe, the MI-SF QPT occurs at fixed integer number density in the two phases in the vicinity of the phase boundary and lies in the equivalence class of 3D XY model [13]. The quantum fluctuations are large near the tip of the Mott lobes, because of which the SGMF method cannot describe the phase boundary accurately. And, away from the tip, the QPT occurs at varying number density.

2.4 Non-equilibrium dynamics

The methods we have discussed so far are to obtain the equilibrium quantum phases. Let us now discuss the physics governing the non-equilibrium dynamics of these quantum phases. We shall assume the closed system dynamics with no couplings to the ex-

ternal surroundings or dissipations. Thus, the dynamics of the quantum phase follow a unitary evolution. Using the variational principle, we derive the equations of state corresponding to the single-site mean-field Hamiltonian $\hat{h}_{p,q}$ [179], the generalization for CGMF follows in a similar way. The Lagrangian at the site (p,q) is

$$L_{p,q} = i\ {}_{p,q}\langle\Psi(t)|\partial_t\,|\Psi(t)\rangle_{p,q} - {}_{p,q}\langle\Psi(t)|\hat{h}_{p,q}\,|\Psi(t)\rangle_{p,q}\,. \tag{2.20}$$

Using Gutzwiller ansatz, $|\Psi(t)\rangle_{p,q} = \sum_n c_n^{(p,q)}(t)\,|n\rangle_{p,q}$, the first term on the right-hand side of Eq. (2.20) assumes the expression

$$\begin{aligned} i\ {}_{p,q}\langle\Psi(t)|\partial_t\,|\Psi(t)\rangle_{p,q} &= i\sum_{m,n} c_m^{(p,q)*}\partial_t c_n^{(p,q)}\ {}_{p,q}\langle m|n\rangle_{p,q} \\ &= i\sum_n c_n^{(p,q)*}\partial_t c_n^{(p,q)}. \end{aligned} \tag{2.21}$$

And the second term on the right-hand side of Eq. (2.20) is given by

$$\begin{aligned} &{}_{p,q}\langle\Psi(t)|\hat{h}_{p,q}\,|\Psi(t)\rangle_{p,q} \\ &= \sum_n -J \Big[\phi^*_{p+1,q}\sqrt{n}c^{(p,q)*}_{n-1}c^{(p,q)}_n + \phi_{p+1,q}\sqrt{n+1}c^{(p,q)*}_{n+1}c^{(p,q)}_n \\ &\quad + \phi_{p-1,q}\sqrt{n+1}c^{(p,q)*}_{n+1}c^{(p,q)}_n + \phi^*_{p-1,q}\sqrt{n}c^{(p,q)*}_{n-1}c^{(p,q)}_n \\ &\quad + \phi^*_{p,q+1}\sqrt{n}c^{(p,q)*}_{n-1}c^{(p,q)}_n + \phi_{p,q+1}\sqrt{n+1}c^{(p,q)*}_{n+1}c^{(p,q)}_n \\ &\quad + \phi_{p,q-1}\sqrt{n+1}c^{(p,q)*}_{n+1}c^{(p,q)}_n + \phi^*_{p,q-1}\sqrt{n}c^{(p,q)*}_{n-1}c^{(p,q)}_n \Big] \\ &\quad + \sum_n \Big[\frac{J}{2}\Big(\phi^*_{p+1,q}\phi_{p,q} + \phi^*_{p-1,q}\phi_{p,q} + \phi^*_{p,q+1}\phi_{p,q} \\ &\qquad + \phi^*_{p,q-1}\phi_{p,q} + \text{h.c.}\Big) + \frac{U}{2}n(n-1) - \mu n\Big] c^{(p,q)*}_n c^{(p,q)}_n. \end{aligned} \tag{2.22}$$

The Lagrange equations of motion

$$\partial_t \frac{\partial L}{\partial(\partial_t c_n^{(p,q)})} = \frac{\partial L}{\partial c_n^{(p,q)}}, \tag{2.23}$$

gives a set of coupled differential equations in terms of the coefficients $c_n^{(p,q)}$ as

$$\begin{aligned} -i\partial_t c_n^{(p,q)} = \quad & -J\left(\phi_{p+1,q} + \phi_{p-1,q} + \phi_{p,q+1} + \phi_{p,q-1}\right)\sqrt{n}c^{(p,q)}_{n-1} \\ & -J\left(\phi^*_{p-1,q} + \phi^*_{p+1,q} + \phi^*_{p,q+1} + \phi^*_{p,q-1}\right)\sqrt{n+1}c^{(p,q)}_{n+1} \end{aligned}$$

$$+\Bigg[\frac{J}{2}\Big(\phi_{p+1,q}\phi^*_{p,q}+\phi_{p-1,q}\phi^*_{p,q}+\phi_{p,q+1}\phi^*_{p,q} +\phi_{p,q-1}\phi^*_{p,q}+\text{h.c.}\Big)+\frac{U}{2}n(n-1)-\mu n\Bigg]c_n^{(p,q)}. \quad (2.24)$$

It is to be noted that the coefficients of the wavefunction at site (p, q) are coupled to the coefficients of the same lattice site only but of different Fock-states. The coupling to the neighbouring lattice sites is due to the mean-field ϕ. The dynamical wavefunction can be obtained by solving the set of coupled differential equations. In our studies related to the dynamical evolution of the state, we use the fourth-order Runge-Kutta (RK4) method to solve the set of coupled differential equations. In a similar way, the equations of motion for the dynamical wavefunction described using CGMF can be obtained by working with the Lagrangian corresponding to the cluster Hamiltonian and deriving the equations of motion.

2.5 Summary of the chapter

To summarize, we have discussed the BHM Hamiltonian, which describes the system of ultracold bosonic atoms in optical lattices. We then discussed the numerical methods for obtaining the equilibrium ground states of the system. This includes the mean-field methods, namely the SGMF and CGMF methods. We have presented the phase diagram of BHM with SGMF and CGMF methods. Towards the end, we have discussed the time dependent Gutzwiller equations for studying the dynamical evolution of a quantum phase. We have utilized these methods in studies related to the ultracold atoms in optical lattices described in this thesis.

Chapter 3

Exact diagonalization technique for bosons on a lattice

Only a handful of quantum many-body system problems can be solved analytically, necessitating the frequent utilization of numerical approaches to gain some insights into these systems. While the numerical mean-field techniques are relatively simple to apply [180], they fall short in capturing the correlation effects and entanglement inherent to the many-body quantum systems. Going beyond the mean-field theory, Quantum Monte Carlo based methods like the stochastic series expansion have proven to be powerful numerical tools [181, 182]. The QMC method is often employed to investigate the systems' approximate properties in the thermodynamic limit. However, it encounters challenges known as "sign problems" for fermionic systems like frustrated quantum spins QMC [183]. Other numerical techniques include the density matrix renormalization group, tensor network methods, to name a few. While various techniques can effectively capture the ground state properties of these systems, solving for the entire Hamiltonian, including the complete eigenspectrum and eigenstates, is a formidable challenge with these methods. The exact diagonalization methods theoretically offer a route to solving the full problem with remarkable precision. In this chapter, we provide an overview of the fundamental components of the ED method and delve into the processes of enumerating basis states, constructing the Hamiltonian matrix, and obtaining the eigenvalues of the Hamiltonian matrix through iterative solvers.

We discuss the ED method for studying the system of cold bosons trapped in a lattice potential. Ultracold atoms trapped in optical lattices serve as excellent proxies to study various condensed matter systems, as they offer superb control and easy tunability over their parameters in the experiments [15, 155, 158]. The ED method offers the advantage of providing a precise solution and access to the full spectrum for these systems, however, it requires heavy computational resources. This imposes severe limitations, and is appropriate for relatively small quantum many-body systems [184]. For example, when dealing with a system of spins arranged on a lattice, the size of the Hilbert space for the system grows exponentially with the lattice size. In the literature, extensive ED investigations of systems such as the spin $1/2$ kagome Heisenberg antiferromagnet exist with approximately 40 to 50 spins [64, 65], as well as the bosonic fractional quantum Hall effect on a 12×4 lattice [82]. For comprehensive insights into the ED technique, valuable references include reviews [61–63, 185, 186].

In this chapter, we present a novel implementation of ED in numerical computations. This method is well-suited for modelling cold bosons confined within optical lattices, where multiple bosons may occupy a single lattice site. In this method, we construct the basis set by systematically building upon single-site Fock states, ultimately forming a hierarchy of wavefunctions consisting of "row-states" and "multi-row states". The Fock states represent the occupation number basis for the lattice site. This hierarchical structure streamlines the implementation of possible constraints to reduce the size of the associated Fock-space, and facilitates the efficient calculation of the Hamiltonian matrix. Furthermore, each stage of our method can be parallelized, thereby significantly enhancing computational speed. While we primarily showcase the application of this method to the Bose-Hubbard model, which describes the ultracold bosons in optical lattices, the proposed method possesses broad applicability across various lattice models. Towards the end of this chapter, we demonstrate the application of the proposed technique for studying the fractional quantum Hall states in optical lattice. We have also discussed how the proposed algorithm can be extended to obtain the reduced density matrix following a spatial bipartitioning of the lattice and study the bipartite entanglement entropy in these states. These symmetry protected topological phases are robust and are of high interest for potential applications

in quantum technologies. We now begin with an overview of the ED procedure.

3.1 Overview

The starting point of the ED method is enumerating a complete set of basis states for the Hamiltonian of the system. For describing the Hamiltonian of lattice models, given in terms of the bosonic creation and annihilation operators, the basis states $\{|\psi_i\rangle\}$ constructed from the Fock-states are the natural choice of basis. Each basis state is then tagged with a sequential index i using techniques such as Lin tables [187], hash [188], or binary search [61]. The next step is to calculate the Hamiltonian matrix elements in terms of the basis states. For the lattice models with restricted itinerancy of the atoms, the Hamiltonian matrix is a sparse matrix with most of the matrix elements equal to zero. Thus, instead of calculating all matrix elements, we only calculate the non-zero elements. The matrix element, $H_{ij} \equiv \langle\psi_i| \hat{H} |\psi_j\rangle$ can be effectively calculated by operating each of the terms in the Hamiltonian on the ket state. The result then identifies the corresponding bra state, which gives a non-zero matrix element. After calculating the Hamiltonian matrix, the last step of the ED method is diagonalizing the Hamiltonian matrix to obtain the eigenvalues and eigenvectors of the Hamiltonian.

For most of the studies on quantum-mechanical systems at low temperatures, the low energy spectrum, namely, the ground state and few excited states, are sufficient to describe the properties of the system. This simplicity allows the usage of well-known Lanczos algorithm for faster numerical diagonalization [173–175]. The Lanczos algorithm is particularly efficient for finding a small subset of eigenvalues and eigenvectors of large, sparse, and symmetric matrices. It avoids the need for explicitly diagonalizing the entire matrix, which can be computationally expensive. Instead, it constructs a smaller tridiagonal matrix whose eigenvalues provide good approximations to those of the original matrix. To understand the main idea of the Lanczos algorithm, let us consider a n-dimensional real symmetric matrix H with a minimal eigenvalue $\lambda_{\min}$. Using a random initial vector $\mathbf{x}$, $\lambda_{\min}$ can be evaluated variationally as

$$\lambda_{\min} = \min_{\mathbf{x}} \frac{\mathbf{x}^\dagger H \mathbf{x}}{\mathbf{x}^\dagger \mathbf{x}}. \tag{3.1}$$

To achieve faster minimization, $\mathbf{x}$ should be varied in the direction opposite to the gra-

dient of $\mathbf{x}^\dagger H\mathbf{x}/\mathbf{x}^\dagger\mathbf{x}$. This direction is spanned by vectors $\mathbf{x}$ and $H\mathbf{x}$. Thus, the minimal solution vector needs to be searched in the space spanned by vectors $\in \{\mathbf{x}, H\mathbf{x}\}$. After k iterations, the best minimal solution lives in the Krylov space spanned by vectors $\in \{\mathbf{x}, H\mathbf{x}, H^2\mathbf{x} \cdots H^{k-1}\mathbf{x}\}$. Constructing an orthonormal basis in this space, can be used to recast the Hamiltonian matrix into a tri-diagonal matrix. With increasing iterations, less than n, the Krylov space approaches an invariant subspace of H, and the eigenvalues determined from the orthonormal basis approach the minimal eigenvalue of H. We shall now discuss the implementation of ED in the context of BHM.

3.2 Implementation

Let us now discuss the construction of the basis set. Starting from the single-site Fock states, we define the basis states in terms of a hierarchy of states with multiple lattice sites along multiple rows of the lattice.

3.2.1 Construction of the row-states

We start with the single-site Fock state $|n_{p,q}\rangle$, corresponding to the occupancy $n_{p,q}$ at lattice site (p, q). For bosons, $n_{p,q}$ can, in principle, assume any non-negative integer value. However, we choose a cutoff on the single-site occupancy such that $0 \leq n_{p,q} < N_B$. Utilizing the single-site Fock states, we construct "row-states" which represent the configuration of particles along a row. The row-states construction is useful as they can be utilized to represent the configuration of particles in multiple rows or the entire lattice. The row-state is defined as the tensor product over the single-site Fock states, given by

$$|\phi_m\rangle \equiv |n_1, n_2, \cdots n_p, \cdots n_K\rangle = \prod_{p=1}^{K} |n_p\rangle\,, \tag{3.2}$$

where, the lattice has dimension $K \times L$. For simplicity, we have omitted the lattice site index along the y direction of the occupancies, as this index is same for all the lattice sites constituting the row. Each row-state $|\phi_m\rangle$ is uniquely identified by a corresponding "quantum number" m, defined as

$$m = \sum_{p=1}^{K} n_p\, N_B^{p-1}. \tag{3.3}$$

Since $0 \leqslant n_p \leqslant N_B - 1$, thus the total number of distinct row-state configurations is given by $\alpha = (N_B)^K$, with the row-state identifier $m \in \{0, 1, 2, \cdots \alpha - 1\}$. It can be easily verified that Eq. (3.3) represents an invertible map, thus allowing the extraction of the configuration of occupancies along the row from the quantum number m of the row-state. The numerical enumeration of row-state configurations involves computing the occupancies n_p corresponding to the quantum number m which can take all possible non-negative integer value less than α. From this, various properties, such as the total number of particles N_m in the row-state $|\phi_m\rangle$ can be computed as

$$N_m = \sum_{p=1}^{K} n_p. \tag{3.4}$$

3.2.2 Hierarchical multi-row states

Using the row-states as the fundamental building blocks, we construct the "multi-row states", which represent the configuration of occupancies within a cluster consisting of multiple rows. For instance, multi-row states consisting of two rows, represented as $\left|\Phi^2\right\rangle$, is obtained from the tensor-product of the row-states, given by

$$\left|\Phi^2_M\right\rangle = |\phi_{m_1}\rangle \otimes |\phi_{m_2}\rangle \,. \tag{3.5}$$

Here, the two-row state label M corresponds to a two-dimensional vector $\mathbf{M} = (m_1, m_2)$, which contains quantum numbers of the constituting row-states. The two-row state label is uniquely identified by $M = \alpha \times m_1 + m_2$ and can take values $0 \leq M < \alpha^2 - 1$. Similarly, a hierarchy of multi-row states of higher ranks, corresponding to higher number of rows can be constructed out of lower-rank multi-row states together with the row-states

$$\begin{aligned} \left|\Phi^3_{M'}\right\rangle &= \left|\Phi^2_M\right\rangle \otimes |\phi_m\rangle \,, \\ \left|\Phi^4_{M'}\right\rangle &= \left|\Phi^2_{M_1}\right\rangle \otimes \left|\Phi^2_{M_2}\right\rangle \,. \end{aligned} \tag{3.6}$$

The multi-row states with q rows, represented as $|\Phi^q_M\rangle$, is thus identified by a vector $\mathbf{M} = (m_1, m_2, \cdots m_q)$ in a q dimensional hyperspace. The components of the vector are the row-state quantum numbers and each axes of the hyperspace correspond to one of the constituting row-states. As mentioned earlier, various q-row multi-row states

are uniquely identified by the multi-row state index M, corresponding to the vector $\mathbf{M}$. The index M and the number of particles in the multi-row state N_M are given by

$$M = \sum_{j=1}^{q} N_B^{K(L-j)} m_j, \text{ and } N_M = \sum_{p=1}^{K} \sum_{j=1}^{q} n_{p,j}. \tag{3.7}$$

Expanding upon the concept of the multi-row states, we construct the basis states for the lattice with L rows and K columns by taking a direct product of two appropriately chosen states, given by

$$\left|\Phi_M^L\right\rangle = \left|\Phi_{M_1}^{L_1}\right\rangle \otimes \left|\Phi_{M_2}^{L_2}\right\rangle, \tag{3.8}$$

such that, $L_1 + L_2 = L$. Similar to the previous cases of multi-row states, each basis state $\left|\Phi_M^L\right\rangle$ is identified by a unique index M, given by Eq. (3.7), and a corresponding L dimensional vector $\mathbf{M} = (m_1, m_2, \cdots m_L)$. Thus, the total number of distinct basis states is α^L. Fig. 3.1 shows schematically a L-dimensional hyper-space, spanned by the row-states $|\phi\rangle_m$ along the L rows of the lattice and each point in this hyper-space corresponds to a possible basis state representing a configuration of particles on a 2D lattice. The basis construction procedure can be summarized as: the configuration of occupancies over the entire lattice, which constitutes a basis state, is identified with a vector with row-state quantum numbers as its constituents. This vector is further identified by the basis index M. The essence of this scheme is shown in the representation shown below.

$$\begin{pmatrix} n_{1,L} & n_{2,L} & \cdots & n_{p,L} & \cdots & n_{K,L} \\ \vdots & \vdots & & \vdots & & \vdots \\ n_{1,q} & n_{2,q} & \cdots & n_{p,q} & \cdots & n_{K,q} \\ \vdots & \vdots & & \vdots & & \vdots \\ n_{1,2} & n_{2,2} & \cdots & n_{p,2} & \cdots & n_{K,2} \\ n_{1,1} & n_{2,1} & \cdots & n_{p,1} & \cdots & n_{K,1} \end{pmatrix} \equiv \begin{pmatrix} m_L \\ \vdots \\ m_q \\ \vdots \\ m_2 \\ m_1 \end{pmatrix} \equiv M$$

Thus, any state of the system can be expressed as a linear combination of these basis states with complex coefficients C^M, given by

$$|\psi\rangle = \sum_{M=0}^{\alpha^L - 1} C^M \left|\Phi_M^L\right\rangle. \tag{3.9}$$

After constructing the basis states, the next step is the calculation of the Hamiltonian matrix.

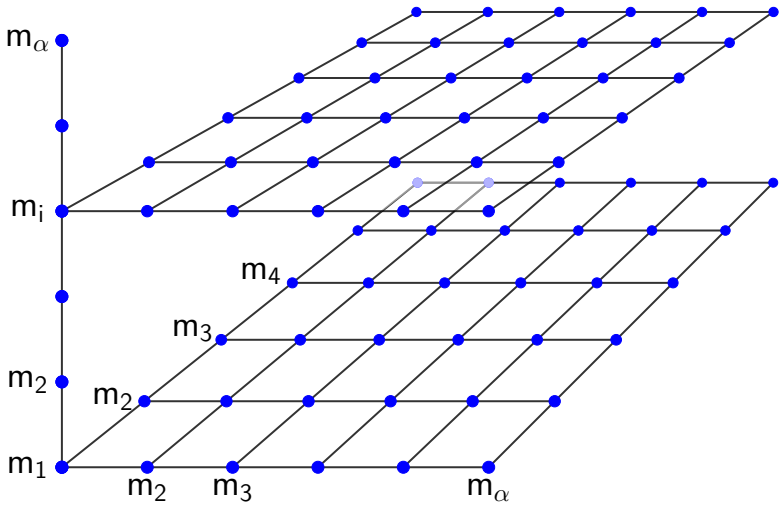

Figure 3.1: Schematic showing the basis states identified by a point in the 3-dimensional space spanned by row-states, for a lattice with 3 rows.

3.2.3 Construction of the Hamiltonian matrix

Let us consider the BHM as the model Hamiltonian for which we shall discuss the matrix construction procedure. The BHM Hamiltonian is given by [13, 14, 44]

$$\hat{H}_{\text{BHM}} = \sum_{p,q} \left[-J\left(\hat{b}^\dagger_{p+1,q}\hat{b}_{p,q} + \hat{b}^\dagger_{p,q+1}\hat{b}_{p,q} + \text{H.c.}\right) + \frac{U}{2}\hat{n}_{p,q}(\hat{n}_{p,q}-1) - \mu\hat{n}_{p,q}\right] \quad (3.10)$$

where p, q are lattice site coordinates along the x and y directions. Due to the restricted hopping to nearest neighboring lattice sites only, the BHM Hamiltonian matrix is sparse with a lots of zero. Thus, instead of naively calculating the matrix element by looping over all bra and ket states, we only compute the non-zero elements which saves a lot of computational time.

Let us first consider the action of the x-hopping term $-J\hat{b}^\dagger_{p+1,q}\hat{b}_{p,q}$ on the basis state $\left|\Phi^L_M\right\rangle$. The x-hopping affects the occupancies at only two lattice sites (p,q) and $(p,q+1)$ along the qth row. This hopping results in a non-zero action, if the occupancies in the ket state is such that $n_{p,q} \geqslant 1$ and $n_{p+1,q} \leqslant N_B - 1$, with the action on qth row occupancies given by

$$\begin{aligned} \hat{b}^\dagger_{p+1,q}\hat{b}_{p,q} \quad & |n_{1,q}, \cdots n_{p,q}, n_{p+1,q} \cdots n_{K,q}\rangle \\ = \quad & \sqrt{n_{p,q}\left(n_{p+1,q}+1\right)}\,|n_{1,q}, \cdots (n_{p,q}-1), (n_{p+1,q}+1) \cdots n_{K,q}\rangle \,. \end{aligned} \quad (3.11)$$

Thus, this hopping term only modifies the row-state $|\phi\rangle_{m_q}$ at the qth row of the basis state to a different row-state $|\phi\rangle_{m'_q}$. And, the quantum numbers of the two row-states are related as

$$\begin{aligned} m'_q - m_q &= \sum_{j=1}^{K} (n'_{j,q} - n_{j,q})\, N_B^{j-1}, \\ &= (n'_{p+1,q} - n_{p+1,q})\, N_B^{p} + (n'_{p,q} - n_{p,q})\, N_B^{p-1}, \\ &= N_B^p - N_B^{p-1} = N_B^{p-1}\big(N_B - 1\big), \end{aligned} \tag{3.12}$$

since $n'_{p+1,q} = n_{p+1,q} + 1$ and $n'_{p,q} = n_{p,q} - 1$ for the x-hopping along the qth row in the +ve direction. Thus, for an allowed x-hopping in the +ve direction along the qth row, the matrix element has the value

$$\begin{aligned} (-J\hat{b}^\dagger_{p+1,q}\hat{b}_{p,q})_{M'M} \equiv & \quad {}_{M'}\left\langle \Phi^L \right| - J\hat{b}^\dagger_{p+1,q}\hat{b}_{p,q} \left| \Phi^L_M \right\rangle \\ = & \quad -J\sqrt{n_{p,q}\,(n_{p+1,q}+1)}. \end{aligned} \tag{3.13}$$

where the vectors $\mathbf{M} = (m_1, m_2, \cdots m_L)$ and $\mathbf{M'} = (m'_1, m'_2, \cdots m'_L)$ are related as

$$m'_j = \begin{cases} m_j & \text{if } j \neq q, \\ m_q + N_B^{p-1}\,(N_B - 1) & \text{if } j = q. \end{cases} \tag{3.14}$$

This follows from the fact that x-hopping along the qth row modifies the occupancies and hence changes only the row-state quantum number of the qth row as given by Eq. (3.14).

Similarly, the y-hopping term $-J\hat{b}^\dagger_{p,q+1}\hat{b}_{p,q}$ modifies the row-states at q and $q+1$ rows of the basis state, the row-state quantum numbers satisfy the relations

$$\begin{aligned} m'_q - m_q &= (n'_{p,q} - n_{p,q})\, N_B^{p-1} = -N_B^{p-1} \\ m'_{q+1} - m_{q+1} &= (n'_{p,q+1} - n_{p,q+1})\, N_B^{p-1} = N_B^{p-1} \end{aligned} \tag{3.15}$$

For a possible y-hopping, along the pth column in the +ve direction, the non-zero matrix element is given by

$$(-J\hat{b}^\dagger_{p,q+1}\hat{b}_{p,q})_{M'M} = -J\sqrt{n_{p,q}\,(n_{p,q+1}+1)}\,, \tag{3.16}$$

where,

$$m'_j = \begin{cases} m_j & \text{if } j \neq q, j \neq q+1, \\ m_q - N_B^{p-1} & \text{if } j = q, \\ m_{q+1} + N_B^{p-1} & \text{if } j = q+1. \end{cases} \tag{3.17}$$

In a similar manner, the hermitian conjugate of the hopping terms in the Hamiltonian can be evaluated. The on-site interaction term and chemical potential term depend on the number operator only. These terms thus contribute to the diagonal elements of the Hamiltonian matrix and are straightforward to compute. Using these schemes, we can complete the calculation of the Hamiltonian matrix and diagonalizing it gives the required eigenspectrum. However, it should be emphasized that in certain cases, it is possible to filter out some of the basis states by imposition of constraints. We refer to this filtering process, as the "state reduction", and it can significantly reduce the Fock-space dimension, thereby reducing the demand for heavy computational resources. In the next section, we shall discuss the basis construction and Hamiltonian matrix construction procedures with state reduction.

3.3 Exact Diagonalization with State Reduction

So far, we have only imposed the constraint on the single-site occupancies $n_{p,q}$ so that it can be atmost equal to $N_B - 1$. Thus, the basis states constructed in terms of the row-states and multi-row states include all possible values for total number of particles in the lattice N, varying in the range $0 \leqslant N \leqslant (N_B - 1)^{KL}$. For BHM like Hamiltonians, which preserve the total number of particles, micro-canonical studies with fixed N can be done by filtering out the basis states appropriately. This also implies that $0 \leqslant n_{p,q} \leqslant \min(N, N_B - 1)$. Additional constraints for filtering the basis states can also be imposed depending upon the system of interest. For instance, at unit filling $(N = K \times L)$ and strong contact interactions, the average occupancy ≈ 1. Thus, basis states with large fluctuations in occupancies away from $n_{p,q} \approx 1$ may contribute to higher excitations and can be filtered out, leading to a reduction in Fock-space dimension. These state reduction considerations, however, require some modifications in the earlier discussed procedures for basis construction and Hamiltonian matrix calculation, as discussed in upcoming sections.

3.3.1 Row-states with constraints

The state reduction process starts at the level of the single-site Fock states, with the single site occupancies $n_{p,q}$, constrained as

$$\eta \leqslant n_{p,q} \leqslant N_B - 1. \tag{3.18}$$

This constraint modifies the lowest possible occupancy to η and redefines the total choices for the single-site occupancies to $N_B - \eta$. This type of constraint is suitable for describing the quantum states with higher average occupancies. It should be noted that this constraint also puts a lower bound on the total number of particles in the row as $N_m \geqslant \eta\, K$ and in the entire lattice by $N \geqslant \eta\, K \times L$. In a similar way, the total number of particles in any row of the basis states can be constrained within the range

$$\sigma \leqslant \sum_{p=1}^{K} n_{p,q} \leqslant \sigma + \delta. \tag{3.19}$$

Here, $\sigma \geqslant \eta K$ represents the minimum number of particles along any row and sets the number fluctuations to $\delta \leqslant (N_B - 1 - \eta)K$. This type of constraint is suitable to study quantum phases with lower number fluctuations. The lower (upper) bound σ ($\sigma + \delta$) on N_m should be appropriately chosen according to the number fluctuations in the quantum phase of interest.

For constructing the row-states, we can still use Eq. (3.2) together with the constraints in Eq. (3.18) and (3.19), and the row-state quantum number can be obtained using Eq. (3.3). However, to avoid large values of m which may result in integer overflow in defining the multi-row quantum numbers, it is suitable to shift the occupancies by η while calculating the row-state quantum number, as given by

$$m = \sum_{p=1}^{K} (n_p - \eta)\,(N_B - \eta)^{p-1}. \tag{3.20}$$

It should be noted that with the constraints, the quantum number m doesn't vary uniformly and may not assume consecutive integer values. This can be observed from Table A.1 in Appendix A, where we illustrate the construction of row-states with an example. Thus, for the purpose of book keeping, m is unsuitable as an index for labelling. So, let us consider the set formed by quantum numbers m, arranged in ascending order, for the possible row-states which are β in number: $\mathcal{S} = \{m_i : m_i < m_{i+1}$ and $i, i{+}1 \in$

$\mathcal{S}'\}$. Here, the sequence label i which forms the index set $\mathcal{S}' = \{1, 2, \cdots \beta\}$ can be used for indexing the row-states as $|\phi\rangle_i \equiv |\phi_{m_i}\rangle$. In this way, the row-state with lowest value of m is assigned the index $i = 1$ and the state with second lowest value of m is assigned $i = 2$ and so on. Thus, the ordering in the row-states is ensured by the quantum numbers m. As described earlier, we construct the basis states in terms of a hierarchy of states with multiple rows using these constrained row-states as the fundamental building blocks. This procedure, modified appropriately due to constraints, is described in the next section.

3.3.2 Multi-row states with constraints

Similar to the constraints applied at the level of single-site and row-states, given in Eq. (3.18) and (3.19), respectively, the total number of particles in the entire lattice N can be constrained as

$$\Sigma \leqslant \sum_{p=1}^{K} \sum_{q=1}^{L} n_{p,q} \,, \leqslant \Sigma + \Delta, \tag{3.21}$$

Here, $\Sigma \geqslant \eta KL$ sets a lower limit on the number of particles in the basis states and Δ sets the range of N. This type of constraint is suitable for the studies where total number of particles in the lattice is not fixed. However, for micro-canonical studies with fixed N, Δ is set to 0. The constraints in Eq. (3.18), (3.19) and (3.21), chosen appropriately to describe the quantum phase of interest, can reduce the basis set to an optimal size.

Similar to the previous case, the q-rows states are denoted by $|\Phi^q_M\rangle$, with a vector $\mathbf{M}$ identifying the row-states configurations in the constituting q rows. The two-row states is constructed out of tensor product of two row-states as

$$\left|\Phi^2_M\right\rangle \equiv |\phi_{m_1}\rangle \otimes |\phi_{m_2}\rangle : N_M \leqslant \Sigma + \Delta \tag{3.22}$$

Here, $\mathbf{M} = (m_1, m_2)$ contains the row-state quantum numbers of the two contributing row-states satisfying the global constraint on maximum number of particles in the lattice to be atmost $\Sigma + \Delta$. It should be noted that the number of two-row states can be additionally reduced with the imposition of more complex constraints on N_M, however, these constraints should be appropriate to the quantum phase of interest. Thus, each two-row state $\left|\Phi^2_M\right\rangle$ is uniquely identified by the vector label $\mathbf{M}$ which can be

mapped to a integer label $M = \|\mathbf{M}\| = \sum_{j=1}^{2} m_j (N_B - \eta)^{K(L-j)}$. This mapping is similar to Eq. (3.7) except for a shift in N_B by η done to avoid large integer values. Similar to the row-state quantum number, the integer label M of the two-row states may not assume consecutive integer values due to the state-reduction constraints and is thus unsuitable as an index for these states. So, we use the strategy adopted in the case of row-states for indexing the two-row states. Consider the set formed by the two-row state quantum numbers, $\beta^{(2)}$ in number, arranged in an ascending sequence: $\mathcal{S} = \{M_I : M_I < M_{I+1}, \text{ and } I, I+1 \in \mathcal{S}'\}$. Here, the sequence label I, which forms the index set $\mathcal{S}' = \{1, 2, \cdots \beta^{(2)}\}$ is used for indexing the two-row states. In this way, the Ith two-row state, represented as $\left|\Phi^2\right\rangle_I \equiv \left|\Phi^2_{M_I}\right\rangle$, is uniquely identified by M_I, which inturn identifies the pair of the constituent row-states (m_1, m_2). In other words, each two-row state is identified with a integer index I, sequenced according to the quantum number of the two contributing row-states. The sequence is defined in terms of the ordered pair (m_1, m_2), with the left quantum number m_1 as slower varying with I. And, the two-row state with the lowest possible values of m_1 followed by the lowest possible values of m_2 is assigned the index $I = 1$. This definition is also consistent with the previous ordering scheme defined by Eq. (3.7). Table A.2 in Appendix A illustrates as an example the ordering for the two-row states. It should be noted that the number of possible two-row states $\beta^{(2)} \leqslant (\beta)^2$. Following similar steps, multi-row states with larger number of rows can be constructed using multi-row states with lower number of rows and the row-states.

Continuing in a similar fashion, the basis states for entire lattice are generated. For this purpose, we can utilize atmost two appropriate multi-row states and/or row-states, satisfying the constraints on total number of particles in the lattice, given in Eq. (3.21). For instance, the basis states for lattice with $L = 3$ are selected from the set $\{\left|\Phi^3_M\right\rangle\}$ as

$$\left|\Phi^3\right\rangle_I \in \{\left|\Phi^3_M\right\rangle\} : \Sigma \leqslant N_{M'} \leqslant \Sigma + \Delta. \tag{3.23}$$

Similar to the previous cases, each basis state is assigned with a unique integer index $I \in \{1, 2, \cdots \Gamma\}$, with $\Gamma \leqslant \beta^{(3)}$ being the total number of possible basis states for the entire lattice. Similarly, for a larger lattice of dimension $K \times L$, multi-row states of

lower ranks are utilized for basis construction as

$$\left|\Phi^{L}\right\rangle_{I} = \left|\Phi^{L_1}_{M_1}\right\rangle \otimes \left|\Phi^{L_2}_{M_2}\right\rangle : \Sigma \leqslant N_I = N_{M_1} + N_{M_2} \leqslant \Sigma + \Delta, \tag{3.24}$$

where, $L = L_1 + L_2$. With the set of basis states $\{\left|\Phi^{L}\right\rangle_{I}\}$, any state of the system can be expressed as a linear combination $|\Psi\rangle = \sum_{I=1}^{\Gamma} C^I \left|\Phi^{L}\right\rangle_{I}$, with C^I being the coefficient of the basis state $\left|\Phi^{L}\right\rangle_{I}$.

3.3.3 Calculation of Hamiltonian matrix

Let us again consider the BHM Hamiltonian given in Eq. (5.8), and discuss the operation of $x-$hopping term $-J\hat{b}^{\dagger}_{p+1,q}\hat{b}_{p,q}$ on the basis states. It's action can be evaluated in a similar way as given in the expressions in Eq. (3.11-3.12). Thus, for any Ith basis state with vector $\mathbf{R}$ containing the information of row-state components, a valid x-hopping results in

$$-J\hat{b}^{\dagger}_{p+1,q}\hat{b}_{p,q}\left|\Phi^{L}_{R}\right\rangle = -J\sqrt{n_{p,q}\left(n_{p+1,q}+1\right)}\left|\Phi^{L}_{R'}\right\rangle. \tag{3.25}$$

The action of hopping term has transformed the ket basis state $\left|\Phi^{L}_{R}\right\rangle$ into $\left|\Phi^{L}_{R'}\right\rangle$. As previously calculated, the corresponding vectors of the two basis states $\mathbf{R} = (r_1, r_2, \cdots r_L)$ and $\mathbf{R}' = (r'_1, r'_2, \cdots r'_L)$ are related by $r'_j = r_j$ for $j \neq q$ and $r'_q = r_q + N_B^{p-1}\left(N_B - 1\right)$. Thus, we have uniquely identified the bra state with vector $\mathbf{R}'$ that gives a non-zero matrix element for the considered hopping on the chosen ket state. However, the basis index of corresponding to $\left|\Phi^{L}_{R'}\right\rangle$ is yet unknown. Once the corresponding basis index is identified, we have the knowledge of the Hamiltonian matrix element $H_{II'} = \left\langle\Phi^{L}_{R'}\right| H_{\text{BHM}} \left|\Phi^{L}_{R}\right\rangle$. This process continued for all the terms in the Hamiltonian generates the Hamiltonian matrix. Let us now discuss the much needed identification scheme for locating the basis index I from the corresponding vector label of the basis state.

As previously mentioned, the Ith basis state $\left|\Phi^{L}\right\rangle_{I}$ is tagged with a corresponding vector label $\mathbf{M} = (m_1, m_2, \cdots, m_L)$ containing the row-state quantum number information of the constituent rows. This constitutes a forward map from the basis state index j to the row-state quantum numbers contained in the vector label $\mathbf{M}$

$$\left|\Phi^{L}\right\rangle_{j} \rightarrow |\phi_{m_1}\rangle \otimes |\phi_{m_2}\rangle \cdots \otimes |\phi_{m_L}\rangle \equiv |\phi\rangle_{i_1} \otimes |\phi\rangle_{i_2} \cdots \otimes |\phi\rangle_{i_L}. \tag{3.26}$$

In order to resolve the inverse map, let us recall the structure adopted in the basis set construction process. The row-states, total β in number, are identified with a positive integer index i and the corresponding quantum number m. And the basis states $\left|\Phi^L\right\rangle_I$, are identified with vector $\mathbf{M} = (m_1, m_2, \cdots m_L)$ and corresponding row-state indexes $(i_1, i_2, \cdots i_L)$, together with the convention that the left component i_q varies slower than i_{q+1} with the basis index I. As an example, we illustrate the ordering in the basis state index with the row-state indexes in Table 3.1.

I	$(i_1, i_2, \cdots i_{L-1}, i_L)$
1	$(1,\ 1,\ \cdots 1,\ 1)$
2	$(1,\ 1,\ \cdots 1,\ 2)$
$\vdots$	$\vdots\ \ \vdots\ \ \ \ \vdots\ \ \vdots$
I_1	$(1,\ 1,\ \cdots 1,\ \beta)$
I_1+1	$(1,\ 1,\ \cdots 2,\ 1)$
$\vdots$	$\vdots\ \ \vdots\ \ \ \ \vdots\ \ \vdots$
I_2	$(1,\ 1,\ \cdots 2,\ \beta)$
$\vdots$	$\vdots\ \ \vdots\ \ \ \ \vdots\ \ \vdots$
I_3	$(1,\ 1,\ \cdots \beta,\ \beta)$
$\vdots$	$\vdots\ \ \vdots\ \ \ \ \vdots\ \ \vdots$
I_4	$(1,\ \beta,\ \cdots \beta,\ \beta)$
I_4+1	$(2,\ 1,\ \cdots 1,\ 1)$
$\vdots$	$\vdots\ \ \vdots\ \ \ \ \vdots\ \ \vdots$
I_5	$(2,\ \beta,\ \cdots \beta,\ \beta)$
$\vdots$	$\vdots\ \ \vdots\ \ \ \ \vdots\ \ \vdots$
Γ	$(\beta,\ \beta,\ \cdots \beta,\ \beta)$

Table 3.1: Table showing sequentially ordered all possible basis-states and the row-state indexes i_q.

Let us suppose that we want to locate the basis index I corresponding to the basis state with row-state configuration $\mathbf{R}' = (i'_1, i'_2, \cdots, i'_L)$. For this purpose, we perform bisection search in the interval $I \in [1, \Gamma]$. Since the leftmost component i_1 is the

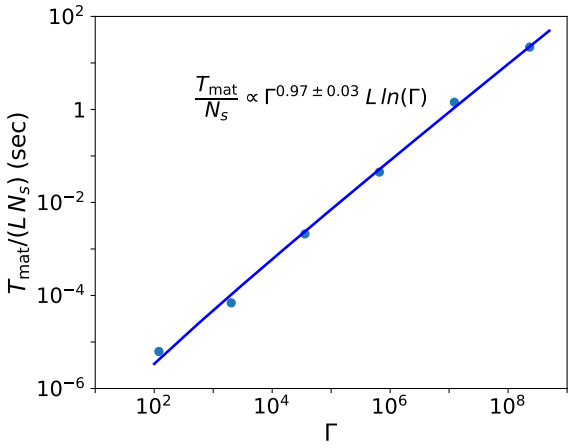

Figure 3.2: Dependence of the computation time T_{mat} involved in matrix construction as a function of the size of the basis set.

slowest varying and thus increase monotonically with I, we use the bisection method to locate the range of basis index $I \in [I^1_{\text{min}}, I^1_{\text{max}}]$ for which the leftmost row-state index satisfy $i_1 = i'_1$. Now, within this range of I, the row-state index i_2 increases monotonically with I. Hence, a bisection search can be employed in this range to locate the range $[I^2_{\text{min}}, I^2_{\text{max}}]$ for which $i_2 = i'_2$ At this stage, all the basis states $\left|\Phi^L\right\rangle_I$ with I in the range $[I^2_{\text{min}}, I^2_{\text{max}}]$ have the desired row-states configurations in two rows with $q = 1$ and $q = 2$. Continuing in a similar manner, we keep on bisecting the previously obtained interval $[I^y_{\text{min}}, I^y_{\text{max}}]$ to obtain a smaller interval $[I^{y+1}_{\text{min}}, I^{y+1}_{\text{max}}]$ with desired configuration of row-state in the row $q = y + 1$. Finally, the required basis state index I is obtained in the Lth bisection step. Thus, the inverse map that locates the basis index, from a given row-state configurations of the basis state, is obtained through a sequence of L bisection searches. And, each bisection search requires atmost $ln_2(\Gamma)$ comparisons of the quantum numbers.

With this identification scheme, we can construct the full Hamiltonian matrix. Starting with a ket state $\left|\Phi^L\right\rangle_I$, we identify the corresponding bra states ${}_{I'}\left\langle\Phi^L\right|$ and the non-zero matrix element for all the terms in the Hamiltonian. The full Hamiltonian matrix is constructed by looping over all possible ket states.

Fig. 3.2 shows the scaling of the computation time elapsed in the matrix construction T_{mat}, as a function of the basis set dimension Γ. It is expected that T_{mat} should depend on the number of hopping terms, which is proportional to the num-

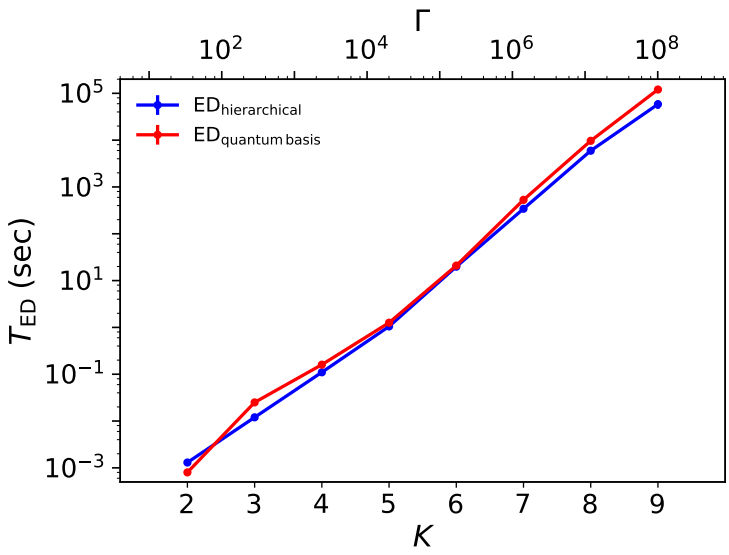

Figure 3.3: Comparison of our ED code, based on hierarchical wavefunctions and bisection searches, with an open source ED package: "quantum basis" which is a C language based ED library for general models and is available at github [189]. Along y-axis, total time elapsed in computing the ground state is plotted for a system of hardcore bosons at density $= 1/4$ on a lattice of dimension $K \times 4$, for which the total basis states are Γ in number. The error bars represents the time difference based on several runs.

ber of lattice sites N_s. For Γ possible ket states, and together with the identification of the bra state with non-zero matrix element in $L\,ln(\Gamma)$ number of steps, it is expected that $T_{\rm mat}/N_s$ should scale $\sim \Gamma ln(\Gamma) L$. For the BHM matrix with hardcore bosons at fixed number density $N/N_s = 1/8$ on a 2D lattice of dimension $8 \times L$, with $L \in \{2, 3, 4, 5, 6, 7\}$, Fig. 3.2 shows the computational time as a function of Γ. We note that $T_{\rm mat}/N_s \propto \Gamma^{0.97\pm0.03}\, L\, ln(\Gamma)$ which is quite close to the expected dependence. This is drastically lower than the quadratic dependence with Γ, if we have resorted to calculating all the matrix elements by looping over all possible ket and bra states.

To benchmark the proposed ED technique based on hierarchical wavefunctions for basis construction and bisection searches to calculate the Hamiltonian matrix elements, we compare it with a standard ED library named "quantum basis" available at github [189]. The "quantum basis" ED library is written in C language and utilizes the

concept of "Lin Tables" for basis identification. In addition, it has the advantage of utilizing all the cpu threads available in a cpu core. For benchmarking the two methods, we compare the total time elapsed in obtaining the ground state wave-function. We ran the two ED codes on a single cpu node of a HPC cluster which have 256GB memory, with each cpu capable of hosting two threads. Fig. 3.3 shows the comparison of the total time (T_{ED}) elapsed for the two codes as a function of the lattice size and corresponding basis set dimension Γ. For this study, we have chosen a system of hardcore bosons at fixed density of $1/4$ bosons across various lattices with dimensions 2×4, 3×4, $\cdots$, and 9×4. For matrix diagonalization, both the codes use the ARPACK library based on implicitly restarted Arnoldi method with same set of parameter values and takes similar amount of time. However, the basis construction procedure using hierarchical wavefunctions offers advantages and is superior, particularly for larger lattice dimensions as can be seen from Fig. 3.3.

After obtaining the ground state wavefunction, we can investigate the entanglement characteristics of the state. The entanglement between the spatial parts of the system, referred to as the spatial bi-partite entanglement, can be studied by bipartitioning the lattice wavefunction in terms of the degrees of freedom associated with the two halves of the lattice. The structure employed in the basis state construction using hierarchical wavefunctions or the multi-row states is useful in this regard. We shall discuss this in detail in the next section.

3.4 Entanglement in the quantum phase

The entanglement characteristics of a system provide valuable insights into its topological properties. This is particularly useful for distinguishing the topologically ordered phases, such as the quantum Hall phase, from normal phases, like the superfluid. Among the various measures of entanglement within a system, the bipartite entanglement entropy is robust. The bipartitioning in real-space is achieved by dividing the lattice system into two subsystems, denoted as A and B. The many-body wavefunction of the system can then be expressed in a Schmidt-decomposed form [190]

$$|\Psi\rangle = \sum_i \sqrt{\lambda_i}\, |\Psi_{\mathrm{A}}\rangle \otimes |\Psi_{\mathrm{B}}\rangle\,, \tag{3.27}$$

where, λ_i are the Schmidt coefficients that contain the entanglement characteristics between the two sub-systems. These coefficients are identically equivalent to the eigenvalues of the reduced density matrix of the sub-system. The reduced density matrix for sub-system A is given by the density matrix of the full system traced over the degrees of freedom associated with sub-system B, $\rho_{\mathrm{A}} = Tr_{\mathrm{B}} |\Psi\rangle \langle\Psi|$. The eigen-spectrum λ_i of the reduced density matrix gives the entanglement spectra. And the bi-partite entanglement entropy can be inferred from the Von Neumann entropy, given by

$$S_E = -\mathrm{Tr}[\rho_{\mathrm{A}} \log \rho_{\mathrm{A}}] = -\sum_i \lambda_i \log \lambda_i. \tag{3.28}$$

For topological phases such as quantum Hall, the entanglement entropy S_E follows the area law and scales with the length (L) of the boundary between the two sub-systems as [191, 192]

$$S_E = \alpha L - \gamma + \mathcal{O}(L^{-\nu}) \ , \ \nu > 0. \tag{3.29}$$

The Area-law scaling of the entanglement is typical of ground states for gapped systems [193]. The constant term $-\gamma$, called the topological entanglement entropy, is a universal property of the state and depends on the topological order. For example, the topologically ordered $\nu = 1/m$ fractional quantum Hall state has $\gamma = 1/2 \log(m)$. It is also a measure of the quantum dimension of the quasiparticle excitations in the FQH states. Now, we shall discuss the procedure for spatial bipartitioning for studying the bipartite entanglement.

3.4.1 Constructing bipartite reduced density matrix

The methodology utilized in constructing the basis set can be optimally applied to compute the bipartite reduced density matrix. To do this, let's consider dividing a lattice system with L rows into two subsystems, where subsystem A encompasses the lower L_1 rows, while subsystem B comprises the upper $L_2 = L - L_1$ rows, as illustrated in Fig. 3.4. Following Eq. (3.24), each basis state comprising of L row states can be expressed as

$$\left|\Phi_M^L\right\rangle \equiv \left|\Phi_{M_1}^{L_1}\right\rangle \otimes \left|\Phi_{M_2}^{L_2}\right\rangle : \Sigma \leqslant N_{M_1} + N_{M_2} \leqslant \Sigma + \Delta. \tag{3.30}$$

Thus, each basis state $\left|\Phi_M^L\right\rangle$, labelled with the index I, can be thought of as a direct product of multi-row states $\left|\Phi_{M_1}^{L_1}\right\rangle$ and $\left|\Phi_{M_2}^{L_2}\right\rangle$ with multi-row state index I_1 and I_2,

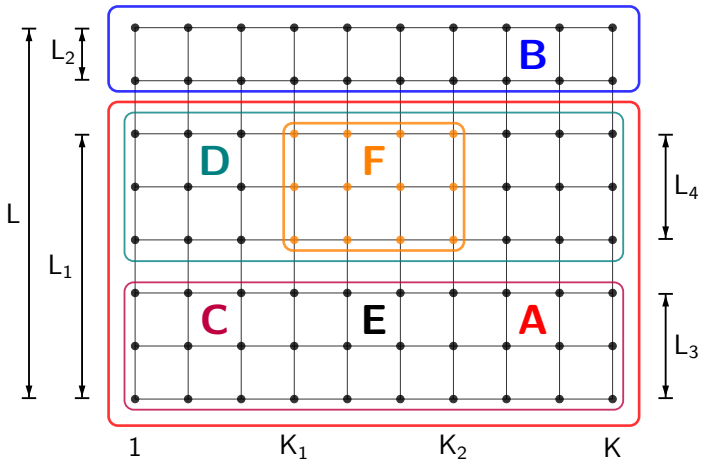

Figure 3.4: Schematic illustration of spatial bipartitioning of the lattice. For partitioning the lattice into sub-system F and the rest, we follow a stepwise process. Initially, the lattice is split along the y-axis into sub-systems, A and B. Next, sub-system A is further divided into sub-systems C and D. Ultimately, sub-system D is partitioned along the x-axis, resulting in the sub-system F. The boundaries of these sub-systems are distinguishable by their respective color-coded labels. Sub-system E, which surrounds sub-system F, is represented by the lattice sites colored in black.

respectively. The reduced density matrix of subsystem A, $\rho_{\rm A}$, of dimension $\beta^{(L_1)}$ is obtained from the density matrix of the entire lattice, $\rho = |\Psi\rangle\langle\Psi|$, after tracing over the degrees of freedom associated with multi-row state of subsystem B, identified by I_2,

$$\begin{aligned}\rho_{\rm A}(k,l) &= \sum_{I=1}^{\Gamma}\sum_{I'=1}^{\Gamma} C^{*I}\, C^{I'}\, \delta_{I_2,I'_2}\, \delta_{I_1,k}\, \delta_{I'_1,l} \\ &= \sum_{I=1}^{\Gamma}\sum_{I'=1}^{\Gamma} \rho(I,I')\, \delta_{I_2,I'_2}\, \delta_{I_1,k}\, \delta_{I'_1,l}. \end{aligned} \tag{3.31}$$

Similarly, sub-system A can be further subdivided into sub-systems C and D, where sub-system C consists of lower L_3 rows and subsystem D comprises of upper $L_4 = L_1 - L_3$ rows. Consequently, the sub-system A state $\left|\Phi_M^{L_1}\right\rangle$, labelled with index I for $1 \leqslant I \leqslant \beta^{(L_1)}$, can be written as a direct product of states of these two subsystems. The states of sub-systems C, $\left|\Phi^{L_3}\right\rangle_{M_3}$, are identified with the index $1 \leqslant I_3 \leqslant \beta^{(L_3)}$. And for sub-system D, the states, $\left|\Phi^{L_4}\right\rangle_{M_4}$, are identified with index $1 \leqslant I_4 \leqslant \beta^{(L_4)}$.

Thus, the reduced density matrix of sub-system D, $\rho_{\rm D}$ which is a $\beta^{(L_4)}$ dimensional matrix, can be obtained as

$$\rho_{\rm D}(k,l) = \sum_{I=1}^{\beta^{(L_1)}} \sum_{I'=1}^{\beta^{(L_1)}} \rho_{\rm A}(I,I')\, \delta_{I_3,I'_3}\, \delta_{I_4,k}\, \delta_{I'_4,l}\,. \tag{3.32}$$

The previous discussions on bi-partitioning of the system have focused on separation along the rows, as illustrated by the sublattices A and B in Fig. 3.4. However, in accordance with the approach outlined in Ref. [191], calculating entanglement entropy necessitates bi-partitioning the system into an isolated part and the surrounding domain. This is illustrated in Fig. 3.4 by the isolated subsystem F and the remaining part E. In this figure, the subsystem F is constituted by orange colored lattice sites, while the rest of the lattice sites in black colors form the subsystem E. The orange colored boundary separates the subsystems F and E. In this scenario, partitioning occurs both along rows and columns. To compute the reduced density matrix of the subsystem F, we follow a two-step process. First the subsystems B and C can be traced out using the method discussed earlier. Subsequently, the sub-system D is partitioned into sub-system F and the remaining lattice sites which forms a part of the sub-system E as shown in Fig. 3.4. The surrounding of subsystem F corresponds to black-colored lattice sites which constitutes the subsystem E. This partitioning involves tracing out columns on both the left and right sides of the subsystem F. The lattice sites (p,q) with $L_3+1 \leqslant q \leqslant L_1$ and $p \in \{K_1, K_1+1, \cdots p, \cdots K_2\}$ belong to sub-system F, while the remaining sites are a part of sub-system E which are subject to tracing out. For this purpose, it becomes necessary to introduce of a unique label corresponding to the various configuration of occupancies in the sub-system F. For relatively lesser number of sites in the subsystem F, we can adopt the following approach for assigning a unique label $\tilde{m}$ to each configuration, given by

$$\tilde{m} = \sum_{q=L_3+1}^{L_1} \sum_{p=K_1}^{K_2} (n_{p,q} - \eta)\, N_B^{(p-K_1)+(L_1-q)(K_2-K_1+1)}. \tag{3.33}$$

Now, corresponding to each multi-row state I of sub-system D, the configuration of particles in the sub-system F is assigned a label $\tilde{m}$ given by Eq. (3.33). Thus, the reduced density matrix of sub-system F is given by

$$\rho_{\rm F}(k,l) = \sum_{I=1}^{\beta^{(L_4)}} \sum_{I'=1}^{\beta^{(L_4)}} \rho_{\rm D}(I,I') \delta_{\tilde{m},k} \delta_{\tilde{m}',l} \prod_{p,q}{}' \delta_{n_{p,q},n'_{p,q}}, \tag{3.34}$$

where $n_{p,q}$ and $n'_{p,q}$ are the occupancies at lattice site (p, q) corresponding to the multi-row states with indexes I and I', respectively. And, the prime over the product signifies restriction on the lattice sites with coordinates given by $p \in \{1, 2, \cdots K_1 - 1, K_2 + 1, \cdots K\}$ and $q \in \{L_3 + 1, L_3 + 2, \cdots L_1\}$.

It should be noted that if the total number of lattice sites in sub-system F is large, then assigning a label to the configurations using Eq. (3.33) is not manageable. Instead, we can then construct the multi-row states using newly constructed row-states with $K_2 - K_1$ sites along the row. Now, each configuration of occupancies in sub-system F can then be uniquely identified with the multi-row index described earlier. It should be mentioned that reduced density matrix is not a sparse matrix in comparison to the Hamiltonian matrix. Thus, Lanczos algorithm is not suitable anymore for the diagonalization purpose and extraction of the eigenvalues. In this case, standard linear algebra packages like LAPACK [171] and ScaLAPACK [194] can be used for matrix diagonalization.

Now, we discuss the application of the proposed technique for studying the bipartite entanglement in fractional quantum Hall states. These topological phases can be experimentally realized in optical lattices with synthetic gauge fields, and are described in more detail in Chapter 4. Here, we study the entanglement characteristics in these phases to demonstrate the application of the bipartition scheme developed in previous sections.

3.4.2 Fractional quantum Hall effect in optical lattice

The topological entanglement entropy, γ, serves as a suitable property for discerning quantum Hall states from other non-topological states. As an application of the methodology we have devised, we examine the fractional quantum Hall state on a square lattice. FQH states can be realized in optical lattices with the introduction of synthetic magnetic fields [25, 26, 195]. Consequently, the hopping term in the tight-binding model such as the Bose-Hubbard model acquires a lattice-site-dependent Peierls phase [57], and the Hamiltonian of the system is given by the bosonic Harper-

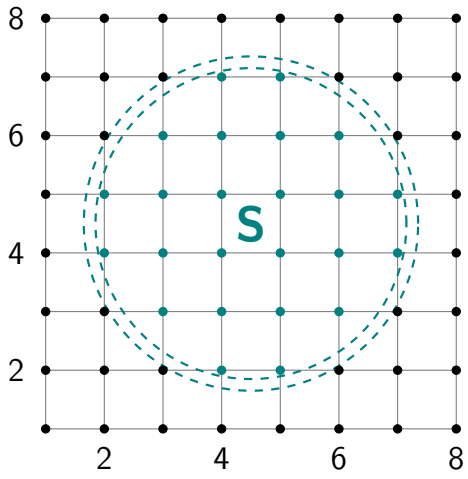

Figure 3.5: Schematic illustration for spatial bi-partitioning of the lattice into a isolated subsystem S, with lattice sites within the circle (teal colored) forming a part of the sub-system S.

Hofstadter Hamiltonian [58, 196, 197]

$$\hat{H} = \sum_{p,q} \left[\left(-Je^{i\phi^x_{p,q}} \hat{b}^\dagger_{p+1,q} \hat{b}_{p,q} - Je^{i\phi^y_{p,q}} \hat{b}^\dagger_{p,q+1} \hat{b}_{p,q} + \text{H.c.} \right) + \frac{U}{2} \hat{n}_{p,q}(\hat{n}_{p,q} - 1) \right] \quad (3.35)$$

Here, $\phi^x_{p,q}, \phi^y_{p,q}$ are the complex phases acquired while hopping in the presence of a magnetic field. Appendix B gives the derivation of the Harper-Hofstadter Hamiltonian. The complex phases are dependent on the strength of the magnetic field, with the magnetic flux per unit cell given by $\alpha = (\phi^x_{p,q} + \phi^y_{p+1,q} - \phi^x_{p,q+1} - \phi^y_{p,q})/2\pi$. These complex phases can be engineered in experiments with the artificial gauge fields, and is discussed in more details in Section 4.1.

We choose Landau gauge, where $\phi^x_{p,q} = 2\pi\alpha\, q$ and $\phi^y_{p,q} = 0$, with the magnetic field strength $\alpha = 1/8$ for a 8×8 lattice with periodic boundary conditions along both the spatial directions. With ED, we obtain the ground state with 4 hardcore bosons, which corresponds to the occupation density $\rho = 1/16$ and a filling factor $\nu = \rho/\alpha = 1/2$. The filling factor measures the ratio of number of particles to the number of magnetic flux quanta in the system. We find that the ground state of the system is $\nu = 1/2$ FQH state and observe that the ground state manifold is two-fold degenerate, a key characteristic property of the $\nu = 1/2$ FQH state on a torus geometry

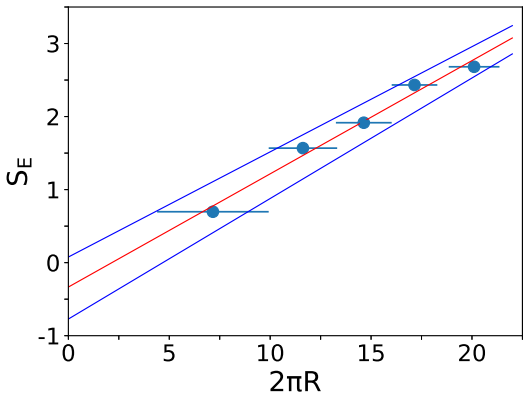

Figure 3.6: Scaling of the entanglement entropy (S_E) of the sub-system S as a function of the boundary length $2\pi R$ of the circular boundary separating the isolated subsystem S from the rest of the lattice. The x-error bars represent the ambiguity in the definition of boundary length.

[198]. We have successfully verified the topological nature of this state by calculating the many-body Chern number employing the prescription of Hatsugai [199]. For extracting the topological entanglement entropy for this state, we bi-partition the lattice system as shown by the schematic in Fig. 3.5. Subsequently, we calculate the entanglement entropy between the subsystem S and the rest of the lattice. However, due to the discrete nature of the lattice geometry, bi-partitioning with a circular geometry introduces ambiguity in defining the boundary, as illustrated in Fig. 3.5. Thus, for a given configuration of lattice sites within the subsystem S, we consider the boundary of the circle enclosing encompassing S to lie within the minimum and maximum radii $(R_{\rm min}, R_{\rm max})$. The scaling of the entanglement entropy, S_E with the boundary length L, as depicted in Fig. 3.6, is bounded by two lines. The lower and upper lines correspond to the least square fits of data for circles with radii $R_{\rm min}$ and $R_{\rm max}$, respectively. In the figure, the middle line represents the least square fit utilizing the average of the two radii. We note that the y-intercept, which represents γ, is dependent on the chosen definition of the boundary length and exhibits a range of variation from 0.08 to -0.77. However, considering the average radius $(R_{\rm min} + R_{\rm max})/2$, we obtain $\gamma = 0.33 \pm 0.17$ which is consistent with the theoretical estimate of $\gamma = ln\sqrt{2} \approx 0.347$ for the $\nu = 1/2$ abelian FQH state. It is worth noting that the numerical estimates can be further refined by incorporating entropy calculations with larger values of L, necessitating larger

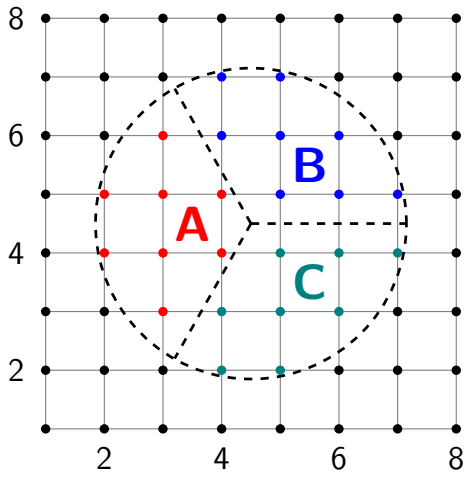

Figure 3.7: Schematic representation showing spatial bi-partitioning of the subsystem in three slices, forming the plural areas A, B and C. The lattice sites in each subsystem are color-coded corresponding to the color of the sub-system label.

lattice dimensions. However, the ambiguity in the definition of L would still persist and can be neglected only for very large lattices.

By adopting the Kitaev and Preskill's approach for computing γ in terms of the plural areas, it becomes feasible to calculate γ without the inherent ambiguity associated with the boundary length. In their approach, γ is expressed by a suitable combination of the entanglement entropies of the plural areas within the subsystem S, as illustrated in Fig. 3.7. It is calculated according to the relation $S_{ABC} - S_{AB} - S_{BC} - S_{AC} + S_A + S_B + S_C = -\gamma$ [191]. Employing this formulation, we have calculated γ for various choices of size for the sub-system S and the results are presented in Fig. 3.8. We note that the numerical estimates of the γ differs from the theoretical estimate of -0.35. Nevertheless, we observe an improvement in the calculated γ as the size of the sub-system S increases. We also note that the trend appears to be saturating towards a finite value for $R_{\mathbf{min}} > 3$, suggesting it may not increase indefinitely with increase in subsystem size. This improvement can be attributed to the necessity of having a smooth, large-sized boundary compared to the correlation length $\xi \ll R$. The calculations with larger subsystem size are however bounded by the constraint $R_{\mathbf{min}} < 3.5$ on a 8×8 lattice. Although, further improvements in the estimates of γ can be achieved

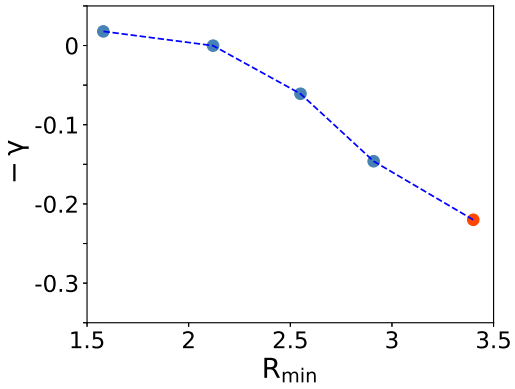

Figure 3.8: Topological entanglement entropy $(-\gamma)$ for $\nu = 1/2$ FQH state. The x axis represents the radius R_{min} for various choices of the circular subsystem S. The filled blue circles corresponds to the subsystem S, centered at the center of the 8×8 lattice system, while the filled red circles corresponds to the subsystem S centered at grid point $(3.85, 3.85)$ of the lattice. The blue dashed-line is a visual guide to the eye.

with a larger-sized subsystem on a larger lattice, the computational resources required for such an endeavour exceed the accessible computational capacity.

3.5 Summary of the Chapter

In this chapter, we have introduced a novel method for exact diagonalization, which relies on a hierarchical approach for defining the basis states for lattice systems. The starting point is the single-site Fock states, which are utilized to construct the row-states, through their tensor products. Subsequently, the tensor product of the row-states generates the multi-row states. This approach offers a high degree of flexibility and is particularly well-suited for studying bosonic optical lattice systems. In such systems, there are no restrictions on the lattice site occupancy, and the number of basis states grows exponentially fast with the system size and number of particles. This multi-step and hierarchical approach allows us to impose various constraints, effectively reducing the dimension of basis set and the Hamiltonian matrix. Furthermore, the construction of the Hamiltonian matrix is optimized with the identification of the pairs of states that contributes to a non-zero matrix element. For the case of state reduction, we employ the bisection method to expedite the identification and calculation of the non-zero

Hamiltonian matrix elements. Each of the constituent steps in our implementation is parallelizable. We have parallelized both the generation of basis set and the calculation of the Hamiltonian matrix elements. Additionally, we parallelize the diagonalization of the Hamiltonian matrix using PARPACK [200]. Using the proposed method, we show how to spatially partition a lattice system, compute the reduced density matrix and calculate the topological entanglement entropy. Specifically, we have applied this methodology to investigate the $\nu = 1/2$ FQH state in the bosonic Harper-Hofstadter Hamiltonian.

Chapter 4

Fractional quantum Hall effect in optical lattice

The phenomena of quantum Hall effect is observed at low temperatures in 2D electron gas subjected to a strong magnetic field in the perpendicular direction. Then, the off-diagonal resistivity forms plateaus as a function of magnetic field, and at these plateaus, the resistivity is quantized $R_{xy} = (2\pi\hbar/e^2)/\nu$. For fractional values of the filling factor ν, defined as the ratio of the number of electrons to the number of available states, this phenomena is called the fractional quantum Hall effect. The FQH states are long-range entangled and topologically protected phases with robust quantized edge transport. Their excitations obey anyonic statistics with fractional charges. Various such fascinating properties exhibited by these phases have attracted attention to these phases and their experimental realization for applications in quantum technologies. Ultracold atoms in optical lattices are excellent systems for investigating the FQH effect due to the possibility of simulating very high magnetic flux per unit cell of the lattice. In addition, the strongly interacting regime is accessible and it helps in stabilizing the ground state quantum phases. In the lattice models, the FQH states are also referred to as the fractional Chern insulators and conceptually originate from the flat Chern bands which play the role of the Landau levels in the continuum [201, 202].

In chapter 3, we discussed the bipartite entanglement entropy for the $\nu = 1/2$ FQH state for a fixed number of bosons with exact diagonalization. The experimental realization of the FQH phase depends upon the outcome of the competition, for existence

as the ground state of the system among different phases supported by the system. In this regard, this chapter investigates the bosonic FQH states in the system of ultracold bosons in optical lattice. These systems, described by the BHM, support the Mott-insulator and SF phases as ground state phases. However, with the implementation of artificial gauge fields, experimentally realized using lasers [26, 195, 203–205], the topological FQH phase can emerge as the ground state of the system at appropriate values of the system parameters. In this chapter, we shall focus on the $\nu = 1/2$ FQH state, and explore the occurrence of this topological phase as the ground state against the competing phases using the CGMF method. The CGMF method is used to study the ground state properties of the system in various parameter regimes and identify the parameter regimes where the quantum Hall states can exist. But, the wavefunction obtained from the CGMF method is not exact because of the mean-field coupling. Thus, for topological characterization of the system, we use exact diagonalization, and the exact wavefunction is used for calculating the many-body Chern number and other topological properties. With CGMF, we obtain the compressibility plot and consider the location of the plateaus in the plot as potential candidates for the FQH state. The characterization of the FQH state is done using ED by studying the properties which are characteristic of quantum Hall states. For instance, the two-point correlation function is calculated to investigate the signatures of the gapped bulk and gapless edges. The topological order of the state is identified by calculating the many-body Chern number. Furthermore, we study the robustness of the FQH state against the dipolar interactions. The repulsive long-range dipolar interactions increase the energy gap between the ground and the excited state. This increases the robustness of the ground state by stabilizing it against perturbations. However, its effect on the long-range entanglements and the topological order in the FQH state should be investigated. This study adds to the literature on FQH states by investigating the effect of dipolar interactions on the stability of FQH states as the ground state quantum phases in optical lattice. We begin the chapter by describing the system and the model Hamiltonian.

4.1 Artificial gauge fields

Consider a system of ultracold neutral bosons trapped in a 2D square optical lattice described by the BHM. To simulate the effects of magnetic field on the charge neutral atoms and to study the topological FQH phases, artificial gauge field is implemented. Experimentally, the gauge fields can be synthesized using the technique of laser-assisted tunneling [70]. It involves creating a staggered superlattice potential along one of the spatial direction (x) with an energy offset Δ, while along the other direction (y) there is no energy offset, and the lattice is simple. This is schematically shown in Fig. 4.1 with grey colored sites corresponding to high-energy sites, while the black-colored sites are lower energy sites. For the energy offset much larger than the hopping strength along the x ($\Delta >> J$), the dynamics along the x is frozen. By creating a running-wave potential using another set of lasers $(\omega_1, \mathbf{k_1})$ along x and $(\omega_2, \mathbf{k_2})$ along y, the resonant tunnelling along x is restored for $\hbar(\omega_1 - \omega_2) = \Delta$. The running-wave beams with wavevectors $|\mathbf{k_1}| \approx |\mathbf{k_2}| \approx k_R$ imparts the hopping term with a lattice-site dependent phase $\delta\mathbf{k}.\mathbf{R} = k_R a(p-q)$. This complex phase, referred to as the Peierls phase, can be tuned by appropriately choosing the lattice geometry and the wavevector k_R. The modified Hamiltonian with complex hoppings is given by the bosonic Harper-Hofstadter model.

4.1.1 Harper-Hofstadter model

In the presence of an artificial gauge field, the ultracold atoms trapped in optical lattices are described by the bosonic analogue of Harper-Hofstadter Hamiltonian [58, 196]. The Hamiltonian is similar to the BHM Hamiltonian except that the hopping term now acquires a lattice-site dependent complex Peierls phase [57, 58]. In the Landau gauge $\mathbf{A} = 2\pi\alpha y\ \hat{x}$ with corresponding magnetic field in the $-z$ direction, the Hamiltonian of the system is given by

$$\begin{aligned} \hat{H} &= -\sum_{p,q}\left(Je^{2i\pi\alpha q}\hat{b}^{\dagger}_{p+1,q}\hat{b}_{p,q} + J\hat{b}^{\dagger}_{p,q+1}\hat{b}_{p,q} + \text{H.c.}\right) \\ &\quad + \sum_{p,q}\left[\frac{U}{2}(\hat{n}_{p,q}\hat{n}_{p,q} - 1) - \mu\hat{n}_{p,q}\right]. \end{aligned} \tag{4.1}$$

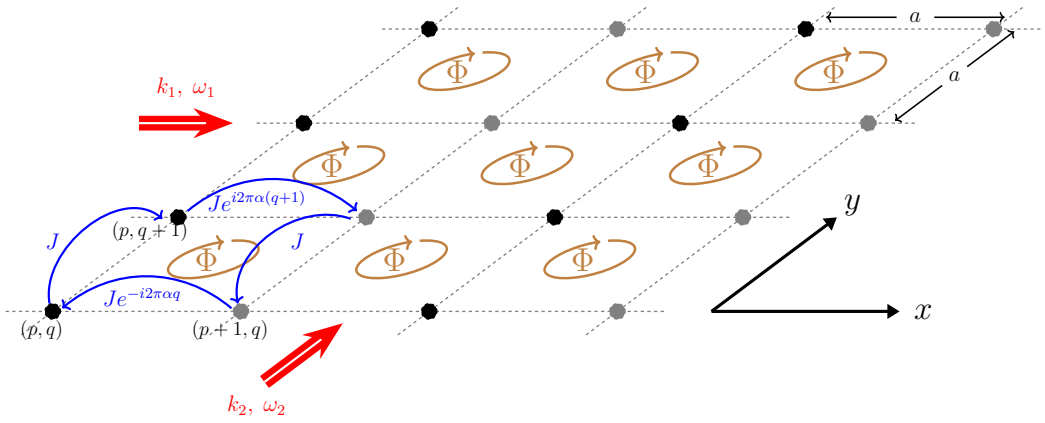

Figure 4.1: Schematic illustration of the complex hopping terms in the Harper-Hofstadter model. The artificial gauge field is implemented by creating a superlattice potential along x with an energy offset among black and grey colored sites. The resonant tunnelling along x is achieved with additional lasers depicted with red color. In the Landau gauge, the hopping along x direction occurs with a lattice-site dependent phase factor, while the hopping along y direction occurs with no additional phase. The total phase accumulated while traversing the unit cell of the lattice is $\Phi = 2\pi\alpha$ and is uniform throughout the lattice.

Here, p (q) is the lattice site index along the $x(y)$ direction, J is the NN hopping strength, U is the onsite interaction strength, μ is the chemical potential, and α represents the total number of flux quanta per unit cell of the lattice. The artificial gauge field results in a phase accumulation of $\Phi = 2\pi\alpha$ while traversing around a unit cell of the lattice, as shown in Fig. 4.1. This simulates the Aharonov-Bohm phase accumulated while traversing a closed loop in a perpendicular homogeneous magnetic field. The artificial gauge field breaks the translational invariance of the lattice in terms of displacement by integer multiples of the lattice vectors. Instead, the Hamiltonian is invariant under translation by the magnetic unit cell. For the choice of Landau gauge considered here and for the artificial gauge field with $\alpha = p/q$, the magnetic unit cell comprises $1 \times q$ lattice sites. In this study, we consider $\alpha = 1/4$, a relatively large value of magnetic field which is experimentally realizable [25]. The magnetic unit cell comprises 1×4 lattice sites and total flux enclosed within the magnetic unit cell is 2π.

The FQH effect in the Harper-Hofstadter model has been extensively studied in

various theoretical studies [34, 59, 73–75]. On the experimental aspects, very recently the FQH state has been observed for the first time with ultracold ^{87}Rb atoms in optical lattices [27]. In the experiment, the $\nu = 1/2$ FQH state is prepared from an initial state of 2 particles localized in a 4×4 driven optical lattice. The driven optical lattice with Raman-assisted tunnelling allows the synthesis of gauge field with independent controls over the magnetic flux per unit cell and the tunnelling rates J_x (J_y) along the x (y)-directions. The asymmetry in the tunnelling along the x and y directions has been utilized to follow an adiabatic path connecting the initially localized state in the absence of any tunnelling and the final FQH state at $J_x = J_y$. The observed Hall conductivity $\sigma_H/\sigma_0 = 0.6 \pm 0.2$ agrees well with the expected value of 0.5 for the $\nu = 1/2$ FQH state. Now, we shall discuss the investigation of the topological FQH phases as the ground state quantum phases in the Harper-Hofstadter model with the CGMF method.

4.1.2 Ground state quantum phases

With the CGMF method, we obtain the ground state quantum phases of the system. Similar to BHM, we find the Mott insulator and superfluid phases but with an enhancement in the MI-SF phase boundary. The enhancement can be attributed to the localizing effects arising from the cyclotronic motion arising from the artificial gauge fields. Following previous studies, predicting the formation of bosonic FQH states out of excitations on top of the Mott insulating phase [76, 77], we search for the FQH states in the vicinity of the Mott lobe for various values of the chemical potential. FQH are incompressible states, and correspond to the plateaus in the compressibility curve, which is the plot of average bosonic density ρ as a function of μ/U. To investigate the FQH states, we have chosen $\alpha = 1/4$ and have used 4×4 clusters to tile the 12×12 lattice. This choice of cluster and lattice size is consistent with the magnetic translational symmetry for chosen value of α. To mimic the thermodynamic limit, we use periodic boundary conditions along both the spatial directions. We further consider the bosonic atoms as hardcore bosons, which means the single-site occupancies can be either 0 or 1. The hardcore assumption is justified near the $\rho = 0$ state and at low J/U, since the probability of double occupancies at a site is negligible. With this and a fixed

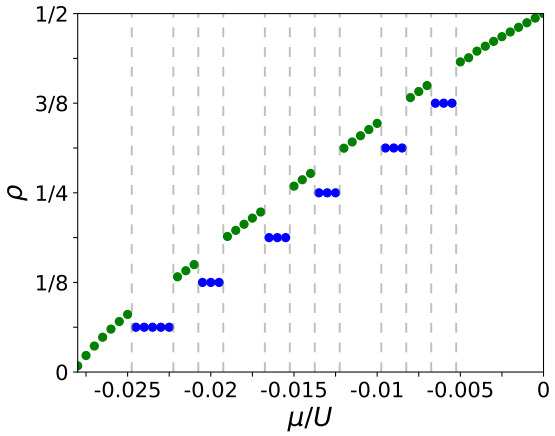

Figure 4.2: Compressibility plot: The ground state density ρ as a function of μ/U for hardcore bosons at $J = 0.01$ and $\alpha = 1/4$. The density of the incompressible ground states are identified with green colored dots while that of superfluid ground states are identified with blue colored dots. The dashed gray line separates the incompressible states and the superfluid state regimes.

$J = 0.01U$, we obtain the ground state of the system at different values of chemical potential.

The average bosonic density as a function of the chemical potential is shown in Fig. 4.2. As shown in the compressibility plot, the SF states with continuously varying number density against μ/U are obtained as the ground state in various parameter regimes. These compressible ground states are shown with blue color. However, for some values of μ/U, the number density does not change with variations in μ/U and appears as plateaus in the compressibility curve. The incompressible states appear with the number density $\rho = 1/16, 1/8, 3/16, \cdots$ which corresponds to the filling factors $\nu = \rho/\alpha = 1/4, 1/2, 3/4, \cdots$, respectively. The parameter domain of the incompressible ground states is shown in green color. In these regimes, the incompressible states are the ground states, while the SF states are the competing metastable states. For instance, at $\mu = -0.020U$, the incompressible state with $\rho = 1/8$ is lower in energy and is nearly degenerate in energy with the competing SF state which is metastable. The energy per particle for the incompressible state is $-0.00456U$, while the competing SF state exists as a metastable state, featuring a higher particle density and an energy per particle of $-0.00446U$. The difference in energy per particle between the two states

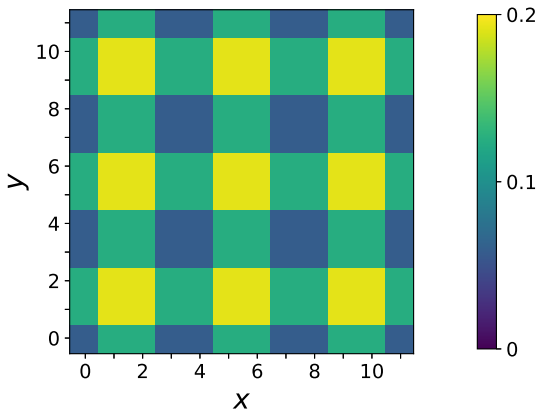

Figure 4.3: Density distribution for $\nu = 1/2$ filling incompressible state at $\mu = -0.020U$, $J = 0.01U$ and $\alpha = 1/4$.

is very small, approximately $0.0001U \sim J/100$. These states corresponding to the plateaus in the compressibility plot are candidates for quantum Hall states and confirmation can be done by studying other properties of the state. To investigate the finite size effects, we have investigated for $\rho = 1/8$ plateau with system sizes of 8×8 and 16×16 for a range of μ/U values around this plateau. We note that this plateau is intact, and robust against the finite size of the lattice.

After studying the average bosonic densities, we investigate the density distribution of $\nu = 1/2$ incompressible states corresponding to the plateau in the compressibility plot. The image in Fig. 4.3 shows the density distribution for such a state at $\mu = -0.020U$ corresponding to $\rho = 1/8$ and $\nu = 1/2$. In this figure, we notice that the bosonic density is maximum at the centre of the 4×4 cluster, and it decreases radially within each of the clusters. The density distribution among the clusters is identical. This is expected as the coupling between different clusters is incorporated through the mean field, which is zero in the incompressible state. Further characterization of the $\nu = 1/2$ incompressible state is discussed in the remaining part of the chapter.

4.2 Characterization of $\nu = 1/2$ FQH state

In the previous section, we used the CGMF method to identify the ground state quantum phases. For characterizing the incompressible states, which correspond to the plateaus in the compressibility curve, we use ED with a fixed number of particles at

the required filling factors. Here, we shall discuss a few properties of the FQH state which can be used to characterize the state.

4.2.1 Two point correlation function

The quantum Hall states are gapped in the bulk and possess gapless edges at the boundary of the system. This characteristic property can be studied using the two-point correlation (TPC) function defined by $\langle \hat{b}^\dagger(x', y')\hat{b}(x, y)\rangle$, where the expectation is calculated with respect to the ground state wavefunction. For the QH states, the TPC function exhibits a power-law decay at the edges, whereas in the bulk, it follows an initial exponential decay and a power-law tail towards the end of the bulk row [80]

$$\langle \hat{b}^\dagger(x, y)\hat{b}(0, y)\rangle \propto \begin{cases} 1/x^\alpha, & y \sim 0, \\ e^{-x/\xi}, & y \sim M/2, x < M, \\ 1/(x + 2y)^\alpha, & y \sim M/2, x \sim M. \end{cases} \tag{4.2}$$

We investigate the decay of TPC function for the $\nu = 1/2$ state for sufficiently large lattice systems. In order to distinguish the edge row from the bulk of the lattice, we use open boundary conditions. This is shown in Fig. 4.4, where we have plotted the TPC for the system of 4, 5 and 6 bosons on 8×4, 10×4, and 12×4 lattices respectively. With the artificial gauge field $\alpha = 1/4$, these choices of bosonic density correspond to the filling factor $\nu = \rho/\alpha = 1/2$.

In Fig. 4.4, the TPC function for the bulk row $y = 1$ is shown with different shades of red color for different lattices. And, for the $y = 0$ row at the edge, TPC function for different lattices is shown with different shades of blue color. From the figure, we can see an initial exponential decay in the bulk row. However, for the $y = 0$ row at the edge, decay is not exponential but more like a power-law decay. Owing to a smaller extent of the system along the $y-$ direction, the power-law decay is not clearly discernible. This can be improved by increasing the lattice dimension along the y direction, then the distinction between the bulk and edge would be more prominent. However, to respect the magnetic unit cell, the lattice should consist of 8 rows, which would require very high computational resources. In view of this, we infer few observations from Fig. 4.4 only. From the figure, in $y = 0$ row at the edge, we observe an initial power law decay followed by a non-monotonic trend and followed by a power law decay. The power

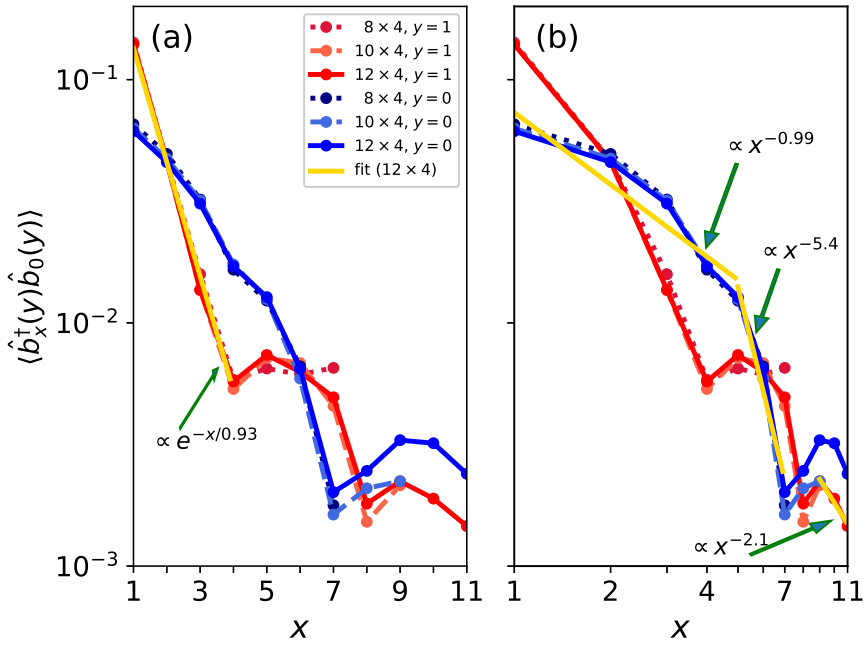

Figure 4.4: Two-point correlation function for $\nu = 1/2$ filling state using open boundary conditions in (a) log-linear scale and (b) log-log scale. Different shades of the red and blue colors correspond to the row in bulk $(y = 1)$ and at the edge $(y = 0)$ respectively. Dotted, dashed, and solid lines correspond to system sizes 8×4, 10×4, and 12×4 respectively. The yellow line shows the fitted curve.

law exponents are -0.99 ± 0.18 for $1 \lesssim x \lesssim 5$ and -5.4 ± 1.1 for $5 \lesssim x \lesssim 7$. While in the bulk row $y = 1$, we find an initial exponential decay, $\langle \hat{b}^\dagger(x', y)\hat{b}(x, y)\rangle \propto e^{-x/\xi}$ with correlation length $\xi = 0.93 \pm 0.04$. This trend persists till $x \lesssim 4$ and is followed by a non-monotonic behaviour. Finally, towards the end of this row, a power law decay with exponent -2.1 ± 0.34 is observed for $9 \lesssim x \lesssim 11$. The non-monotonicity in the middle of the bulk and edge rows is evident for the larger lattices. However, near the end of the two rows, it is a decaying function. These trends of the TPC function for the rows in bulk and the edge are consistent with a QH state.

4.2.2 Ground state degeneracy on torus geometry

Apart from the characteristic trend in the TPC function, the FQH states also possess characteristic degeneracy. On a torus geometry, with the implementation of periodic boundary conditions along the two spatial dimensions of the 2D lattice, the ground

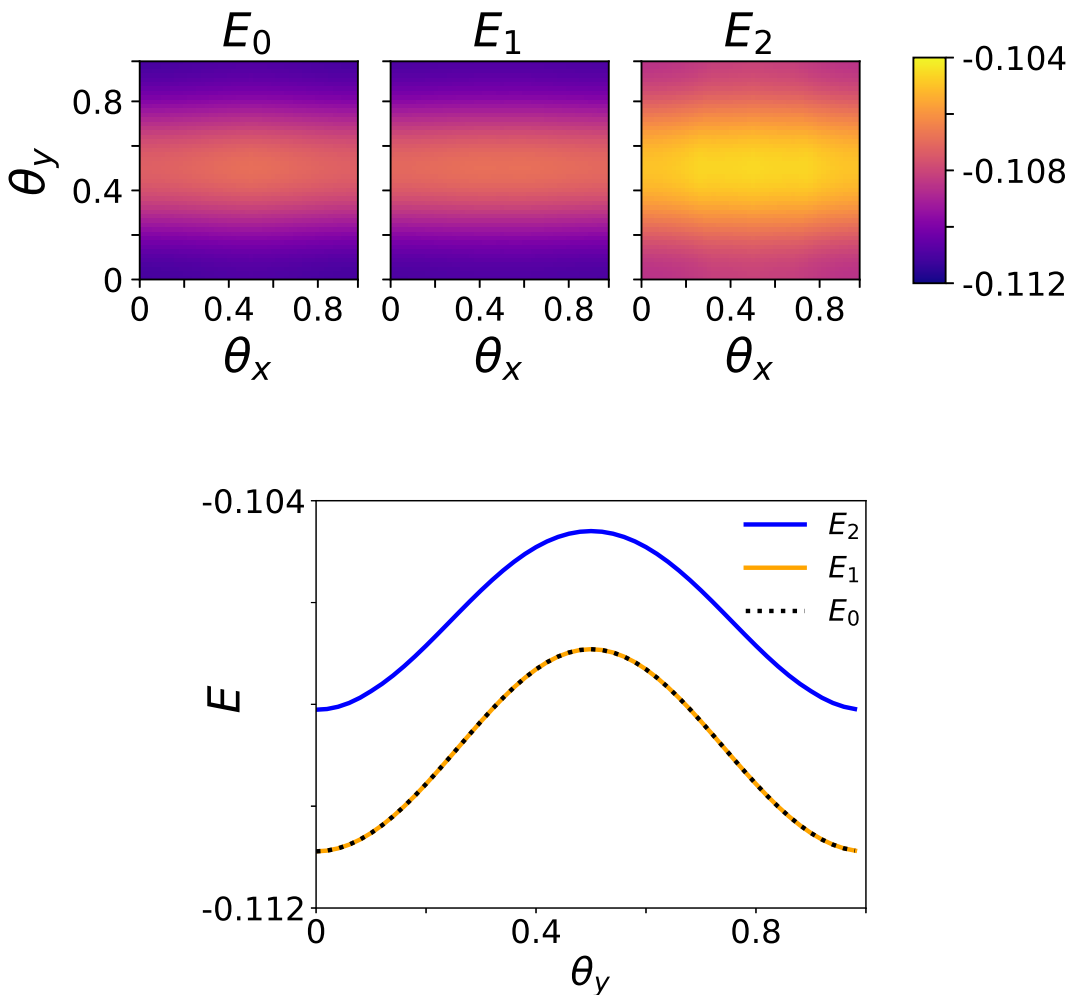

Figure 4.5: For $\nu = 1/2$ filling state with 4 bosons on a 8×4 lattice with PBC at $J = 0.01U$, energies of degenerate ground states E_0, E_1 and of first excited state E_2. Top figure shows the variation of energies with the twist angles (θ_x, θ_y), and the bottom figure shows energies as a function θ_y for fixed $\theta_x = 0.5$.

state manifold corresponding to the $\nu = 1/2$ FQH state is doubly degenerate. More specifically, on a Riemann surface of genus g, the ground-state manifold of the $\nu = p/q$ FQH state with p and q as co-primes is q^g fold degenerate [198]. The torus geometry corresponds to $g = 1$. In addition, on a torus geometry, translation of the wavefunction by the lattice size along any of the two spatial dimensions yields the original wavefunction upto a phase factor. The generalized boundary conditions thus correspond to the twist angles at the boundary. The twist angles represent the magnetic flux along the axis or through the centre of the torus [74]. With the introduction of the twist angles at

the boundary, the Hamiltonian is

$$\begin{aligned}\hat{H} &= \sum_{p,q}\Big[-\Big(Je^{i2\pi\alpha q}e^{-i2\pi\delta_{xL}\theta_x}\hat{b}_{p+1,q}\hat{b}_{p,q} + Je^{-i2\pi\delta_{yL}\theta_y}\hat{b}_{p,q+1}\hat{b}_{p,q} + \text{H.c.}\Big) \\ &\quad + \frac{U}{2}\hat{n}_{p,q}(\hat{n}_{p,q}-1) - \mu\hat{n}_{p,q}\Big], \end{aligned} \tag{4.3}$$

where, δ_{xL} is the Kronecker delta function and θ_x (θ_y) is the twist angle at the boundary of the lattice along x (y) direction. The ground state manifold is thus a function of the twist angles. For the $\nu = 1/2$ filling, corresponding to 4 bosons on a 8×4 lattice with PBC, we investigate the energy spectrum at $J = 0.01U$ with exact diagonalization for a few low-lying states on a grid of twist angles (θ_x, θ_y). We find a slight variation in the ground-state energy with the twist angles, however, the two-fold degeneracy persists throughout the range of twist angles $0 \leqslant \theta_x, \theta_y \leqslant 1$. The ground-state energy of the doubly degenerate manifold and energy of the first excited state is shown in Fig. 4.5, where we can see that the energy gap is $\approx J/4$. The double degeneracy of the ground state manifold is also observed for a system of 2 bosons on a 4×4 lattice with PBC. Thus, the double degeneracy of the $\nu = 1/2$ state satisfies another important property for its characterization as the FQH state.

4.2.3 Many body Chern number

FQH states are topological phases, and in order to characterize the topological order of the state, we calculate the many body Chern number (MBCN) utilizing the method outlined in [199]. For the FQH state with filling factor $\nu = 1/2$, the ground state manifold is doubly degenerate on a torus geometry. Thus, the ground state manifold projector at twist angles (θ_x, θ_y) is given by

$$P(\theta_x, \theta_y) = |\Psi_0(\theta_x, \theta_y)\rangle \langle\Psi_0(\theta_x, \theta_y)| + |\Psi_1(\theta_x, \theta_y)\rangle \langle\Psi_1(\theta_x, \theta_y)|. \tag{4.4}$$

Here, $\Psi_0(\theta_x, \theta_y)$ and $\Psi_1(\theta_x, \theta_y)$, are the two orthogonal states from the degenerate ground state manifold at twists (θ_x, θ_y) for the Hamiltonian defined in Eq. (4.3). In order to fix the gauge for the ground state manifold, we choose two reference multiplets from the ground state manifold at two distinct values of the twist angles. These reference states are denoted as $\Phi_j(\theta_x^1, \theta_y^1)$ and $\Phi'_k(\theta_x^2, \theta_y^2)$, where the indices j and k take values 1 or 2 for the two degenerate states. This allows the definition of two distinct

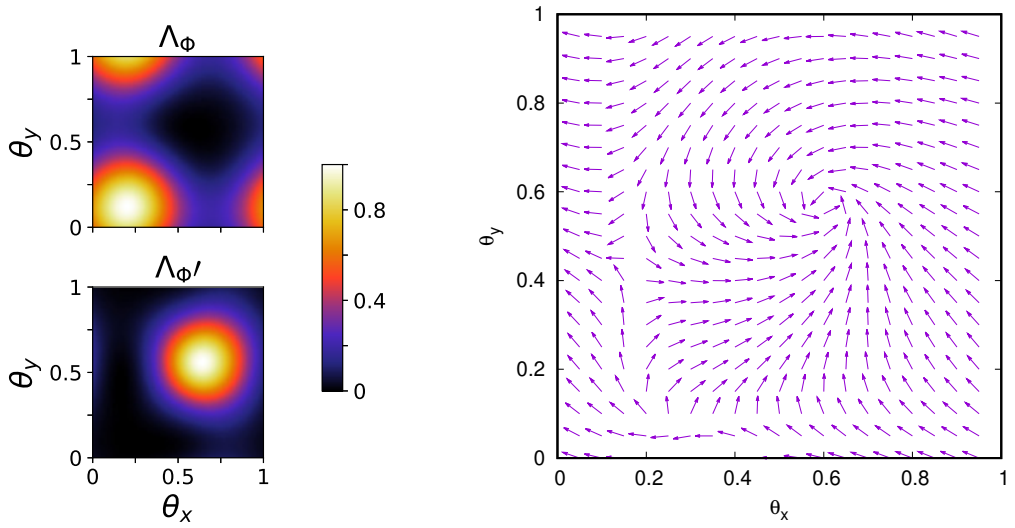

Figure 4.6: (Left) Gauge fields Λ_Φ and $\Lambda_{\Phi'}$ in the (θ_x, θ_y) plane. The gauge fields are well defined in complementary regions of the plane. (Right) Argument field Ω in the (θ_x, θ_y) plane. In the region, with $\Lambda_\Phi = 0$ and $\Lambda_{\Phi'} \neq 0$, we see a vortex in the Ω field with phase accumulation of 2π around it and unit vorticity. Similarly, in the complementary region, we find a unit vorticity, which signifies the MBCN = 1.

gauge references with corresponding scalar fields $\Lambda_\Phi = \det\langle\Phi_j|P(\theta_x,\theta_y)|\Phi_k\rangle$ and $\Lambda_{\Phi'} = \det\langle\Phi'_j|P(\theta_x,\theta_y)|\Phi'_k\rangle$. It is important to note that the gauge fields associated with Φ and Φ' are not well defined across the entire grid spanned by $0 \leqslant \theta_x, \theta_y \leqslant 1$. The region where one of the gauge reference is not well-defined, the other gauge reference can be used. The MBCN is then given by the number of branch vortices in the argument field Ω, defined by

$$\Omega = \arg\Big(\det\langle\Phi'_j|P(\theta_x,\theta_y)|\Phi_k\rangle\Big), \tag{4.5}$$

in either of the regions where one of the reference field Λ_Φ or $\Lambda_{\Phi'}$ vanish. The counting of the number of branch vortices is done by summing the vortices and anti-vortices with appropriate signs according to their vorticity [74, 81].

To identify the topological order in the $\nu = 1/2$ filled state, we calculate the MBCN of this state. For the system of 4 bosons on a 8×4 lattice with PBC and $\alpha = 1/4$, we calculate the argument field Ω and obtain MBCN equal to 1. The image and plot in Fig. 4.6 show gauge references and the argument field as a function of the twist angles. We observe that Ω has a vortex in the region where Λ_Φ vanishes. Thus, we get a unit vorticity amounting to the MBCN equal to 1. We have also calculated the

MBCN for the $\nu = 1/2$ filling on 4×4 lattice and found it to be 1. Thus, the state with $\nu = 1/2$ filling is topologically ordered and is identified as the FQH state. Combined with the CGMF results, we can conclude that $\nu = 1/2$ FQH can occur as the ground state against the competing SF state in optical lattices. Next, we investigate the effect of dipolar interactions on the robustness of this state.

4.3 FQH with dipolar interactions

In this section, we shall discuss the effect of dipolar interactions on the stability of the FQH states in optical lattice. As mentioned earlier, the quantum Hall states are separated from the excited states by an energy gap, and a larger gap ensures the robustness of the state against perturbations. In Ref. [74], using ED for a system with a fixed number of particles, it was shown that the energy gap increases with the dipolar interactions, and it preserve the topological order of the state. Further, in Ref. [206], it was shown that with the introduction of a long-range interaction to the rapidly rotating bosons, the $\nu = 3/2$ FQH state emerges as the ground state of the system. Here, using the CGMF method, where the particle number depends upon the chemical potential, we first investigate if the FQH states occur as the ground state quantum phases of the system with dipolar interactions. Here, the ground state could be either of the competing states, the compressible superfluid or the incompressible state. In case the incompressible emerges as the ground state, we use ED to characterize it and check if it is the FQH state. With the dipolar interactions of strength V, and truncated to nearest-neighbor, the Hamiltonian in Eq. (4.1) is modified with an additional interaction term corresponding to the NN interactions

$$\begin{aligned}\hat{H} &= -\sum_{p,q}\left(Je^{2i\pi\alpha q}\hat{b}^{\dagger}_{p+1,q}\hat{b}_{p,q} + \hat{b}^{\dagger}_{p,q+1}\hat{b}_{p,q} + \text{H.c.}\right) \\ &\quad + \sum_{p,q}\left[\frac{U}{2}(\hat{n}_{p,q}\hat{n}_{p,q} - 1) - \mu\hat{n}_{p,q} + V\,\hat{n}_{p,q}\left(\hat{n}_{p+1,q} + \hat{n}_{p,q+1}\right)\right]. \qquad (4.6)\end{aligned}$$

With the CGMF method, using 4×4 clusters on a 12×12 lattice, we obtain the compressibility plot for hardcore dipolar bosons with NN strengths $V = 2J$ and $V = 5J$ at $J = 0.01U$ and $\alpha = 1/4$. For $V = 2J$, as shown in Fig. 4.7 (a), we find plateaus corresponding to incompressible states at densities $\rho = 1/16$, $1/8$, and $3/16$ in the

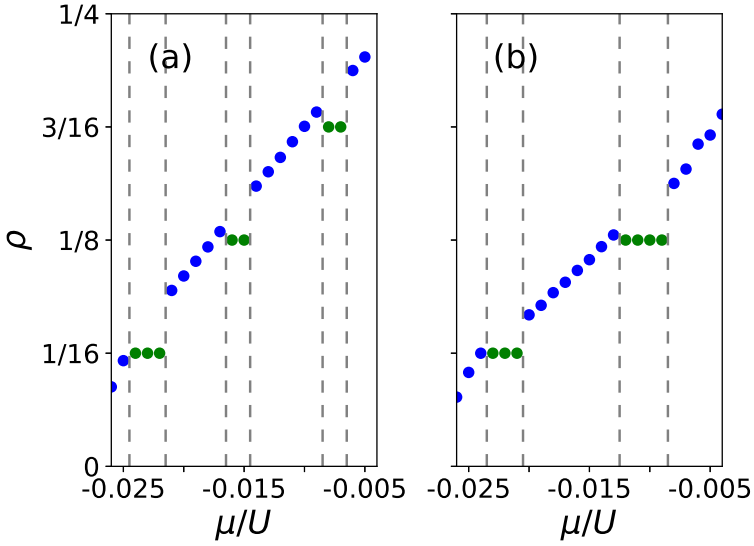

Figure 4.7: Compressibility plot: The ground state density ρ as a function of μ for hardcore bosons at $J = 0.01U$ and $\alpha = 1/4$ for NN interaction strengths (a) $V = 2J$ and (b) $V = 5J$. The incompressible ground states are identified with green colored dots, while the superfluid ground states are identified with blue colored dots. The dashed gray line separates the incompressible states and the superfluid state regimes.

specified range of μ/U. It can be seen that with NN interaction, the plateaus have shifted to higher μ/U values compared to the case when $V = 0$. This is due to the repulsive nature of dipolar interactions, which favor a state with lower density at a given value of μ/U, in order to reduce the repulsive interaction energy. The incompressible state with $\rho = 1/8$ corresponds to the filling factor $\nu = \rho/\alpha = 1/2$ and may correspond to the $\nu = 1/2$ FQH state. This incompressible state at $\mu/U = -0.015$, has energy per particle $-0.0084U$, while the competing SF state at this value of chemical potential has energy per particle $-0.0079U$. The energy gap between the two states is $0.0005U \sim J/20$.

For $V = 5J$, as shown in Fig. 4.7 (b), we observe the plateaus in the compressibility plot at density $\rho = 1/16$ and $1/8$ in the specified range of chemical potential. The incompressible plateaus have shifted to higher μ/U values compared to lower values of V. At $\mu = 0.01U$, $\rho = 1/8$ incompressible state with filling $\nu = 1/2$ have energy per particle $-0.0121U$, while the competing SF state with higher density has energy per particle $-0.0111U$. Thus, the energy gap separating the incompressible ground state

from the SF state is $0.001U \sim J/10$. Additionally, it is noted that the plateaus in the compressibility plot now extend across a broader parameter range within the ground state phase diagram. Hence, the repulsive dipolar interactions serve to enhance the energy gap between the incompressible ground state and the compressible metastable states. These observations strongly imply that the dipolar interactions play a stabilizing role for the incompressible state against the competing compressible SF phase. Although in this study, we have truncated the dipolar interactions to nearest neighbors, this qualitatively captures the effects of long-range interactions. With the inclusion of the next-nearest neighbor interactions, we have examined the effect on $\rho = 1/8$ plateau and found it to be robust.

4.3.1 Characterization of $\nu = 1/2$ state

As mentioned earlier, the characterization of the $\rho = 1/8$ incompressible state at $\nu = 1/2$ filling as the FQH state is done by studying the decay in two-point correlation function, the ground state degeneracy on a torus geometry and the many-body Chern number. We shall examine these properties for the $\rho = 1/8$ incompressible state at $V = 2J$ at $J = 0.01U$ and $\alpha = 1/4$.

We first discuss about the TPC function obtained with the ED method on a square lattice with open boundary conditions. For $\rho = 1/8$ state on 8×4 and 10×4 lattices, the TPC function is shown in Fig. 4.8. We find that in the bulk row $y = 0$, it decays exponentially $\langle \hat{b}^\dagger(x', y')\hat{b}(x, y)\rangle \propto e^{-x/\xi}$ for $x \lesssim 3$ with correlation length $\xi = 0.83 \pm 0.02$. Afterwards, it shows a non-monotonic trend. While in the row $y = 0$, which lies at the edge, the TPC has a power law decay with exponent -1.2 ± 0.3 for $1 \lesssim x \lesssim 5$. This trend of the TPC function is consistent with that of a quantum Hall state. It should be noted that ξ in the bulk is now smaller than the case with $V = 0$. Thus, the dipolar interactions can affect the long-range entanglements in the FQH state, and it is interesting to see whether it affects the topological order in the state. We have investigated the ground-state degeneracy on a torus geometry and found that the ground state manifold is doubly degenerate, which is consistent with the $\nu = 1/2$ FQH state. The topological order of the $\nu = 1/2$ state is investigated by calculating the MBCN on a 4×4 and 8×4 lattice. We find that the MBCN is equal to 1, which confirms the

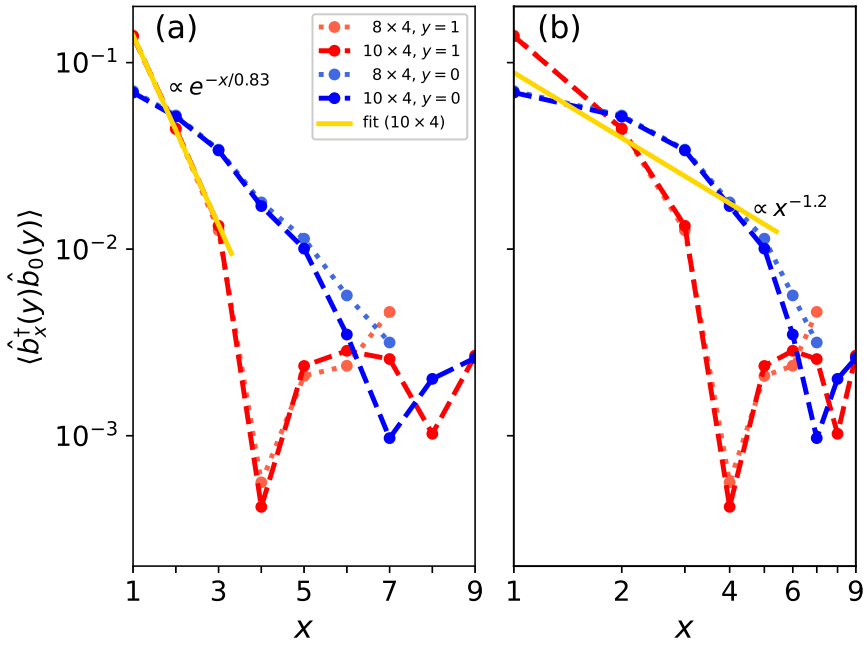

Figure 4.8: Two-point correlation function for $\nu = 1/2$ filling state at $V = 2J$ in (a) log-linear scale, and (b) log-log scale. Different shades of the red and blue colors correspond to the row in bulk $(y = 1)$ and at the edge $(y = 0)$ respectively. The yellow line shows the fitted curve.

topological order. For $V = 2J$ and for $\nu = 1/2$ state on a 4×4 lattice, the argument field is shown in Fig. 4.9, where a single branch-vortex in either of the complementary regions signifies the MBCN equal to 1. We have also verified the topological nature of $\nu = 1/2$ state at $V = 5J$ and identify it as FQH state by calculating the MBCN. We thus find that the BHM with dipolar atoms supports the FQH states as ground states and is more robust. With the recent experimental realization of $\nu = 1/2$ FQH states for the ultracold gas of $^{87}\mathrm{Rb}$ atoms in optical lattice [27], our study suggests the possibility of observing this state with dipolar condensates in optical lattices in near future.

In our study, we have focused the investigations exclusively on closed systems. Nevertheless, in the pursuit of realizing topologically ordered phases in the experiments, it is important to consider the impact of dissipations arising from interactions with the surrounding environment. The dissipations via two-body loss, explored within the framework of Markovian dynamics, have been studied in [207, 208]. The findings indicates the preservation of the topological order, however, the state has a finite

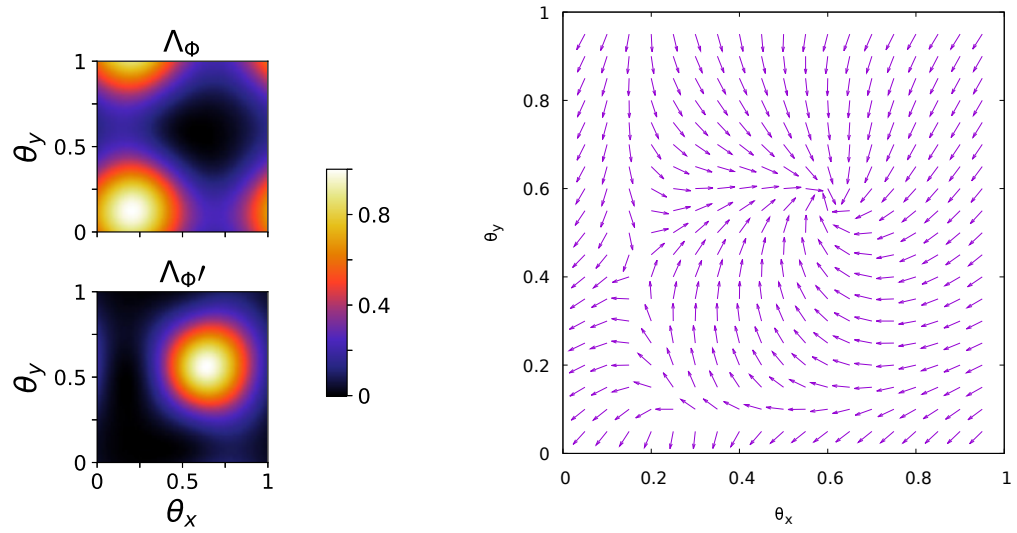

Figure 4.9: (Left) Gauge fields Λ_Φ and $\Lambda_{\Phi'}$ in the (θ_x, θ_y) plane. The gauge fields are well defined in complementary regions of the plane. (Right) Argument field Ω in the (θ_x, θ_y) plane. In the region, with $\Lambda_\Phi = 0$ and $\Lambda_{\Phi'} \neq 0$, we see a vortex in the Ω field with phase accumulation of 2π around it and unit vorticity. Similarly, in the complementary region, we find a unit vorticity, which signifies the MBCN = 1.

lifetime. In a related work ref. [209] discusses the state preparation of FQH states through dissipative pumping of particles from higher to lower bands. The effect of non-Markovian environments has been studied in the context of atom-cavity systems and has been discussed in [210–213]. However, the effect on topologically ordered phases needs further exploration.

4.4 Summary of the Chapter

In this chapter, we have explored the FQH states in the bosonic Harper-Hofstadter Hamiltonian. This specific Hamiltonian can be effectively realized in the experimental setups with ultracold atoms confined in optical lattices. We find the incompressible states with filling factors similar to the FQH states as the ground state of the system for various parameter regimes. The ground state quantum phases are obtained with the CGMF method, suitable for capturing the quantum correlations in the state. To establish these incompressible states as FQH state, we focused on the $\nu = 1/2$ filling state and demonstrated the topological order in the state by calculating the MBCN. For the

case of dipolar atoms, we have introduced the dipolar interactions truncated to NN and have shown that $\nu = 1/2$ FQH state is the ground state of the extended Hamiltonian in certain parameter regimes. We have observed that the dipolar interactions stabilize the FQH state against the competing SF phase. Additionally, we have also verified the robustness of the $\nu = 1/2$ FQH state against finite size effects associated with the finite lattice. Also, we have verified by incorporating the next-nearest neighbor interactions, the $\nu = 1/2$ FQH state is robust against the tail of the dipolar interactions.

Chapter 5

Quench dynamics across the MI-SF phase transition

In previous chapters, we have discussed the bosonic fractional quantum Hall states in optical lattice. We considered these systems as closed systems with a minimal coupling with the surroundings and examined the ground state quantum phases at equilibrium. However, the quantum systems engineered in experiments are subject to various non-equilibrium effects. For example, the dissipation effects in systems coupled to a surrounding or the non-adiabatic effects setup in response to a external control signal. The advancements in quantum technologies revolve around the dynamical manipulation of quantum states, thus necessitating understanding of dynamics associated with quantum state engineering. The dynamical evolution of these systems depends upon the low-lying energy levels accessible to the system and can shed light on to various equilibrium properties, referred to as quench spectroscopy. In regard to the rich physics associated with the out-of-equilibrium dynamics, this chapter discusses the non-equilibrium dynamics of quantum systems under a quantum quench, which refers to a change in the parameters of the underlying Hamiltonian.

Understanding the non-equilibrium aspects is crucial for the development of quantum states in the laboratory. For example, it has significance in the state-preparation procedures, where a desired state is obtained by systematically adjusting parameters, commencing from an initially manageable state. The non-adiabatic effects linked with the quench process can lead to unwanted excitations in the final state. However, such

excitations can be minimized by controlling the quench with an optimal protocol. The quench process can occur as a sudden quench, involving an abrupt change in one of the system parameters, followed by an evolution of the system with new Hamiltonian. The other possibility is slow quench, where the parameter is changed over a finite time duration. Quenches provide a versatile experimental and theoretical framework to probe the rich dynamics and phenomena in quantum systems. The many-body localization, thermalization, and entanglement dynamics following the quench are various research pursuits [85, 214]. This chapter focuses on the slow quenches in the system of ultracold atoms in optical lattice across the Mott-insulator to superfluid quantum phase transition of Bose-Hubbard model.

Ultracold atoms confined in optical lattices provide an exceptional platform to explore the dynamics of quantum many-body systems. The ability to readily control the system parameters and minimal interaction with the surrounding environment make these systems better candidates to study quantum quench dynamics. These systems are described by the BHM and supports the MI and SF quantum phases. A gradual quench from the symmetric MI phase to symmetry-broken SF phase results in the creation of vortices in the quenched SF state. This is attributed to the non-adiabatic or impulse regime during the evolution, which sets in as the system approaches the quantum critical point as described by the Kibble-Zurek mechanism (KZM). The KZM demonstrates the universality in the dynamics across phase transitions and predicts scaling laws for various properties of dynamical state [86, 108]. In this chapter, we shall study the quench dynamics across the MI-SF QPT from the perspective of KZM. We shall obtain the Kibble-Zurek scaling laws using the single-site Gutzwiller mean-field and cluster Gutzwiller mean-field theory. We begin by first discussing the KZM for thermal phase transitions and subsequently derive the KZ scaling laws which are also applicable for QPTs.

5.1 Kibble-Zurek Mechanism

For continuous thermal phase transitions, the relaxation time τ and the correlation length ξ diverge near the critical point of the phase transition. This divergence en-

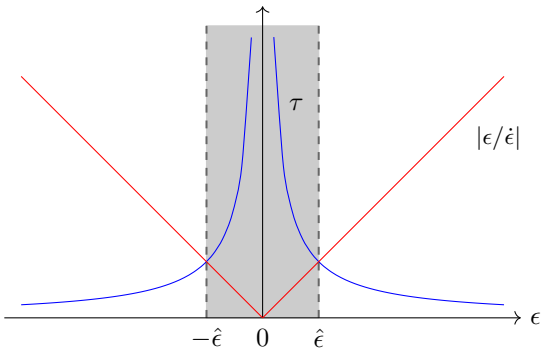

Figure 5.1: Relaxation time (blue) and the inverse transition rate (red) for a linear quench, as a function of the reduced distance from the critical point. The crossover from adiabatic to impulse happens at $-\hat{\epsilon}$ and $\hat{\epsilon}$ when relaxation time equals the inverse transition rate. The impulse region is shown as the shaded region, where relaxation time is greater than inverse transition rate.

capsulates the universality near the critical point, whereby the microscopic details of the system do not matter much and different systems exhibit similar behaviour [215]. In terms of the reduced distance from the critical point $\epsilon = (\chi - \chi_c)/\chi_c$, where χ is the system's parameter governing the phase transition, the correlation length and the relaxation time have power law divergences

$$\xi \propto |\epsilon|^{-\nu}, \text{ and } \tau \propto |\xi|^z = |\epsilon|^{-\nu z}. \tag{5.1}$$

Here, ν and z are the power law exponents and these are referred to as the critical exponents of the phase transition. Under a quench of the system parameter, the adiabaticity during the evolution depends upon the competition between the relaxation time and the inverse transition rate $|\epsilon/\dot{\epsilon}|$, which measures the time from the critical point of the phase transition. Near the critical point, the relaxation time diverges, and the system can not adapt to any changes in the parameter being quenched, resulting in a loss of adiabaticity in the evolution. However, far away from the critical point, the relaxation time is small, $\tau \ll |\epsilon/\dot{\epsilon}|$, leading to an adiabatic evolution. The KZM approximates the dynamical evolution of the quenched state as adiabatic for $\tau < |\epsilon/\dot{\epsilon}|$ and as impulse for $\tau > |\epsilon/\dot{\epsilon}|$. In the impulse domain, the state is assumed to be frozen. The crossover between adiabatic and impulse occurs at $\pm\hat{\epsilon}$, which is obtained from

the relation $\tau(\hat{\epsilon}) = |\hat{\epsilon}/\dot{\hat{\epsilon}}|$. Assuming a linear quench protocol, $\epsilon(t) = t/\tau_Q$, with τ_Q being the quench rate, the impulse regime of KZM is shown in Fig. 5.1. In the impulse regime, in which the quenched state evolves trivially with a phase only, the correlation length at the end of the impulse $\hat{\epsilon}$ is the same as at $-\hat{\epsilon}$. This determines the size of the correlated domains, with different choices of the symmetry breaking, formed after the phase transition. The meeting points of these uncorrelated domains constitute defects in the post-quenched state. The average size of the domains and the defect density vary with the quench rate as a power law with exponents given in terms of the equilibrium critical exponents ν and z. This power law scaling behaviour constitutes the KZ scaling laws and forms the key verifiable predictions of KZM.

5.1.1 Kibble-Zurek scaling laws

Adopting a linear quench protocol of the system parameter χ across the critical point χ_c, we have

$$\chi(t) = \chi_i + (\chi_c - \chi_i)\left(1 + \frac{t}{\tau_Q}\right). \tag{5.2}$$

Here, we assume that the quench starts at $t = -\tau_Q$ with $\chi_i < \chi_c$ in the symmetric phase and is continued till $\chi_f > \chi_c$ in the symmetry broken phase. The critical point χ_c is reached at $t = 0$ and the adiabaticity of the quench is controlled by the quench rate τ_Q. Without loss of generality, let us assume $\chi_i = 0$. With this, the reduced distance is

$$\epsilon(t) = \frac{\chi(t) - \chi_c}{\chi_c} = \frac{t}{\tau_Q}. \tag{5.3}$$

As the critical point is approached, the relaxation time of the system diverges near the phase transition, which results in loss of adiabaticity. The adiabaticity of the quench depends upon the competition between the system relaxation time and the inverse transition rate $|\epsilon/\dot{\epsilon}|$. In Fig. 5.2, these two timescales are shown as a function of the quench parameter χ for two different quench rates. The KZM categorizes the dynamical evolution as adiabatic, away from the critical point for $\tau < |\epsilon/\dot{\epsilon}|$, and as impulse near the critical point for $\tau > |\epsilon/\dot{\epsilon}|$. The crossover between adiabatic and impulse evolution occurs at

$$\left|\frac{\hat{\epsilon}}{\dot{\hat{\epsilon}}}\right| = \tau(\hat{\epsilon}). \tag{5.4}$$

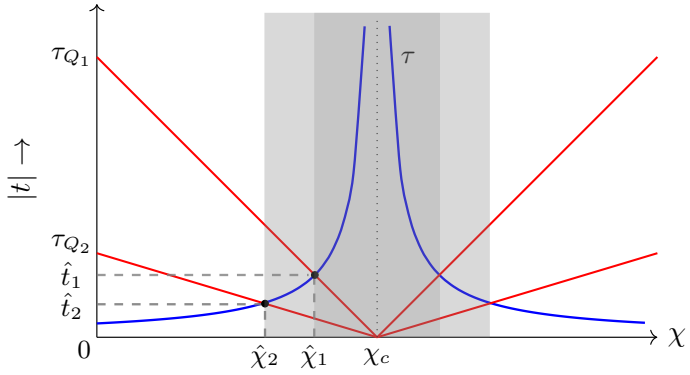

Figure 5.2: Schematic illustration of the relaxation time curve (blue) and the inverse transition rate curve (red) as a function of quench parameter χ, for two quench rates $\tau_{Q_1} > \tau_{Q_2}$. The crossover between adiabatic and impulse regimes happens at time $\hat{t}$ with corresponding value of quench parameter $\hat{\chi}$.

Using the power law divergence of relaxation time given in Eq. (5.1) and the quench protocol given in Eq. (5.2), we get

$$\begin{aligned} \tau_Q|\hat{\epsilon}| &\propto |\hat{\epsilon}|^{-\nu z}, \\ |\hat{\epsilon}| &\propto \tau_Q^{-1/(1+\nu z)}, \\ |\hat{t}| &\propto \tau_Q^{\nu z/(1+\nu z)} = \tau_Q^{b z}, \end{aligned} \tag{5.5}$$

where, $b = \nu/(1+\nu z)$. In Fig. 5.2, the crossover between adiabatic and impulse evolution happens when the relaxation time curve (blue) and the inverse transition rate curve (red) intersects. It should be noted that for slower quenches (larger τ_Q), the width of the impulse region is smaller. However, due to the divergence of the relaxation time near the critical point, the impulse region can't be eliminated, howsoever slow the quench.

The critical slowing down of the system near the critical point is responsible for the generation of topological defects in the quenched state when it exits the impulse domain and enters the symmetry broken state. The KZM assumes that the dynamical state is frozen in the impulse domain $-\hat{t} < t < \hat{t}$. The correlation length doesn't vary during the impulse duration, thus, $\xi(\hat{t}) = \xi(-\hat{t}) = \hat{\xi}$ [84, 216]. The spontaneous symmetry breaking at $\chi(\hat{t})$, leads to the formation of correlated domains of size $\hat{\xi}$

with non-zero order parameter. The meeting point of these domains, with independent choices of the order parameter, constitutes topological defects in the quenched state. The correlation length and the topological defect density depends on the quench rate. The scaling relations can be obtained using Eq. (5.1) and Eq. (5.5) as

$$\begin{aligned} \hat{\xi} &\propto |\hat{\epsilon}|^{-\nu}, \\ \hat{\xi} &\propto \tau_Q^{\nu/(1+\nu z)} = \tau_Q^b. \end{aligned} \tag{5.6}$$

If def is the dimension of the topological defect and D is the spatial dimension, then the topological defect density $\hat{N}$ at time $\hat{t}$ is given by

$$\begin{aligned} \hat{N} &\propto \hat{\xi}^{\mathrm{def}}/(\hat{\xi})^D, \\ \hat{N} &\propto \tau_Q^{(\mathrm{def}-D)\nu/(1+\nu z)} = \tau_Q^{-d}, \end{aligned} \tag{5.7}$$

where, $d = (D - \mathrm{def})\nu/(1 + \nu z)$. The scaling relations, described by Eq. (5.5) - (5.7) forms the key testable predictions of the KZM.

5.1.2 Quantum Kibble-Zurek mechanism

The KZM was originally formulated for the thermal phase transitions and subsequently extended to accommodate QPTs [108, 217]. In isolated quantum systems at zero temperature, the inverse of the energy gap Δ between the ground state and the first excited state sets the natural time scale. And, it plays a role analogous to the relaxation time in thermal phase transitions. For the case of QPTs, the adiabatic evolution of the quenched state is followed if the instantaneous energy gap separating the excitations is larger than the relative change in the energy gap with the quench. Thus, the adiabatic evolution halts near the critical point where the energy gap vanishes with a power law divergence $\Delta \propto |\epsilon|^{\nu z}$. The breakdown of the adiabaticity occurs in the regime where $d(\log \Delta)/dt \geqslant \Delta$. Thus, the time instant demarking the adiabatic and non-adiabatic evolution is

$$\begin{aligned} \frac{d}{dt}\log\hat{\Delta} &\sim \hat{\Delta}, \\ \frac{d}{dt}\log|\hat{\epsilon}|^{\nu z} &\sim |\hat{\epsilon}|^{\nu z}, \\ \frac{d}{dt}\log\left(\frac{|\hat{t}|}{\tau_Q}\right)^{\nu z} &\sim \left(\frac{|\hat{t}|}{\tau_Q}\right)^{\nu z}, \end{aligned}$$

$$|\hat{t}| \sim (\tau_Q)^{\nu z/(1+\nu z)}.$$

This is similar to the KZM scaling relation in Eq. (5.5), obtained for thermal phase transitions. A relation similar to Eq. (5.7) for the defect density in QPTs can also be obtained [110].

In this work, we study the quench dynamics across the MI-SF QPT in BHM. We observe the validity of the KZ power law scaling relations, however, there are deviations from the key assumption of KZM on the frozen state dynamics in the impulse regime. This assumption also been critically explored in previous works [218–220].

5.2 Quantum quench in BHM

In this section, we shall discuss the dynamics of ultracold atoms trapped in optical lattices, described by the BHM Hamiltonian, under a quantum quench. These novel systems offer precise control over system parameters and are ideal for studying the dynamics of the system under a quench. Furthermore, these systems allow investigations on quantum phases in the strongly interacting regimes. For ultracold atoms in a 2D optical lattice, the BHM Hamiltonian is given by

$$\hat{H}_{\text{BHM}} = \sum_{p,q} \left[-J\left(\hat{b}^{\dagger}_{p+1,q}\hat{b}_{p,q} + \hat{b}^{\dagger}_{p,q+1}\hat{b}_{p,q} + \text{H.c.}\right) + \frac{U}{2}\hat{n}_{p,q}(\hat{n}_{p,q}-1) - \mu\hat{n}_{p,q}\right], \quad (5.8)$$

where p, q are lattice site coordinates along the x and y directions, respectively. The system parameters, hopping strength J and chemical potential μ are scaled by the on-site interaction energy U, which is set unity. The competition between J and μ, gives MI and SF quantum phases in various parameter regimes with a QPT between the two. In this Chapter, we shall examine the quench dynamics across the MI-SF QPT. This is achieved by varying J at constant μ, and we consider two cases. First, for the QPT across the multicritical point located at the tip of the MI lobe, and second, for a generic QPT located below the tip of the MI lobe. There exist few experimental investigations on KZ scaling laws for quench across the MI-SF QPT [145, 146]. Theoretical investigations with numerical techniques like truncated Wigner approximation[221], variational wavefunction [114], time-dependent Gutzwiller [142, 222–225] have been done to study KZ scaling laws in BHM and its extensions. In this study, we have em-

ployed time-dependent single-site Gutzwiller and cluster-Gutzwiller mean-field methods to investigate the KZ scaling laws for QPTs separating the MI and SF phases of BHM Hamiltonian. In the phase diagram of BHM in J/U - μ/U plane, the MI phase exists as a lobe, separated from the SF phase by a QPT. At the tip of the lobe, the QPT is continuous and belongs to the universality class of 3D XY model with critical exponents $\nu = 2/3$ and $z = 1$. Away from the tip, the QPT occurs with the critical exponents $\nu = 1/2$ and $z = 2$ [13]. To investigate this change in the nature of the critical exponents, we have studied the quench dynamics at the tip and below the tip of the Mott lobe. Below the tip of the Mott lobe, the excitations are predominantly of hole type which is computationally favourable as it helps in putting a lower cut-off for the single-site Fock space basis in CGMF calculations. To begin with, we first discuss the quench protocol and some properties of the quenched state.

5.2.1 Quench Protocol

The quench across the MI-SF QPT is studied by choosing a linear quench protocol for dynamical variation in the hopping strength, which as discussed earlier in Eq. (5.2), is given by

$$J(t) = J_i + (J_c - J_i)\frac{t + \tau_Q}{\tau_Q}. \tag{5.9}$$

Here, J_i corresponds to the value of the hopping strength at the beginning of the quench, which commences at $t = -\tau_Q$. The initial value J_i is chosen so that the system is in the MI state. And, the critical value for the QPT J_c, obtained from equilibrium studies, is attained at $t = 0$. The hopping strength is linearly quenched with time and is terminated only after the quenched state has transformed to the superfluid state. The parameter τ_Q determines the rate at which the parameter is quenched, thus controlling the adiabaticity of the process.

5.2.2 Quenched state in MI and SF regimes

The superfluid phase is distinguished from the MI phase using the average SF order parameter

$$\phi = \frac{1}{N_s}\sum_{p,q} |\phi_{p,q}|, \tag{5.10}$$

where N_s is the total number of lattice sites. The quenched state in the superfluid regime is populated with the topological defects, vortices and anti-vortices generated by spontaneous symmetry breaking at the QPT. The number of topological defects in the quenched state can be counted as the absolute sum of the vorticity summed over all lattice sites, given by

$$N_{\rm v} = \sum_{p,q} |\Omega_{p,q}|. \tag{5.11}$$

The vorticity $\Omega_{p,q}$ at site (p, q) is given by the phase winding in the SF order parameter for a closed loop around site (p, q), given by

$$\begin{aligned} \Omega_{p,q} \;\; = \;\; & \frac{1}{4}\big[\sin(\theta_{p+1,q} - \theta_{p,q}) + \sin(\theta_{p+1,q+1} - \theta_{p+1,q}) \\ & - \sin(\theta_{p+1,q+1} - \theta_{p,q+1}) - \sin(\theta_{p,q+1} - \theta_{p,q})\big], \end{aligned} \tag{5.12}$$

where, $\theta_{p,q}$ is the phase of local SF order parameter $\phi_{p,q}$. Now, we start with discussions on the quench across the generic phase transition, below the tip of the Mott lobe, with SGMF methodology.

5.3 Quench across MI-SF QPT at $\mu = 0.3$

Let us start the discussion with the initial state preparation scheme. The initial state is the equilibrium state for $\mu = 0.3$ and $J = 0$ on a 96×96 square lattice. For the parameters chosen, the equilibrium state corresponds to the MI phase with unit occupancy on all the sites. To the wavefunction of the state, we add random fluctuations. This is crucial as it mimics the quantum fluctuations necessary to drive the QPT. In this regard, we choose entirely random uni-variate phase fluctuation in the range 0 to 2π and is added to the phase of the coefficient of dominating basis state in the equilibrium wavefunction. Furthermore, we introduce a density fluctuation of the order 10^{-3}, chosen from a random univariate distribution, and is then added to all the coefficients. We note that the magnitude of the density fluctuations added to the initial wavefunction affects the cross-over time $\hat{t}$. A larger magnitude of the fluctuations shifts $\hat{t}$ closer to the critical point J_c and this can be seen from Fig. 5.3. We, however, find that this

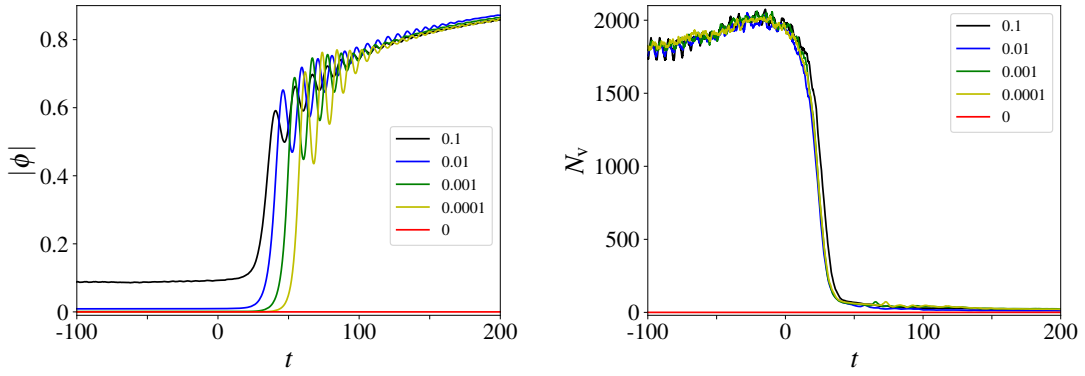

Figure 5.3: Plot showing the effect of density noise, introduced in the initial wavefunction as a part of the state-preparation protocol, on the dynamical state under quench for $\tau_Q = 100$. The magnitude of the density noise is chosen across a range of values for which the dynamical quantities are plotted with different colors for different magnitudes of noise. As evident from red colored lines, the dynamical state remains in the same phase if the density fluctuations are not introduced.

doesn't affect the power law scalings of the cross-over time and defect density. Furthermore, the magnitude of the density fluctuations introduced can be estimated following a detailed analysis of the quantum and thermal fluctuations using the Bogoliubov-de Gennes analysis of the collective modes [223]. This dressed state is then used as the initial state, which is then evolved in time by varying J as per the quench protocol. The dynamical state at a later time is obtained by solving the time-dependent Gutzwiller equations using the RK4 method till the quench is terminated in the SF regime. For solving the coupled Gutzwiller equations using RK4 method, we choose $\Delta t = 0.005$ as the time step. Calculations done with a smaller time step, $\Delta t = 0.001$, suggest no effect on the dynamical state in the region of study. It should be emphasized that owing to the random fluctuations in the initial state, the dynamical properties of the state should be sample averaged. For this purpose, we choose a 40 different realizations of the initial state. Additionally, we have chosen a large lattice of dimension 96×96, with periodic boundary conditions along the two spatial dimensions, in order to have a good statistics over the defects generated in the quench process. The lattice dimension of 96×96 is cleverly chosen so that it can be tiled using 2×2 and 2×3 clusters for CGMF studies, discussed in later part of this Chapter.

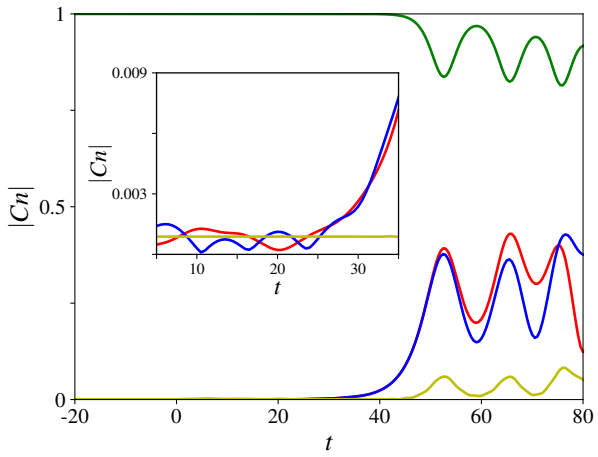

Figure 5.4: Dynamical evolution of the absolute magnitude of some dominating Fock state coefficients using SGMF methodology for $\tau_Q = 100$. For studying the trend, we choose the state at the middle of the lattice, with wavefunction given by $|\Psi_{\mathrm{GW}}\rangle^{(p,q)} = \sum_n c_n^{(p,q)} |n\rangle_{p,q}$. The green colored curve corresponds to the coefficient of the state $|n = 1\rangle$ and red curve corresponds to that of $|n = 0\rangle$ state. The blue and yellow curves represent the coefficients for the basis states $|n = 2\rangle$ and $|n = 3\rangle$ respectively.

5.3.1 Quench dynamics using single-site Gutzwiller mean-field

Using equilibrium SGMF code, we generate the initial MI(1) state with a sufficiently large cutoff $N_b = 6$ on the single-site occupancies. The temporal evolution of the dressed state (one realization) under a quench in J is shown in Fig. 5.4 for some dominating basis states. In the figure, the temporal dependence of the coefficient of most dominant $|n = 1\rangle_{p,q}$ Fock state basis is shown in green color. And the red, blue and yellow colored curves correspond to the Fock states with 0, 2 and 3 occupancies, respectively. As seen from the figure, away from the critical point, the quenched state follows adiabatic evolution and remains the MI(1) state. However, the quenched state retains MI(1) character till some time after crossing the criticality at $t = 0$. On careful inspection, the quenched state has fluctuations of the order of the density noise introduced in the initial dressed state. This is shown in the inset of the figure. Thus, the state is frozen with respect to time near the critical point, which agrees with the assumption of the "impulse" regime in KZM. Afterwards, the evolution starts when J is sufficiently away from J_c, and the quenched state exhibits characteristics of the SF phase, which can be seen from the SF order parameter.

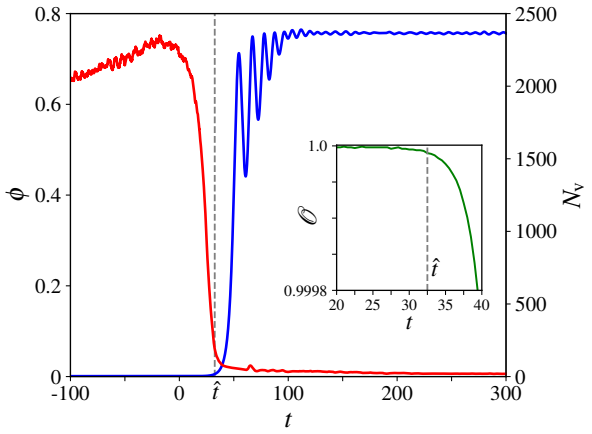

Figure 5.5: Temporal evolution of the SF order parameter ϕ (blue) and defect density $N_{\rm v}$ (red) $\tau_Q = 100$. The quenched is terminated at $t = 100$, following which free evolution starts. The crossover time $\hat{t}$ is marked with dashed grey line, identified using the overlap measure $\mathcal{O}$, shown in the inset.

5.3.1.1 Temporal evolution of ϕ and $N_{\rm v}$

Fig. 5.5 shows the temporal evolution of averaged SF order parameter ϕ (blue colored curve) of quenched state for quench rate $\tau_Q = 100$. The quench is terminated at $t = \tau_Q$, corresponding to $J = 2J_c$, and afterwards, the state is allowed to evolve freely. In the figure, ϕ is initially zero (of order 10^{-3}), signifying a MI state. This small value of ϕ originates from the density fluctuations introduced in the dressed initial state. It shows a delayed growth till $t = \hat{t} > 0$, after which ϕ rises exponentially. This is due to the formation of uncorrelated SF domains inside which the order parameter continues to grow. This is followed by some oscillatory behavior as a result of the phase ordering process. These oscillation decays with time with a global phase coherence in the system. After $t = \tau_Q$, the free evolution starts and ϕ shows a saturation.

In Fig. 5.5, the red colored curve shows the temporal evolution of the defect density $N_{\rm v}$. As a result of the completely random phase fluctuations added to the initial dressed state, the quenched state has a large number of defects, which denotes the phase windings. Near criticality, N_v starts decaying rapidly and these phase windings disappear with the phase redistribution. After $\hat{t}$, uncorrelated domains of SF phase starts growing in the system, with annihilation of vortex- anti-vortex pairs, N_v keeps decreasing with the time as the system becomes phase coherent. The KZM predicts the number

of defects at the crossover time $\hat{t}$ to follow a power law scaling with τ_Q.

5.3.1.2 Overlap measure for locating $\hat{t}$

To locate the crossover time $\hat{t}$, we utilize the KZM assumption that dynamical evolution stops and the state is frozen in the impulse regime, where the wavefunction changes by only a phase factor. Backed by the observation shown in Fig. 5.4, we use the overlap measure to locate $\hat{t}$. This is defined as the inner product of the dynamical wavefunction at any time with the wavefunction at time $t = 0$, given by

$$\mathcal{O}(t) = |\langle\psi(0)|\psi(t)\rangle|. \tag{5.13}$$

The deviation of the overlap from unity signals the crossover time $\hat{t}$. In our calculations, we find the overlap starts varying rapidly at the value of overlap around 0.99999. This value is observed to be dependent on the magnitude of the density fluctuations in the dressed state. Subsequently, we choose a threshold value for overlap to be 0.99999 as a locator for $\hat{t}$. The overlap measure is shown in the inset of the Fig. 5.5.

To show the distribution of the SF order parameter at various times, we plot the amplitude and phase of $\phi_{p,q}$ at various times in Fig. 5.6 for one sample realization. The amplitude profile is shown in Fig. 5.6 (a-c) while Fig. 5.6 (d-f) shows the phase profile at times $t = 0$, $\hat{t}$, and τ_Q. The initial dressed state, with $\phi \sim 10^{-3}$, is seeded with a large number of defects. This persists till $t = 0$, as shown in Fig. 5.6 (a,d). Towards the end of the impulse at $t = \hat{t}$, uncorrelated domains of SF with small amplitudes of order parameter appear, as shown in Fig. 5.6 (b,e). These SF domains continue to grow with the annihilation of vortex- anti-vortex in pairs and the system moves towards a global phase coherence with time. This can be seen at time $t = \tau_Q$, shown in Fig. 5.6 (c,e).

5.3.2 Kibble-Zurek scalings

Now we discuss the results for scaling behaviour of the crossover time and defect density $\hat{N}_v$, with the quench rate in the range $\tau_Q \in \{10, 1000\}$. As shown in left panel of Fig. 5.7, we observe a power-law scaling for $\hat{t}$ and $\hat{N}_v$, however, it shows a slight deviation at the extreme values of the quench rate. The deviation is more pronounced for defect density in the case of extremely fast quench. However, with extremely slow

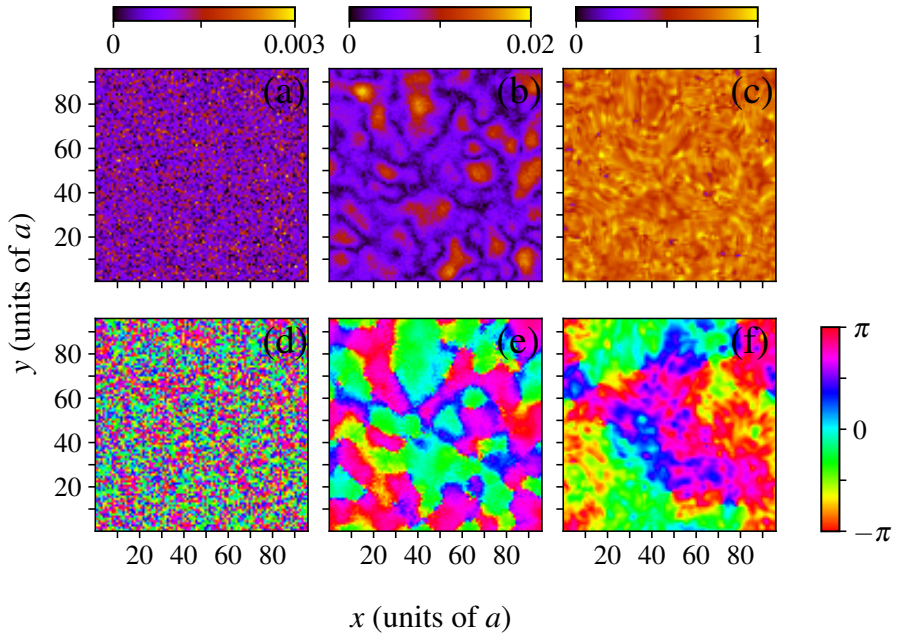

Figure 5.6: Panels (a-c) show snapshots of $|\phi_{p,q}|$ while panels (d-f) show the phase profile of $\phi_{p,q}$ at various time instants $t = 0, \hat{t}$, and τ_Q during the quench for $\tau_Q = 100$.

quenches (large τ_Q), the variation in defect density across the sample is large. From the power law fit of the data, in the regime $\tau_Q \in [25, 300]$, we observe $\hat{t} \propto \tau_Q^{0.496\pm0.004}$ and $\hat{N}_{\rm v} \propto \tau_Q^{-0.348\pm0.038}$. A comparison of these exponents with Eq. (5.5) and Eq. (5.7) gives $bz = 0.496 \pm 0.004$ and $d = 0.348 \pm 0.038$.

It's important to mention that there exist various works where the crossover time $\hat{t}$ is defined as the instant when the average SF order parameter reaches twice its value at criticality, that is $\phi(\hat{t}) = 2\phi(0)$ [142, 144]. In the vicinity of this time instant, there is a rapid increase in ϕ, however, this choice of the growth factor of 2 is somewhat arbitrary. So, we investigate the power law scaling with the identification of $\hat{t}$ with various choices of the growth factor, defined as $\phi(\hat{t})/\phi(0)$. We observe the power law scalings for $\hat{t}$ and $\hat{N}_{\rm v}$. However, the obtained exponents exhibit large variations depending on the choice of the growth factor. This is shown in the right panel of Fig. 5.7. It can be seen that the variation with the choice of growth factor goes away only for very large values ~ 20. This happens because, near this time, the rate at which ϕ grows is quite large and different choices of growth factor correspond to neighboring time instants. A comparison of the obtained results with the scaling exponents obtained

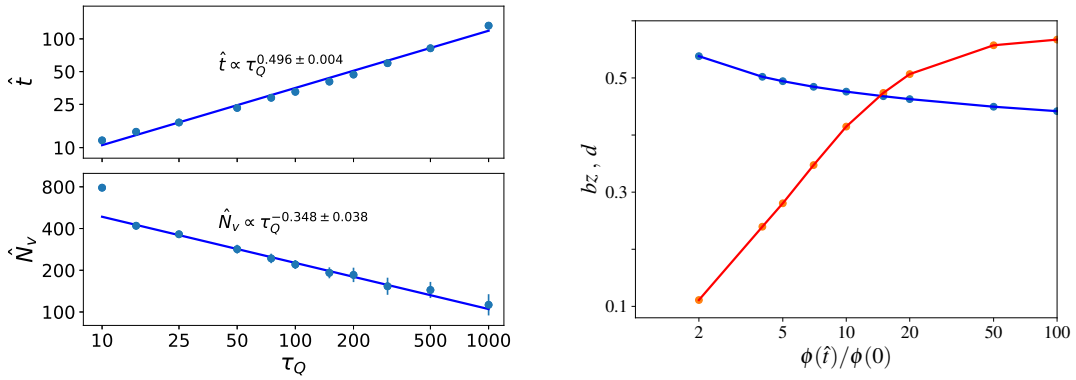

Figure 5.7: The left panel shows the power law scaling of $\hat{t}$ and $\hat{N}_{\rm v}$ as a function of τ_Q, using overlap measure for locating $\hat{t}$. The power law fit is done for $\tau_Q \in [25, 300]$. The Right panel shows the dependence of the power law exponents of $\hat{t}$ (bz), with blue curve, and of $\hat{N}_{\rm v}$ (d), with red curve, on $\phi(\hat{t})/\phi(0)$ which is used for locating $\hat{t}$.

using overlap criteria agrees with a growth factor ~ 7.

We consider that the defect produced in the quench corresponds to $\mathrm{def} = 1$. This is because, the topological defects are always produced in the form of vortex-anti-vortex pairs, thereby constituting a 1D defect. Fig. 5.8 shows the temporal dependence of the number of defects with positive and negative vorticity. In the figure, it can be seen that they are almost equal in number. The large number of defects at $t = -\tau_Q$, corresponds to phase windings in the initial state dressed with entirely random phase fluctuations. And as the quench progresses, these defects are created and annihilated in pairs. With this, we obtain the critical exponents $\nu = 0.69 \pm 0.11$ and $z = 1.42 \pm 0.17$. These dynamically obtained exponents should be compared with the equilibrium values, which correspond to the mean-field exponents $\nu = 1/2$ and $z = 2$. Next, we discuss the results obtained for the dynamics with the CGMF methodology.

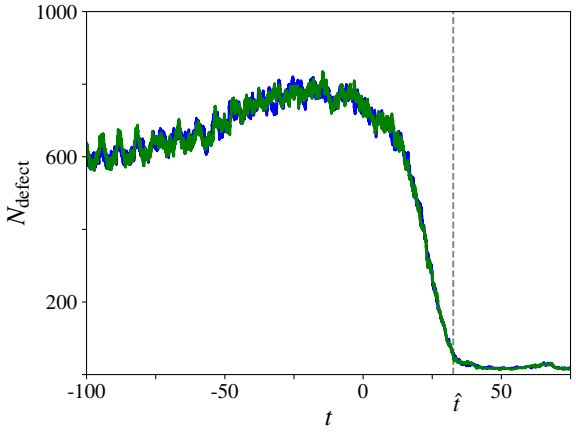

Figure 5.8: Temporal evolution of the topological defects in the quenched state. Blue curve shows the number of vortices with a vorticity $\Omega_{p,q} > 0.5$, while the green curve shows the number of anti-vortices with a vorticity $\Omega_{p,q} < -0.5$. The blue and green curves are almost identical, implying a equal number of vortex and anti-vortex in the quenched state.

5.3.3 Quench dynamics with CGMF

With the CGMF method, we revisit the dynamics of the quenched state and study its properties. For this, we have chosen 2×2 and 2×3 clusters to tile the 96×96 lattice. Since the Fock-space size increases with the cluster dimension, we allow the single-site occupancy to be atmost 2. The basis state dimension now becomes 81 for the 2×2 cluster, and 729 for the 2×3. Thus, choosing large sized clusters is difficult. To circumvent this problem, state reduction can be done where the basis states are filtered out. However, in a quench near the critical point of the phase transition, excitations are seeded in the state, which renders the process of state reduction unfeasible. We have checked that the extra energy due to these excitations depends upon the quench rate.

Furthermore, compared to the SGMF method, we observe the intra-cluster dynamics near the critical point. This can be seen in Fig. 5.9, where we have plotted the absolute value for some of the basis state coefficients with 2×2 cluster CGMF. The strength of the uniform unit filling basis state with 4 particles, shown with green curve, decreases with time. While, other 4 particle basis state, shown with red curve, increases with time. The CGMF method, thus, captures the evolution of the dynamical state in

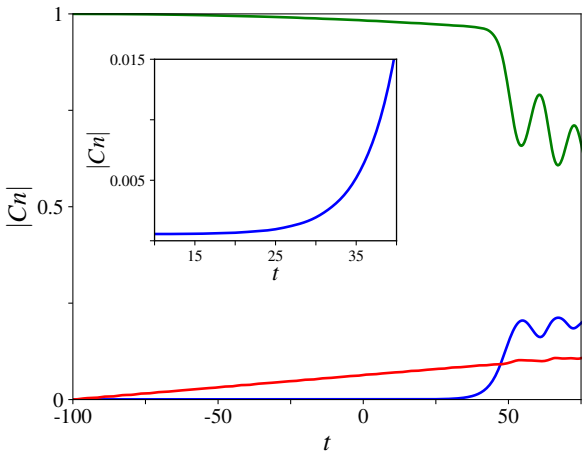

Figure 5.9: Temporal evolution of the absolute magnitude of the coefficients of the basis states with 2×2 cluster CGMF for $\tau_Q = 100$. For studying the trend, we choose the cluster state at the middle of the lattice, with the state given by $|\psi^{\alpha}\rangle = \sum_{n_1 n_2 n_3 n_4} c^{(\alpha)}_{n_1 n_2 n_3 n_4} |n_1 n_2 n_3 n_4\rangle$. The green curve corresponds to $c^{(\alpha)}_{1111}$, while red curve corresponds to coefficient of states such as $|0211\rangle$ and its permutations. The coefficients of the basis states with extra particle/hole, with respect to the unit filling, like $|0111\rangle$, $|2111\rangle$ and their permutations are plotted as blue curve.

the "impulse" regime of the KZM. This is due to the better accounting of correlations captured by the exact treatment of intra-cluster hopping terms. Since the impulse region is absent, the overlap measure, defined earlier, deviates quite early from unity and is not suitable for identifying $\hat{t}$. This is shown in Fig. 5.10. The crossover time $\hat{t}$ marks the development of the SF order parameter and inter-cluster dynamics. In Fig. 5.9, this time instant corresponds to $t \sim 30$ where the coefficient of the basis states with extra particle/hole on top of uniform unit filling, shown with blue curve, starts growing. The SF order parameter at this instant starts rapidly growing, as seen from the inset of Fig. 5.10.

As mentioned earlier, with SGMF, the power law exponents obtained from the overlap measure are quite close to that obtained by the criteria $\phi(\hat{t}) = 7\phi(0)$. Motivated by this, we use this definition of the 7-fold growth in ϕ for locating $\hat{t}$ in CGMF studies. We note that the crossover time and $\hat{N}_{\rm v}$ follow a power-law scaling with τ_Q. This is shown in the left panels of Fig. 5.11 and Fig. 5.12 for the CGMF case with 2×2 and 2×3 clusters, respectively. Similar to the SGMF case, it is observed that the power-law

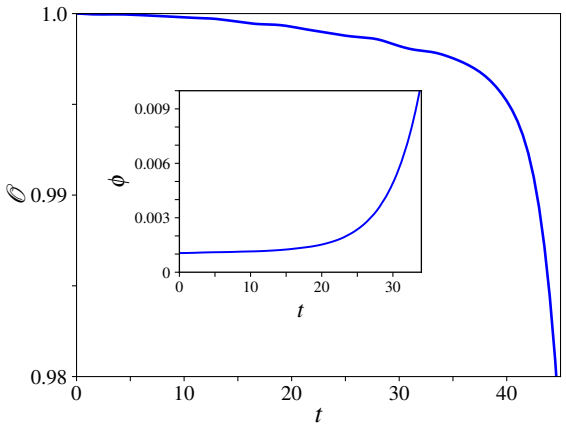

Figure 5.10: Overlap measure with CGMF using 2×2 clusters at $\tau_Q = 100$. Overlap measure is not suitable for locating $\hat{t}$, as it starts deviating quite early and doesn't show a sharp decay. The average SF order parameter is shown in the inset.

behaviour show deviations for extreme of τ_Q. Thus, in order to obtain the exponents of the power-law, we have fitted the data in the range $\tau_Q \in [25, 300]$. As the previous case, we find that different choices for $\phi(\hat{t})/\phi(0)$, gives different scaling exponents. This is shown in the right panels of Fig. 5.11 and Fig. 5.12 for 2×2 and 2×3 clusters, respectively. We extract the critical exponents ν and z using KZ scalings $\hat{t} \propto (\tau_Q)^{\frac{\nu z}{1+\nu z}}$, and $\hat{N}_{\rm v} \propto (\tau_Q)^{\frac{\nu}{1+\nu z}}$. Table 5.1 shows the comparison of critical exponents dynamically obtained using the SGMF and CGMF methods and with the definition $\phi(\hat{t}) = 7\phi(0)$. Here, 1×1 refers to the SGMF case. We find that the critical exponent ν, which characterizes the divergence of the correlation length, show a marginal change without any specific trend with the SGMF and CGMF methods. However, the critical exponent z, which characterizes the divergence of the system's characteristic time, shows an increasing trend with the larger cluster sizes. These dynamically obtained exponents can be compared with the equilibrium mean-field exponents $\nu = 1/2$ and $z = 2$.

5.4 Quench across the tip of MI(1) lobe

The QPT at the tip of the Mott lobe is a continuous phase transition and belongs to the universality class of the 3D XY model. In the parameter space, the tip of the MI(1) lobe occurs at the value of chemical potential, $\mu \approx 0.4$. Like in the earlier

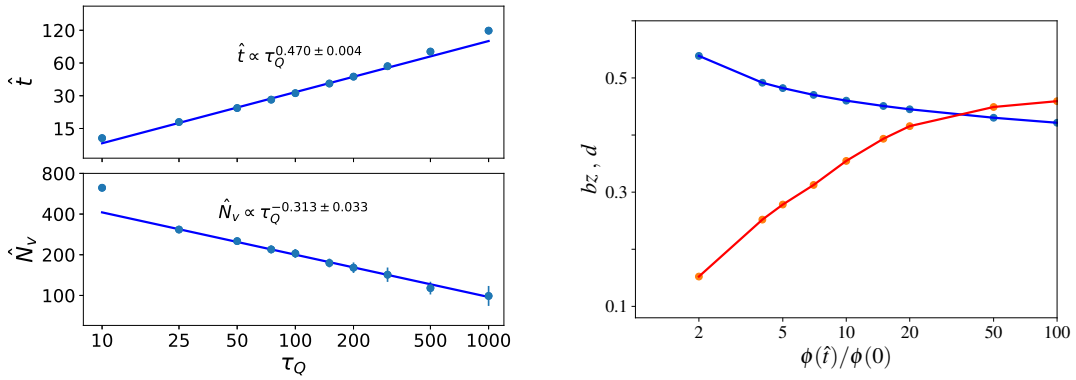

Figure 5.11: Left panel shows the power law scaling of $\hat{t}$ and $\hat{N}_{\rm v}$ as a function of τ_Q, using CGMF with 2×2 clusters. The crossover time is identified by the relation $\phi(\hat{t}) = 7\phi(0)$. The power law fit is done for $\tau_Q \in [25, 300]$. Right panel shows the dependence of the power law exponents of $\hat{t}$ (bz), with blue curve, and of $\hat{N}_{\rm v}$ (d), with red curve, on $\phi(\hat{t})/\phi(0)$ which is used for locating $\hat{t}$.

cluster	1×1	2×2	2×3	equilibrium
$\frac{\nu z}{1+\nu z}$	0.484 ± 0.003	0.470 ± 0.004	0.508 ± 0.005	0.5
$\frac{\nu}{1+\nu z}$	0.347 ± 0.034	0.313 ± 0.033	0.319 ± 0.037	0.25
z	1.39 ± 0.15	1.50 ± 0.17	1.59 ± 0.20	2
ν	0.67 ± 0.09	0.59 ± 0.09	0.65 ± 0.11	0.5

Table 5.1: Comparison of dynamically obtained critical exponent against various cluster sizes, for QPT at $\mu = 0.3$.

case of quench below the tip, here too, we study the properties of the dynamical state under a quench across the multi-critical point at the tip of the MI(1) lobe ($\mu = 0.4$). As discussed previously, we start with an equilibrium MI(1) state and dress it with the appropriate fluctuations in the density and the phase. This dressed state is then allowed to evolve under a linear quench in the hopping strength across the QPT into the SF regime. We study the averaged SF order parameter and the defect density in the quenched state with time. As observed previously, the symmetry breaking is observed at $t = \hat{t} > 0$, after which the quenched state possess characteristics of the superfluid state. The multicritical point at $J = J_c$ is reached at time $t = 0$. In addition, topological defects are generated in the quenched state and destroyed near the critical

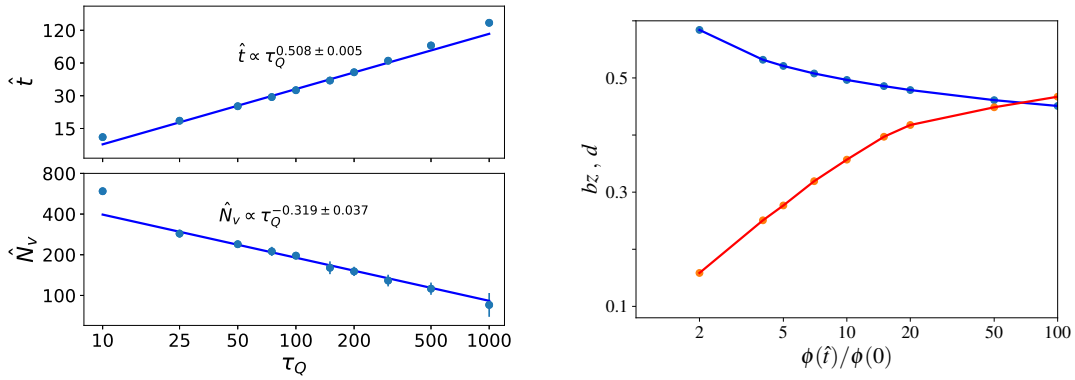

Figure 5.12: Left panel shows the power law scaling of $\hat{t}$ and $\hat{N}_{\rm v}$ as a function of τ_Q, using CGMF with 2×3 clusters. The crossover time is identified by the relation $\phi(\hat{t}) = 7\phi(0)$. The power law fit is done for $\tau_Q \in [25, 300]$. Right panel shows the dependence of the power law exponents of $\hat{t}$ (bz), with blue curve, and of $\hat{N}_{\rm v}$ (d), with red curve, on $\phi(\hat{t})/\phi(0)$ which is used for locating $\hat{t}$.

point through vortex- anti-vortex pair annihilations. We note the crossover time at which the quenched state becomes SF, and the defect density at this time instant for a range of values for quench rate $\tau_Q \in [10, 1000]$.

Studying the evolution of the quenched state with the SGMF method, we observe an impulse regime near the criticality at $t = 0$. This allows usage of the overlap protocol, defined earlier, to locate $\hat{t}$. Noting $\hat{t}$ and $\hat{N}_{\rm v}$ for various quench rates, we find these have power-law dependence on the quench rate. This trend is evident from the plots shown in Fig. 5.13. The power law fitting of the data for $\tau_Q \in [25, 300]$, gives $\hat{t} \propto \tau_Q^{0.421 \pm 0.004}$ and $\hat{N}_{\rm v} \propto \tau_Q^{-0.325 \pm 0.036}$. We find similar power-law exponents for the case of locating the crossover using the relation $\phi(\hat{t}) = 7\phi(0)$, similar to the previously discussed case of the quench at $\mu = 0.3$. The power-law exponents obtained at $\mu = 0.4$ are different from the values obtained earlier with SGMF for quench at $\mu = 0.3$. This is expected as the QPT at the tip is special and belongs to the universality class of 3D XY model. Using these power-law scalings, we extract $\nu = 0.56 \pm 0.09$ and $z = 1.30 \pm 0.16$. These dynamically obtained critical exponents are to be compared with the critical exponents of the 3D XY model, $\nu = 2/3$ and $z = 1$.

Next, we study the quench dynamics with CGMF using 2×2 and 2×3 clusters and track the evolution of the dynamical state. Similar to the previous observation for

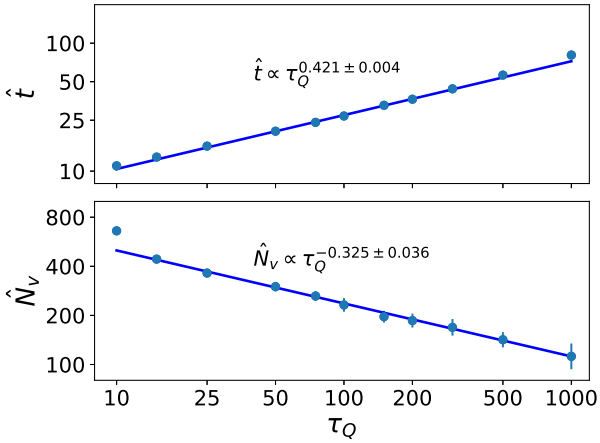

Figure 5.13: Power law scaling of $\hat{t}$ and $\hat{N}_v$ at the tip of the MI(1) lobe ($\mu = 0.4$), using the SGMF method. The crossover time is located using the overlap measure.

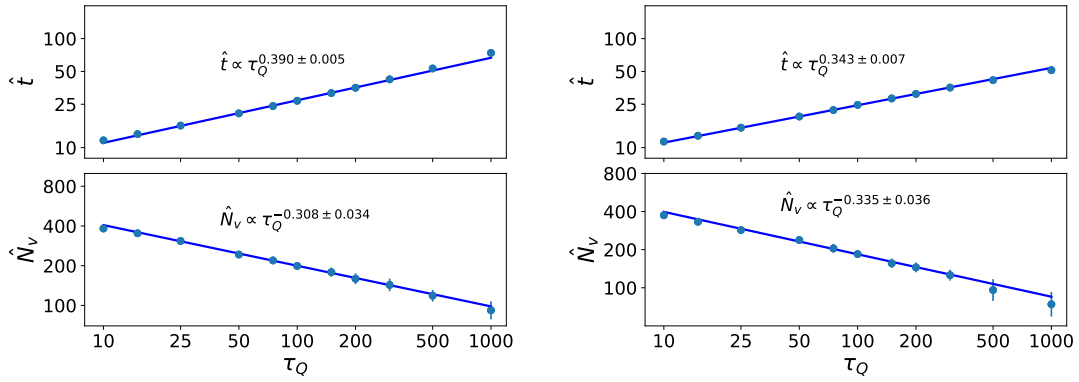

Figure 5.14: Power law scaling of $\hat{t}$ and $\hat{N}_v$, with 2×2 (left panel) and 2×3 (right panel) clusters.

QPT at $\mu = 0.3U$, we observe the "impulse regime" is absent and the dynamical state evolves near the criticality. Thus, the overlap measure is not suitable for locating $\hat{t}$. So, we use the definition $\phi(\hat{t}) = 7\phi(0)$ for identifying the crossover time for various quench rates. As a function of the quench rate, the crossover time and the defect density $\hat{N}_\mathrm{v}$ shows a power-law behavior as shown in Fig. 5.14. A comparison of the power-law exponents obtained with the SGMF and CGMF methods, with $\hat{t}$ identified by the definition $\phi(\hat{t}) = 7\phi(0)$, is shown in Table 5.2. We find that from the dynamics, $\nu \sim 1/2$ and $z \sim 1$ which can be compared with the critical exponents of the 3D XY model, $\nu = 2/3$ and $z = 1$.

cluster	1×1	2×2	2×3	equilibrium
$\frac{\nu z}{1+\nu z}$	0.407 ± 0.004	0.390 ± 0.005	0.343 ± 0.007	0.4
$\frac{\nu}{1+\nu z}$	0.335 ± 0.032	0.308 ± 0.034	0.335 ± 0.036	0.4
z	1.21 ± 0.13	1.27 ± 0.16	1.02 ± 0.13	1
ν	0.57 ± 0.08	0.50 ± 0.09	0.51 ± 0.10	$2/3$

Table 5.2: Critical exponent for $\hat{t}$ and $\hat{N}_v$ for various cluster sizes, for QPT at tip of MI(1) lobe $\mu = 0.4$.

5.5 Summary of the chapter

In this chapter, we have studied the quench dynamics across the MI-SF quantum phase transition of BHM. For a linear quench in J and at fixed $\mu = 0.3$, and 0.4, we have studied the properties of the quenched state. We find power-law scalings for the crossover time and the defect density, with the quench rate, as predicted by KZM. However, the power-law behavior deviates at extreme values of the quench rate. We have used the SGMF and CGMF methodologies for our studies. With the CGMF method, we note the evolution of the dynamical state in the "impulse" regime of KZM. The critical exponents obtained from the quench dynamics study are close to their equilibrium values. We note that, with larger cluster sizes, the critical exponent z improves towards equilibrium value. This is expected as z, which is the dynamical critical exponent, is associated with the divergence of the system's characteristic time. And, a larger sized cluster with a large number of basis states allows better study of the dynamics through redistribution of initial state population amongst various low-lying states.

Chapter 6

Summary and future scope

In summary, this thesis focuses on the exploration of the FQH states in a system of ultracold bosonic atoms confined in a 2D square optical lattice. We have modeled the system with the bosonic Harper-Hofstadter model in the presence of artificial gauge fields. We present the ground-state compressibility plot and discuss the parameter domains of the incompressible states that have filling factors similar to that of the FQH states. We use the CGMF method, with appropriate cluster sizes, to obtain the ground state quantum phases. The CGMF method is good at capturing the quantum correlations within the state, making it well-suited for studying the FQH state. To characterize these incompressible states, we use the ED method with a fixed number of particles corresponding to $\nu = 1/2$ filling. The study of two-point correlation function shows signatures of a gapped bulk and gapless edges. With the calculation of the MBCN, we demonstrate the topological order of the $\nu = 1/2$ state. For the case of dipolar atoms with long-range interactions, we extend the model with the interactions truncated to NN. We demonstrate that within certain parameter regimes, the $\nu = 1/2$ FQH state emerges as the ground state of the extended Hamiltonian. The dipolar interactions preserve the topological order of the FQH state and ensure its stability against the competing SF phase.

In addition, in this thesis, we have introduced a novel implementation of the exact diagonalization method suitable for bosonic optical lattice systems. This implementation utilizes a hierarchical approach for generating the basis states of the lattice systems. The hierarchical construction generates the single-site Fock states, row-states,

multi-row states, and finally, the basis states for the entire lattice. This multi-step approach allows the "state-reduction", where some basis states are filtered out to reduce the dimension of the Hamiltonian matrix. This implementation efficiently constructs the matrix with the identification and calculation of only non-zero matrix elements. With theoretical arguments and backed by numerics, we show that the time required in the matrix construction almost scales linearly with the dimension of the matrix and the number of lattice sites. Furthermore, each step of the implementation is parallelizable over multiple nodes for faster computations. We use this ED procedure for studying the bipartite entanglement entropy in the $\nu = 1/2$ FQH state on a large lattice. The extraction of topological entanglement entropy (TEE) from the area law is ambiguous due to the definition of the boundary length on lattice system. This ambiguity can be neglected for larger sized lattices. The TEE calculated with subdivision of lattice in terms of "plural areas" [191], shows a mismatch between the calculated value and the theoretical estimates. However, our calculations suggest it can approach the theoretical estimate with a larger choice of lattice dimension.

In addition to equilibrium investigations, we have explored the quench dynamics of ultracold bosonic atoms confined in optical lattices. In particular, we have focused on quench in hopping strength J, at constant μ, across the MI-SF quantum phase transition. In our study, we have chosen a linear quench protocol for quench across the multicritical point at the tip of the Mott(1) lobe and for a generic QPT at $\mu = 0.3$. With SGMF, we find the dynamical state doesn't evolve near the critical point of QPT, in accordance with the "impulse" region approximation of KZM. This allows the use of the overlap measure for identifying the impulse to adiabatic crossover time $\hat{t}$. We demonstrate the KZM predictions of power law scalings for $\hat{t}$ and defect density as a function of quench rate. However, with CGMF, the "impulse" region is absent. So, we locate $\hat{t}$ based on the rise in averaged SF order parameter. We note a power law behavior similar to the SGMF, but with slightly different exponents. The critical exponents obtained in our study are close to their equilibrium counterparts. It is noteworthy that the deviation of the critical exponent z from the equilibrium value decreases with larger cluster sizes. This may be due to the better capturing of dynamics with the availability of more accessible basis states.

Scope for future works

This thesis opens up new avenues for future research, which include the following key areas of focus:

- Using the spatial bipartite entanglement to identify minimal entangled states, the modular matrix and corresponding quasiparticle statistics can be extracted for topologically nontrivial systems. We wish to study this for non-Abelian FQH states in future works.

- Our studies on bipartite entanglement in FQH state in chapter 3 suggest improvement in the calculated TEE with larger lattice size. With larger lattices, the area law can be examined to study the sub-leading corrections arising from the geometry of the boundary. We wish to study this in future works.

- With the advancements in technology, very recently the $\nu = 1/2$ FQH state was experimentally realized for ^{87}Rb atoms in optical lattice. Our study in chapter 4 suggests the possibility of observing this topological state with dipolar condensates in the near future.

- In our study on FQH phases, we have limited ourselves to closed systems. In the pursuit of realizing these phases in the experiments, the effects of dissipations arising from the interactions with the surroundings should be investigated. There are some investigations within the framework of Markovian dynamics, however, the effect of non-Markovian environment should be explored.

- The quench dynamics study in chapter 5 can be extended to examine the domain growth, phase ordering kinetics, and entanglement growth following the quench. We wish to study these in future works.

Appendix A

An example of hierarchical wavefunction

As an example, let us focus on describing a quantum phase corresponding to a hole fluctuation over a commensurate filling of 2 bosons per site on a 3×3 lattice. As mentioned earlier, we generate the basis states of 3×3 lattice using hierarchical wavefunctions: row-states and multi-row states. Now, in the row-state construction, we can constrain the single-site occupancies so that it can assume values as 1 or 2 only. Furthermore, since we are interested in a quantum phase with 1 less particle over uniform filling of 2 bosons per site, we filter the possible row-state configurations by imposing the constraint that within a row, comprising of only 3 lattice sites, the total number of bosons can be either 5 or 6. With these constraints, $\eta = 1$, $N_B = 3$, and $\sigma = 5$ and $\sigma + \delta = 6$, the possible row-state configurations, totalling to $\beta = 4$ in number are listed in Table A.1. From this Table, it can be observed that the row-state configurations $|\phi_m\rangle \equiv |n_1, n_2, n_3\rangle$, are uniquely identified by corresponding row-state quantum number m and by the state index i assigned according to the ordering in m.

Next, in the hierarchical order, we consider the multi-row state comprising of two rows corresponding to a 3×2 lattice. We construct the two-row states $\left|\Phi^2_M\right\rangle$ from the direct product of row-states $|\phi_m\rangle$, chosen from Table A.1 with some appropriate constraints on the total number of particles in the state. Recalling that we are interested in representing a quantum phase with hole fluctuation over uniform filling of 2 bosons per site, we constrain the two-row states such that total number of bosons in the two

$\lvert\phi_m\rangle \equiv$ $\lvert n_1 \quad n_2 \quad n_3\rangle$	$\lvert 1 \quad 2 \quad 2\rangle$	$\lvert 2 \quad 1 \quad 2\rangle$	$\lvert 2 \quad 2 \quad 1\rangle$	$\lvert 2 \quad 2 \quad 2\rangle$
m	3	5	6	7
i	1	2	3	$\beta = 4$

Table A.1: Table showing all possible row-state configurations together with the corresponding values of the row-state quantum number m and state index i. The possible row-states are constrained by $\eta = 1$, $N_B = 3$, $\sigma = 5$ and $\delta = 1$.

rows can be either 11 or 12. With this constraint, possible two-row states, $\beta^{(2)} = 7$ in number, are shown in Table A.2. Finally, the basis states corresponding to the system of $N = 17$ particles on a 3×3 lattice can be constructed from direct product of rowstates and two-row states, constructed earlier in Table A.1 and A.2. This is done by constraining the total number of particles in the basis state to be equal to 17. Table A.3 lists all such possible basis states, which are $\Gamma = 9$ in number.

$\begin{matrix} \vert\phi_{m_2}\rangle \\ \vert\Phi^2_M\rangle = \quad \otimes \\ \vert\phi_{m_1}\rangle \end{matrix}$	$\mathbf{M} = (m_1, m_2)$	$M = \|\mathbf{M}\|$	I
$\left\vert \begin{matrix} 2 & 2 & 2 \\ 1 & 2 & 2 \end{matrix} \right\rangle$	$(3, 7)$	31	1
$\left\vert \begin{matrix} 2 & 2 & 2 \\ 2 & 1 & 2 \end{matrix} \right\rangle$	$(5, 7)$	47	2
$\left\vert \begin{matrix} 2 & 2 & 2 \\ 2 & 2 & 1 \end{matrix} \right\rangle$	$(6, 7)$	55	3
$\left\vert \begin{matrix} 1 & 2 & 2 \\ 2 & 2 & 2 \end{matrix} \right\rangle$	$(7, 3)$	59	4
$\left\vert \begin{matrix} 2 & 1 & 2 \\ 2 & 2 & 2 \end{matrix} \right\rangle$	$(7, 5)$	61	5
$\left\vert \begin{matrix} 2 & 2 & 1 \\ 2 & 2 & 2 \end{matrix} \right\rangle$	$(7, 6)$	62	6
$\left\vert \begin{matrix} 2 & 2 & 2 \\ 2 & 2 & 2 \end{matrix} \right\rangle$	$(7, 7)$	63	$\beta^{(2)} = 7$

Table A.2: Table illustrating all possible two-row states $\left|\Phi^2_M\right\rangle$, together with the vector label $\mathbf{M}$ containing the contributing row-state configurations. The two-row states are constrained by allowing the total particles within two rows to vary as either 11 or 12 only. The state index I is sequenced according to M.

$\begin{matrix} \vert\phi_{m_3}\rangle \\ \otimes \\ \vert\Phi^3_M\rangle = \vert\phi_{m_2}\rangle \\ \otimes \\ \vert\phi_{m_1}\rangle \end{matrix}$	$\mathbf{M} = (m_1, m_2, m_3)$	$M = \Vert\mathbf{M}\Vert$	I
$\left\vert \begin{matrix} 2 & 2 & 2 \\ 2 & 2 & 2 \\ 1 & 2 & 2 \end{matrix} \right\rangle$	$(3, 7, 7)$	255	1
$\left\vert \begin{matrix} 2 & 2 & 2 \\ 2 & 2 & 2 \\ 2 & 1 & 2 \end{matrix} \right\rangle$	$(5, 7, 7)$	383	2
$\left\vert \begin{matrix} 2 & 2 & 2 \\ 2 & 2 & 2 \\ 2 & 2 & 1 \end{matrix} \right\rangle$	$(6, 7, 7)$	447	3
$\left\vert \begin{matrix} 2 & 2 & 2 \\ 1 & 2 & 2 \\ 2 & 2 & 2 \end{matrix} \right\rangle$	$(7, 3, 7)$	479	4
$\left\vert \begin{matrix} 2 & 2 & 2 \\ 2 & 1 & 2 \\ 2 & 2 & 2 \end{matrix} \right\rangle$	$(7, 5, 7)$	495	5
$\left\vert \begin{matrix} 2 & 2 & 2 \\ 2 & 2 & 1 \\ 2 & 2 & 2 \end{matrix} \right\rangle$	$(7, 6, 7)$	503	6
$\left\vert \begin{matrix} 1 & 2 & 2 \\ 2 & 2 & 2 \\ 2 & 2 & 2 \end{matrix} \right\rangle$	$(7, 7, 3)$	507	7
$\left\vert \begin{matrix} 2 & 1 & 2 \\ 2 & 2 & 2 \\ 2 & 2 & 2 \end{matrix} \right\rangle$	$(7, 7, 5)$	509	8
$\left\vert \begin{matrix} 2 & 2 & 1 \\ 2 & 2 & 2 \\ 2 & 2 & 2 \end{matrix} \right\rangle$	$(7, 7, 6)$	510	$\Gamma = 9$

Table A.3: Table illustrating all possible basis-states identified by the corresponding vector label $\mathbf{M}$ for a system of 17 particles on a 3×3 lattice.

Appendix B

Harper-Hofstadter Hamiltonian

Let us consider the kinetic part of the second-quantized Hamiltonian introduced in Eq. (2.1) of Chapter 2, which describes neutral bosonic atoms in a lattice potential. The effect of a homogeneous magnetic field $\mathbf{B} = \nabla \times \mathbf{A}$, can be incorporated with the minimal coupling $\mathbf{p} \to \mathbf{p} - e\mathbf{A}$. The kinetic part of the Hamiltonian is then given by

$$\hat{H}_{\text{kin}} = \int \mathrm{d}\mathbf{r} \hat{\Psi}^{\dagger}(\mathbf{r}) \frac{(-i\hbar\nabla - e\mathbf{A})^2}{2m} \hat{\Psi}(\mathbf{r}) \tag{B.1}$$

Assuming tight-binding limit and lowest-band approximation, we can expand the field operators in terms of the Wannier functions of the lowest Bloch band, with an appropriate phase factor to account the effect of magnetic field as

$$\hat{\Psi}(\mathbf{r}) = \sum_i e^{i\frac{e}{\hbar}\int_{\mathbf{R_i}}^{\mathbf{r}} \mathbf{A}.\mathrm{d}\mathbf{r}'} \, w_0(\mathbf{r} - \mathbf{R_i}) \, \hat{b}_i, \tag{B.2}$$

Using Eq. (B.2) in Eq. (B.1) and assuming vanishing overlap between the Wannier functions of distant lattice, we get

$$\begin{aligned}
\hat{H}_{\text{kin}} &= \sum_{\langle i,j \rangle} \hat{b}_i^{\dagger}\hat{b}_j \int \mathrm{d}\mathbf{r} e^{-i\frac{e}{\hbar}\int_{\mathbf{R_i}}^{\mathbf{r}} \mathbf{A}.\mathrm{d}\mathbf{r}'} \, w_0^*(\mathbf{r} - \mathbf{R_i}) \frac{(-i\hbar\nabla - e\mathbf{A})^2}{2m} e^{i\frac{e}{\hbar}\int_{\mathbf{R_j}}^{\mathbf{r}} \mathbf{A}.\mathrm{d}\mathbf{r}'} \, w_0(\mathbf{r} - \mathbf{R_j}) \\
&= \sum_{\langle i,j \rangle} \hat{b}_i^{\dagger}\hat{b}_j \, \frac{1}{2m} \int \mathrm{d}\mathbf{r} e^{-i\frac{e}{\hbar}\int_{\mathbf{R_i}}^{\mathbf{r}} \mathbf{A}.\mathrm{d}\mathbf{r}'} \, e^{i\frac{e}{\hbar}\int_{\mathbf{R_j}}^{\mathbf{r}} \mathbf{A}.\mathrm{d}\mathbf{r}'} \, w_0^*(\mathbf{r} - \mathbf{R_i}) \frac{-\hbar^2\nabla^2}{2m} w_0(\mathbf{r} - \mathbf{R_j}) \\
&= \sum_{\langle i,j \rangle} \hat{b}_i^{\dagger}\hat{b}_j \, e^{i\frac{e}{\hbar}\int_{\mathbf{R_j}}^{\mathbf{R_i}} \mathbf{A}.\mathrm{d}\mathbf{r}'} \, \frac{1}{2m} \int \mathrm{d}\mathbf{r} e^{-i\frac{e}{\hbar}\oint \mathbf{A}.\mathrm{d}\mathbf{r}'} \, w_0^*(\mathbf{r} - \mathbf{R_i}) \frac{-\hbar^2\nabla^2}{2m} w_0(\mathbf{r} - \mathbf{R_j})
\end{aligned} \tag{B.3}$$

where, $\oint \mathbf{A}.\mathrm{d}\mathbf{r}'$ is over the closed path $\mathbf{R_i} \to \mathbf{r} \to \mathbf{R_j} \to \mathbf{R_i}$. This integral is non-zero for $\mathbf{r}$ farther from $\mathbf{R}$ and $\mathbf{R}'$ where the overlap of Wannier function vanishes. Thus, we

get

$$\hat{H}_{\text{kin}} = \sum_{\langle i,j \rangle} e^{i\frac{e}{\hbar}\int_{\mathbf{R_j}}^{\mathbf{R_i}} \mathbf{A}.\mathrm{d}\mathbf{r}'} \left(\int \mathrm{d}\mathbf{r} w_0^*(\mathbf{r} - \mathbf{R_i}) \frac{\hbar^2 \nabla^2}{2m} w_0(\mathbf{r} - \mathbf{R_j}) \right) \hat{b}_i^\dagger \hat{b}_j. \tag{B.4}$$

Considering the remaining interaction terms of Eq. (2.1), similarly as done in Chapter 2, we obtain the bosonic analogue of the Harper-Hofstadter Hamiltonian

$$\hat{H} = \sum_{\langle i,j \rangle} e^{i\phi_{ij}} J_{ij} \hat{b}_i^\dagger \hat{b}_j + \frac{U}{2} \sum_i \hat{n}_i(\hat{n}_i - 1) - \mu \sum_i \hat{n}_i, \tag{B.5}$$

where, $\phi_{ij} = \dfrac{e}{\hbar} \displaystyle\int_{\mathbf{R_j}}^{\mathbf{R_i}} \mathbf{A}.\mathrm{d}\mathbf{r}'$ is the complex phase factor associated with the hopping term and J_{ij}, U are given by Eq. (2.5) and Eq. (2.6) respectively.

Bibliography

[1] M. H. Anderson, J. R. Ensher, M. R. Matthews, C. E. Wieman, and E. A. Cornell, *Observation of bose-einstein condensation in a dilute atomic vapor,* Science **269**, 198–201 (1995).

[2] K. B. Davis, M. O. Mewes, M. R. Andrews, N. J. van Druten, D. S. Durfee, D. M. Kurn, and W. Ketterle, *Bose-einstein condensation in a gas of sodium atoms,* Phys. Rev. Lett. **75**, 3969–3973 (1995).

[3] C. C. Bradley, C. A. Sackett, J. J. Tollett, and R. G. Hulet, *Evidence of bose-einstein condensation in an atomic gas with attractive interactions,* Phys. Rev. Lett. **75**, 1687–1690 (1995).

[4] S. L. Cornish, N. R. Claussen, J. L. Roberts, E. A. Cornell, and C. E. Wieman, *Stable* $^{85}\mathrm{Rb}$ *bose-einstein condensates with widely tunable interactions,* Phys. Rev. Lett. **85**, 1795–1798 (2000).

[5] A. Robert, O. Sirjean, A. Browaeys, J. Poupard, S. Nowak, D. Boiron, C. I. Westbrook, and A. Aspect, *A bose-einstein condensate of metastable atoms,* Science **292**, 461–464 (2001).

[6] Y. Takasu, K. Maki, K. Komori, T. Takano, K. Honda, M. Kumakura, T. Yabuzaki, and Y. Takahashi, *Spin-singlet bose-einstein condensation of two-electron atoms,* Phys. Rev. Lett. **91**, 040404 (2003).

[7] B. P. Anderson and M. A. Kasevich, *Macroscopic quantum interference from atomic tunnel arrays,* Science **282**, 1686 (1998).

[8] M. Kozuma, L. Deng, E. W. Hagley, J. Wen, R. Lutwak, K. Helmerson, S. L. Rolston, and W. D. Phillips, *Coherent splitting of bose-einstein condensed*

atoms with optically induced bragg diffraction, Phys. Rev. Lett. **82**, 871–875 (1999).

[9] J. Stenger, S. Inouye, A. P. Chikkatur, D. M. Stamper-Kurn, D. E. Pritchard, and W. Ketterle, *Bragg spectroscopy of a bose-einstein condensate,* Phys. Rev. Lett. **82**, 4569–4573 (1999).

[10] Y. B. Ovchinnikov, J. H. Müller, M. R. Doery, E. J. D. Vredenbregt, K. Helmerson, S. L. Rolston, and W. D. Phillips, *Diffraction of a released bose-einstein condensate by a pulsed standing light wave,* Phys. Rev. Lett. **83**, 284–287 (1999).

[11] E. W. Hagley, L. Deng, M. Kozuma, M. Trippenbach, Y. B. Band, M. Edwards, M. Doery, P. S. Julienne, K. Helmerson, S. L. Rolston, and W. D. Phillips, *Measurement of the coherence of a bose-einstein condensate,* Phys. Rev. Lett. **83**, 3112–3115 (1999).

[12] M. Greiner, I. Bloch, O. Mandel, T. W. Hänsch, and T. Esslinger, *Exploring phase coherence in a 2D lattice of Bose-Einstein condensates,* Phys. Rev. Lett. **87**, 160405 (2001).

[13] M. P. A. Fisher, P. B. Weichman, G. Grinstein, and D. S. Fisher, *Boson localization and the superfluid-insulator transition,* Phys. Rev. B **40**, 546 (1989).

[14] D. Jaksch, C. Bruder, J. I. Cirac, C. W. Gardiner, and P. Zoller, *Cold bosonic atoms in optical lattices,* Phys. Rev. Lett. **81**, 3108 (1998).

[15] M. Greiner, O. Mandel, T. Esslinger, T. W. Hänsch, and I. Bloch, *Quantum phase transition from a superfluid to a Mott insulator in a gas of ultracold atoms,* Nature (London) **415**, 39 (2002).

[16] M. Boninsegni and N. Prokof'ev, *Supersolid phase of hard-core bosons on a triangular lattice,* Phys. Rev. Lett. **95**, 237204 (2005).

[17] I. Danshita and C. A. R. Sá de Melo, *Stability of superfluid and supersolid phases of dipolar bosons in optical lattices,* Phys. Rev. Lett. **103**, 225301 (2009).

[18] S. Bandyopadhyay, R. Bai, S. Pal, K. Suthar, R. Nath, and D. Angom, *Quantum phases of canted dipolar bosons in a two-dimensional square optical lattice,* Phys. Rev. A **100**, 053623 (2019).

[19] K. Suthar, R. Kraus, H. Sable, D. Angom, G. Morigi, and J. Zakrzewski, *Staggered superfluid phases of dipolar bosons in two-dimensional square lattices,* Phys. Rev. B **102**, 214503 (2020).

[20] K. Günter, T. Stöferle, H. Moritz, M. Köhl, and T. Esslinger, *Bose-Fermi mixtures in a three-dimensional optical lattice,* Phys. Rev. Lett. **96**, 180402 (2006).

[21] J. Catani, L. De Sarlo, G. Barontini, F. Minardi, and M. Inguscio, *Degenerate Bose-Bose mixture in a three-dimensional optical lattice,* Phys. Rev. A **77**, 011603 (2008).

[22] R. Bai, D. Gaur, H. Sable, S. Bandyopadhyay, K. Suthar, and D. Angom, *Segregated quantum phases of dipolar bosonic mixtures in two-dimensional optical lattices,* Phys. Rev. A **102**, 043309 (2020).

[23] K. V. Krutitsky and P. Navez, *Excitation dynamics in a lattice bose gas within the time-dependent gutzwiller mean-field approach,* Phys. Rev. A **84**, 033602 (2011).

[24] T. Saito, I. Danshita, T. Ozaki, and T. Nikuni, *Detecting the superfluid critical momentum of bose gases in optical lattices through dipole oscillations,* Phys. Rev. A **86**, 023623 (2012).

[25] M. Aidelsburger, M. Atala, S. Nascimbène, S. Trotzky, Y.-A. Chen, and I. Bloch, *Experimental realization of strong effective magnetic fields in an optical lattice,* Phys. Rev. Lett. **107**, 255301 (2011).

[26] M. Aidelsburger, M. Atala, M. Lohse, J. T. Barreiro, B. Paredes, and I. Bloch, *Realization of the hofstadter hamiltonian with ultracold atoms in optical lattices,* Phys. Rev. Lett. **111**, 185301 (2013).

[27] J. Léonard, S. Kim, J. Kwan, P. Segura, F. Grusdt, C. Repellin, N. Goldman, and M. Greiner, *Realization of a fractional quantum hall state with ultracold atoms,* Nature **619**, 495–499 (2023).

[28] E. H. Hall, *On a new action of the magnet on electric currents,* American Journal of Mathematics **2**, 287–292 (1879).

[29] K. v. Klitzing, G. Dorda, and M. Pepper, *New method for high-accuracy determination of the fine-structure constant based on quantized hall resistance,* Phys. Rev. Lett. **45**, 494–497 (1980).

[30] D. C. Tsui, H. L. Stormer, and A. C. Gossard, *Two-dimensional magnetotransport in the extreme quantum limit,* Phys. Rev. Lett. **48**, 1559–1562 (1982).

[31] R. Willett, J. P. Eisenstein, H. L. Störmer, D. C. Tsui, A. C. Gossard, and J. H. English, *Observation of an even-denominator quantum number in the fractional quantum hall effect,* Phys. Rev. Lett. **59**, 1776–1779 (1987).

[32] R. B. Laughlin, *Anomalous quantum Hall effect: An incompressible quantum fluid with fractionally charged excitations,* Phys. Rev. Lett. **50**, 1395 (1983).

[33] J. K. Jain, *Composite-fermion approach for the fractional quantum hall effect,* Phys. Rev. Lett. **63**, 199–202 (1989).

[34] A. Sterdyniak, N. R. Cooper, and N. Regnault, *Bosonic integer quantum hall effect in optical flux lattices,* Phys. Rev. Lett. **115**, 116802 (2015).

[35] Y.-C. He, S. Bhattacharjee, R. Moessner, and F. Pollmann, *Bosonic integer quantum hall effect in an interacting lattice model,* Phys. Rev. Lett. **115**, 116803 (2015).

[36] T.-S. Zeng, *Integer quantum hall effect of two-component hard-core bosons in a topological triangular lattice,* Phys. Rev. B **105**, 235140 (2022).

[37] P. Soltan-Panahi, J. Struck, P. Hauke, A. Bick, W. Plenkers, G. Meineke, C. Becker, P. Windpassinger, M. Lewenstein, and K. Sengstock, *Multi-component quantum gases in spin-dependent hexagonal lattices,* Nature Physics **7**, 434–440 (2011).

[38] D.-S. Lühmann, O. Jürgensen, M. Weinberg, J. Simonet, P. Soltan-Panahi, and K. Sengstock, *Quantum phases in tunable state-dependent hexagonal optical lattices,* Phys. Rev. A **90**, 013614 (2014).

[39] C. Becker, P. Soltan-Panahi, J. Kronjäger, S. Dörscher, K. Bongs, and K. Sengstock, *Ultracold quantum gases in triangular optical lattices,* New Journal of Physics **12**, 065025 (2010).

[40] J. Struck, M. Weinberg, C. Ölschläger, P. Windpassinger, J. Simonet, K. Sengstock, R. Höppner, P. Hauke, A. Eckardt, M. Lewenstein, and L. Mathey, *Engineering ising-xy spin-models in a triangular lattice using tunable artificial gauge fields,* Nature Physics **9**, 738–743 (2013).

[41] L. Santos, M. A. Baranov, J. I. Cirac, H.-U. Everts, H. Fehrmann, and M. Lewenstein, *Atomic quantum gases in kagomé lattices,* Phys. Rev. Lett. **93**, 030601 (2004).

[42] T. H. Barter, T.-H. Leung, M. Okano, M. Block, N. Y. Yao, and D. M. Stamper-Kurn, *Spatial coherence of a strongly interacting bose gas in the trimerized kagome lattice,* Phys. Rev. A **101**, 011601 (2020).

[43] M. Greiner, O. Mandel, T. W. Hänsch, and I. Bloch, *Collapse and revival of the matter wave field of a bose-einstein condensate,* Nature **419**, 51 (2002).

[44] J. Hubbard, *Electron correlations in narrow energy bands,* Proc. Royal Soc. A **276**, 238 (1963).

[45] A. Griesmaier, J. Werner, S. Hensler, J. Stuhler, and T. Pfau, *Bose-Einstein condensation of chromium,* Phys. Rev. Lett. **94**, 160401 (2005).

[46] A. Griesmaier, *Generation of a dipolar bose–einstein condensate,* Journal of Physics B: Atomic, Molecular and Optical Physics **40**, R91–R134 (2007).

[47] M. Lu, N. Q. Burdick, S. H. Youn, and B. L. Lev, *Strongly dipolar Bose-Einstein condensate of dysprosium,* Phys. Rev. Lett. **107**, 190401 (2011).

[48] K. Aikawa, A. Frisch, M. Mark, S. Baier, A. Rietzler, R. Grimm, and F. Ferlaino, *Bose-Einstein condensation of erbium,* Phys. Rev. Lett. **108**, 210401 (2012).

[49] S. Baier, M. J. Mark, D. Petter, K. Aikawa, L. Chomaz, Z. Cai, M. Baranov, P. Zoller, and F. Ferlaino, *Extended Bose-Hubbard models with ultracold magnetic atoms,* Science **352**, 201 (2016).

[50] L. Chomaz, R. M. W. van Bijnen, D. Petter, G. Faraoni, S. Baier, J. H. Becher, M. J. Mark, F. Wächtler, L. Santos, and F. Ferlaino, *Observation of roton mode population in a dipolar quantum gas,* Nature Physics **14**, 442 (2018).

[51] D. Petter, G. Natale, R. M. W. van Bijnen, A. Patscheider, M. J. Mark, L. Chomaz, and F. Ferlaino, *Probing the roton excitation spectrum of a stable dipolar Bose gas,* Phys. Rev. Lett. **122**, 183401 (2019).

[52] Y. Miyazawa, R. Inoue, H. Matsui, G. Nomura, and M. Kozuma, *Bose-einstein condensation of europium,* Phys. Rev. Lett. **129**, 223401 (2022).

[53] C. Trefzger, C. Menotti, and M. Lewenstein, *Ultracold dipolar gas in an optical lattice: The fate of metastable states,* Phys. Rev. A **78**, 043604 (2008).

[54] C. Menotti, C. Trefzger, and M. Lewenstein, *Metastable states of a gas of dipolar bosons in a 2d optical lattice,* Phys. Rev. Lett. **98**, 235301 (2007).

[55] T. Lahaye, C. Menotti, L. Santos, M. Lewenstein, and T. Pfau, *The physics of dipolar bosonic quantum gases,* Reports on Progress in Physics **72**, 126401 (2009).

[56] J. Struck, C. Ölschläger, R. L. Targat, P. Soltan-Panahi, A. Eckardt, M. Lewenstein, P. Windpassinger, and K. Sengstock, *Quantum simulation of frustrated classical magnetism in triangular optical lattices,* Science **333**, 996–999 (2011).

[57] R. Peierls, *Zur theorie des diamagnetismus von leitungselektronen,* Zeitschrift für Physik **80**, 763–791 (1933).

[58] D. R. Hofstadter, *Energy levels and wave functions of Bloch electrons in rational and irrational magnetic fields,* Phys. Rev. B **14**, 2239 (1976).

[59] Y. Kuno, K. Shimizu, and I. Ichinose, *Bosonic analogs of the fractional quantum Hall state in the vicinity of Mott states,* Phys. Rev. A **95**, 013607 (2017).

[60] S. Pal, R. Bai, S. Bandyopadhyay, K. Suthar, and D. Angom, *Enhancement of the bose glass phase in the presence of an artificial gauge field,* Phys. Rev. A **99**, 053610 (2019).

[61] J. M. Zhang and R. X. Dong, *Exact diagonalization: the bose–hubbard model as an example,* European Journal of Physics **31**, 591–602 (2010).

[62] D. Raventós, T. Graß, M. Lewenstein, and B. Juliá-Díaz, *Cold bosons in optical lattices: a tutorial for exact diagonalization,* Journal of Physics B: Atomic, Molecular and Optical Physics **50**, 113001 (2017).

[63] A. Wietek and A. M. Läuchli, *Sublattice coding algorithm and distributed memory parallelization for large-scale exact diagonalizations of quantum many-body systems,* Phys. Rev. E **98**, 033309 (2018).

[64] A. M. Läuchli, J. Sudan, and E. S. Sørensen, *Ground-state energy and spin gap of spin-$\frac{1}{2}$ kagomé-heisenberg antiferromagnetic clusters: Large-scale exact diagonalization results,* Phys. Rev. B **83**, 212401 (2011).

[65] A. M. Läuchli, J. Sudan, and R. Moessner, *$s = \frac{1}{2}$ kagome heisenberg antiferromagnet revisited,* Phys. Rev. B **100**, 155142 (2019).

[66] N. K. Wilkin and J. M. F. Gunn, *Condensation of "composite bosons" in a rotating bec,* Phys. Rev. Lett. **84**, 6–9 (2000).

[67] B. Paredes, P. Fedichev, J. I. Cirac, and P. Zoller, *$\frac{1}{2}$-anyons in small atomic bose-einstein condensates,* Phys. Rev. Lett. **87**, 010402 (2001).

[68] N. K. Wilkin, J. M. F. Gunn, and R. A. Smith, *Do attractive bosons condense?* Phys. Rev. Lett. **80**, 2265–2268 (1998).

[69] J. Dalibard, F. Gerbier, G. Juzeliūnas, and P. Öhberg, *Colloquium: Artificial gauge potentials for neutral atoms,* Rev. Mod. Phys. **83**, 1523–1543 (2011).

[70] M. Aidelsburger, *Artificial gauge fields and topology with ultracold atoms in optical lattices,* Journal of Physics B: Atomic, Molecular and Optical Physics **51**, 193001 (2018).

[71] N. R. Cooper, J. Dalibard, and I. B. Spielman, *Topological bands for ultracold atoms,* Rev. Mod. Phys. **91**, 015005 (2019).

[72] P. Hauke and I. Carusotto, *Quantum hall and synthetic magnetic-field effects in ultra-cold atomic systems,* (2022).

[73] A. S. Sørensen, E. Demler, and M. D. Lukin, *Fractional quantum Hall states of atoms in optical lattices,* Phys. Rev. Lett. **94**, 086803 (2005).

[74] M. Hafezi, A. S. Sørensen, E. Demler, and M. D. Lukin, *Fractional quantum Hall effect in optical lattices,* Phys. Rev. A **76**, 023613 (2007).

[75] R. N. Palmer and D. Jaksch, *High-field fractional quantum Hall effect in optical lattices,* Phys. Rev. Lett. **96**, 180407 (2006).

[76] R. O. Umucal ılar and M. O. Oktel, *Phase boundary of the boson mott insulator in a rotating optical lattice,* Phys. Rev. A **76**, 055601 (2007).

[77] R. O. Umucalilar and E. J. Mueller, *Fractional quantum Hall states in the vicinity of Mott plateaus,* Phys. Rev. A **81**, 053628 (2010).

[78] G. Möller and N. R. Cooper, *Composite fermion theory for bosonic quantum hall states on lattices,* Phys. Rev. Lett. **103**, 105303 (2009).

[79] S. S. Natu, E. J. Mueller, and S. Das Sarma, *Competing ground states of strongly correlated bosons in the Harper-Hofstadter-Mott model,* Phys. Rev. A **93**, 063610 (2016).

[80] Y.-C. He, F. Grusdt, A. Kaufman, M. Greiner, and A. Vishwanath, *Realizing and adiabatically preparing bosonic integer and fractional quantum Hall states in optical lattices,* Phys. Rev. B **96**, 201103 (2017).

[81] M. Gerster, M. Rizzi, P. Silvi, M. Dalmonte, and S. Montangero, *Fractional quantum hall effect in the interacting hofstadter model via tensor networks,* Phys. Rev. B **96**, 195123 (2017).

[82] R. Bai, S. Bandyopadhyay, S. Pal, K. Suthar, and D. Angom, *Bosonic quantum Hall states in single-layer two-dimensional optical lattices,* Phys. Rev. A **98**, 023606 (2018).

[83] T. W. B. Kibble, *Topology of cosmic domains and strings,* Journal of Physics A: Mathematical and General **9**, 1387 (1976).

[84] W. H. Zurek, *Cosmological experiments in superfluid helium?* Nature **317**, 505 (1985).

[85] A. Polkovnikov, K. Sengupta, A. Silva, and M. Vengalattore, *Colloquium: Nonequilibrium dynamics of closed interacting quantum systems,* Rev. Mod. Phys. **83**, 863–883 (2011).

[86] A. del Campo and W. H. Zurek, *Universality of phase transition dynamics: Topological defects from symmetry breaking,* International Journal of Modern Physics A **29**, 1430018 (2014).

[87] M. Rigol, V. Dunjko, and M. Olshanii, *Thermalization and its mechanism for generic isolated quantum systems,* Nature **452**, 854–858 (2008).

[88] R. Nandkishore and D. A. Huse, *Many-body localization and thermalization in quantum statistical mechanics,* Annual Review of Condensed Matter Physics **6**, 15–38 (2015).

[89] K. Damle, S. N. Majumdar, and S. Sachdev, *Phase ordering kinetics of the bose gas,* Phys. Rev. A **54**, 5037–5041 (1996).

[90] A. J. Bray, *Theory of phase-ordering kinetics,* Advances in Physics **51**, 481–587 (2002).

[91] S. Puri, *Kinetics of phase transitions* (CRC press, 2009).

[92] L. Pastori, S. Barbarino, and J. C. Budich, *Signatures of topology in quantum quench dynamics and their interrelation,* Phys. Rev. Res. **2**, 033259 (2020).

[93] D. Kagamihara, R. Kaneko, S. Yamashika, K. Sugiyama, R. Yoshii, S. Tsuchiya, and I. Danshita, *Rényi entanglement entropy after a quantum quench starting from insulating states in a free boson system,* Phys. Rev. A **107**, 033305 (2023).

[94] J. Dziarmaga, *Dynamics of a quantum phase transition and relaxation to a steady state,* Advances in Physics **59**, 1063 (2010).

[95] P. C. Hendry, N. S. Lawson, R. A. M. Lee, P. V. E. McClintock, and C. D. H. Williams, *Generation of defects in superfluid 4he as an analogue of the formation of cosmic strings,* Nature **368**, 315–317 (1994).

[96] C. Bäuerle, Y. M. Bunkov, S. N. Fisher, H. Godfrin, and G. R. Pickett, *Laboratory simulation of cosmic string formation in the early universe using superfluid 3he,* Nature **382**, 332 (1996).

[97] V. M. H. Ruutu, V. B. Eltsov, A. J. Gill, T. W. B. Kibble, M. Krusius, Y. G. Makhlin, B. Plaçais, G. E. Volovik, and W. Xu, *Vortex formation in neutron-irradiated superfluid 3he as an analogue of cosmological defect formation,* Nature **382**, 334 (1996).

[98] I. Chuang, R. Durrer, N. Turok, and B. Yurke, *Cosmology in the laboratory: Defect dynamics in liquid crystals,* Science **251**, 1336 (1991).

[99] M. J. Bowick, L. Chandar, E. A. Schiff, and A. M. Srivastava, *The cosmological kibble mechanism in the laboratory: String formation in liquid crystals,* Science **263**, 943 (1994).

[100] R. Carmi, E. Polturak, and G. Koren, *Observation of spontaneous flux generation in a multi-josephson-junction loop,* Phys. Rev. Lett. **84**, 4966–4969 (2000).

[101] A. Maniv, E. Polturak, and G. Koren, *Observation of magnetic flux generated spontaneously during a rapid quench of superconducting films,* Phys. Rev. Lett. **91**, 197001 (2003).

[102] R. Monaco, J. Mygind, R. J. Rivers, and V. P. Koshelets, *Spontaneous fluxoid formation in superconducting loops,* Phys. Rev. B **80**, 180501 (2009).

[103] S.-Z. Lin, X. Wang, Y. Kamiya, G.-W. Chern, F. Fan, D. Fan, B. Casas, Y. Liu, V. Kiryukhin, W. H. Zurek, and S.-W. Batista, Cristian D.and Cheong, *Topological defects as relics of emergent continuous symmetry and higgs condensation of disorder in ferroelectrics,* Nature Physics **10**, 970 (2014).

[104] G. D. Chiara, A. del Campo, G. Morigi, M. B. Plenio, and A. Retzker, *Spontaneous nucleation of structural defects in inhomogeneous ion chains,* New Journal of Physics **12**, 115003 (2010).

[105] M. Mielenz, J. Brox, S. Kahra, G. Leschhorn, M. Albert, T. Schaetz, H. Landa, and B. Reznik, *Trapping of topological-structural defects in coulomb crystals,* Phys. Rev. Lett. **110**, 133004 (2013).

[106] S. Ulm, J. Roßnagel, G. Jacob, C. Degünther, S. T. Dawkins, U. G. Poschinger, R. Nigmatullin, A. Retzker, M. B. Plenio, F. Schmidt-Kaler, and K. Singer, *Observation of the kibble–zurek scaling law for defect formation in ion crystals,* Nature Communications **4**, 2290 (2013).

[107] K. Pyka, J. Keller, H. L. Partner, R. Nigmatullin, T. Burgermeister, D. M. Meier, K. Kuhlmann, A. Retzker, M. B. Plenio, W. H. Zurek, A. del Campo, and T. E. Mehlstäubler, *Topological defect formation and spontaneous symmetry breaking in ion coulomb crystals,* Nature Communications **4**, 2291 (2013).

[108] W. H. Zurek, U. Dorner, and P. Zoller, *Dynamics of a quantum phase transition,* Phys. Rev. Lett. **95**, 105701 (2005).

[109] B. Damski, *The simplest quantum model supporting the kibble-zurek mechanism of topological defect production: Landau-zener transitions from a new perspective,* Phys. Rev. Lett. **95**, 035701 (2005).

[110] A. Polkovnikov, *Universal adiabatic dynamics in the vicinity of a quantum critical point,* Phys. Rev. B **72**, 161201 (2005).

[111] R. Schützhold, M. Uhlmann, Y. Xu, and U. R. Fischer, *Sweeping from the superfluid to the mott phase in the bose-hubbard model,* Phys. Rev. Lett. **97**, 200601 (2006).

[112] J. Dziarmaga, *Dynamics of a quantum phase transition: Exact solution of the quantum ising model,* Phys. Rev. Lett. **95**, 245701 (2005).

[113] V. Mukherjee, U. Divakaran, A. Dutta, and D. Sen, *Quenching dynamics of a quantum xy spin-$\frac{1}{2}$ chain in a transverse field,* Phys. Rev. B **76**, 174303 (2007).

[114] F. M. Cucchietti, B. Damski, J. Dziarmaga, and W. H. Zurek, *Dynamics of the bose-hubbard model: Transition from a mott insulator to a superfluid,* Phys. Rev. A **75**, 023603 (2007).

[115] H. Saito, Y. Kawaguchi, and M. Ueda, *Kibble-zurek mechanism in a quenched ferromagnetic bose-einstein condensate,* Phys. Rev. A **76**, 043613 (2007).

[116] L. Cincio, J. Dziarmaga, M. M. Rams, and W. H. Zurek, *Entropy of entanglement and correlations induced by a quench: Dynamics of a quantum phase transition in the quantum ising model,* Phys. Rev. A **75**, 052321 (2007).

[117] K. Sengupta, D. Sen, and S. Mondal, *Exact results for quench dynamics and defect production in a two-dimensional model,* Phys. Rev. Lett. **100**, 077204 (2008).

[118] J. Dziarmaga, J. Meisner, and W. H. Zurek, *Winding up of the wave-function phase by an insulator-to-superfluid transition in a ring of coupled bose-einstein condensates,* Phys. Rev. Lett. **101**, 115701 (2008).

[119] C. De Grandi, V. Gritsev, and A. Polkovnikov, *Quench dynamics near a quantum critical point,* Phys. Rev. B **81**, 012303 (2010).

[120] F. Pollmann, S. Mukerjee, A. G. Green, and J. E. Moore, *Dynamics after a sweep through a quantum critical point,* Phys. Rev. E **81**, 020101 (2010).

[121] S. Sharma, S. Suzuki, and A. Dutta, *Quenches and dynamical phase transitions in a nonintegrable quantum ising model,* Phys. Rev. B **92**, 104306 (2015).

[122] M. M. Rams, J. Dziarmaga, and W. H. Zurek, *Symmetry breaking bias and the dynamics of a quantum phase transition,* Phys. Rev. Lett. **123**, 130603 (2019).

[123] R. Puebla, O. Marty, and M. B. Plenio, *Quantum kibble-zurek physics in long-range transverse-field ising models,* Phys. Rev. A **100**, 032115 (2019).

[124] A. Sinha, M. M. Rams, and J. Dziarmaga, *Kibble-zurek mechanism with a single particle: Dynamics of the localization-delocalization transition in the aubry-andré model,* Phys. Rev. B **99**, 094203 (2019).

[125] D. Sen, K. Sengupta, and S. Mondal, *Defect production in nonlinear quench across a quantum critical point,* Phys. Rev. Lett. **101**, 016806 (2008).

[126] L. E. Sadler, J. M. Higbie, S. R. Leslie, M. Vengalattore, and D. M. Stamper-Kurn, *Spontaneous symmetry breaking in a quenched ferromagnetic spinor bose–einstein condensate,* Nature **443**, 312 (2006).

[127] L. W. Clark, L. Feng, and C. Chin, *Universal space-time scaling symmetry in the dynamics of bosons across a quantum phase transition,* Science **354**, 606–610 (2016).

[128] B. Gardas, J. Dziarmaga, W. H. Zurek, and M. Zwolak, *Defects in quantum computers,* Scientific Reports **8**, 4539 (2018).

[129] A. Keesling, A. Omran, H. Levine, H. Bernien, H. Pichler, S. Choi, R. Samajdar, S. Schwartz, P. Silvi, S. Sachdev, P. Zoller, M. Endres, M. Greiner, V. Vuletić, and M. D. Lukin, *Quantum kibble–zurek mechanism and critical dynamics on a programmable rydberg simulator,* Nature **568**, 207–211 (2019).

[130] P. Weinberg, M. Tylutki, J. M. Rönkkö, J. Westerholm, J. A. Åström, P. Manninen, P. Törmä, and A. W. Sandvik, *Scaling and diabatic effects in quantum annealing with a d-wave device,* Phys. Rev. Lett. **124**, 090502 (2020).

[131] Y. Bando, Y. Susa, H. Oshiyama, N. Shibata, M. Ohzeki, F. J. Gómez-Ruiz, D. A. Lidar, S. Suzuki, A. del Campo, and H. Nishimori, *Probing the universality of topological defect formation in a quantum annealer: Kibble-zurek mechanism and beyond,* Phys. Rev. Research **2**, 033369 (2020).

[132] O. Morsch and M. Oberthaler, *Dynamics of bose-einstein condensates in optical lattices,* Rev. Mod. Phys. **78**, 179–215 (2006).

[133] G. Lamporesi, S. Donadello, S. Serafini, F. Dalfovo, and G. Ferrari, *Spontaneous creation of kibble–zurek solitons in a bose–einstein condensate,* Nature Physics **9**, 656 (2013).

[134] B. Damski and W. H. Zurek, *Quantum phase transition in space in a ferromagnetic spin-1 bose–einstein condensate,* New Journal of Physics **11**, 063014 (2009).

[135] B. Damski and W. H. Zurek, *Soliton creation during a bose-einstein condensation,* Phys. Rev. Lett. **104**, 160404 (2010).

[136] J. Beugnon and N. Navon, *Exploring the kibble–zurek mechanism with homogeneous bose gases,* Journal of Physics B: Atomic, Molecular and Optical Physics **50**, 022002 (2017).

[137] T. Donner, S. Ritter, T. Bourdel, A. Öttl, M. Köhl, and T. Esslinger, *Critical behavior of a trapped interacting bose gas,* Science **315**, 1556–1558 (2007).

[138] C. N. Weiler, T. W. Neely, D. R. Scherer, A. S. Bradley, M. J. Davis, and B. P. Anderson, *Spontaneous vortices in the formation of bose–einstein condensates,* Nature **455**, 948 (2008).

[139] L. Chomaz, L. Corman, T. Bienaimé, R. Desbuquois, C. Weitenberg, S. Nascimbène, J. Beugnon, and J. Dalibard, *Emergence of coherence via transverse condensation in a uniform quasi-two-dimensional bose gas,* Nature Communications **6**, 6162 (2015).

[140] S. Donadello, S. Serafini, T. Bienaimé, F. Dalfovo, G. Lamporesi, and G. Ferrari, *Creation and counting of defects in a temperature-quenched bose-einstein condensate,* Phys. Rev. A **94**, 023628 (2016).

[141] A. Eckardt, C. Weiss, and M. Holthaus, *Superfluid-insulator transition in a periodically driven optical lattice,* Phys. Rev. Lett. **95**, 260404 (2005).

[142] K. Shimizu, Y. Kuno, T. Hirano, and I. Ichinose, *Dynamics of a quantum phase transition in the bose-hubbard model: Kibble-zurek mechanism and beyond,* Phys. Rev. A **97**, 033626 (2018).

[143] K. Shimizu, T. Hirano, J. Park, Y. Kuno, and I. Ichinose, *Out-of-equilibrium dynamics of multiple second-order quantum phase transitions in an extended bose-hubbard model: Superfluid, supersolid, and density wave,* Phys. Rev. A **98**, 063603 (2018).

[144] Y. Zhou, Y. Li, R. Nath, and W. Li, *Quench dynamics of rydberg-dressed bosons on two-dimensional square lattices,* Phys. Rev. A **101**, 013427 (2020).

[145] D. Chen, M. White, C. Borries, and B. DeMarco, *Quantum quench of an atomic mott insulator,* Phys. Rev. Lett. **106**, 235304 (2011).

[146] S. Braun, M. Friesdorf, S. S. Hodgman, M. Schreiber, J. P. Ronzheimer, A. Riera, M. del Rey, I. Bloch, J. Eisert, and U. Schneider, *Emergence of coherence and the dynamics of quantum phase transitions,* Proceedings of the National Academy of Sciences **112**, 3641 (2015).

[147] C. Meldgin, U. Ray, P. Russ, D. Chen, D. M. Ceperley, and B. DeMarco, *Probing the Bose glass-superfluid transition using quantum quenches of disorder,* Nat. Phys. **12**, 646 (2016).

[148] A. D. King, S. Suzuki, J. Raymond, A. Zucca, T. Lanting, F. Altomare, A. J. Berkley, S. Ejtemaee, E. Hoskinson, S. Huang, E. Ladizinsky, A. J. R. MacDonald, G. Marsden, T. Oh, G. Poulin-Lamarre, M. Reis, C. Rich, Y. Sato, J. D. Whittaker, J. Yao, R. Harris, D. A. Lidar, H. Nishimori, and M. H. Amin, *Coherent quantum annealing in a programmable 2,000 qubit ising chain,* Nature Physics **18**, 1324–1328 (2022).

[149] I. Bloch, J. Dalibard, and W. Zwerger, *Many-body physics with ultracold gases,* Rev. Mod. Phys. **80**, 885 (2008).

[150] C. J. Pethick and H. Smith, *Bose-Einstein condensation in Dilute Gases* (Cambridge University Press (New York), 2002).

[151] M. Ueda, *Fundamentals and New Frontiers of Bose-Einstein Condensation* (World Scientific, 2010).

[152] I. Bloch, *Ultracold quantum gases in optical lattices,* Nature Physics **1**, 23 (2005).

[153] I. Bloch, J. Dalibard, and S. Nascimbène, *Quantum simulations with ultracold quantum gases,* Nature Physics **8**, 267–276 (2012).

[154] D. Jaksch and P. Zoller, *The cold atom Hubbard toolbox,* Annals of Physics **315**, 52 (2005).

[155] M. Lewenstein, A. Sanpera, V. Ahufinger, B. Damski, A. Sen(De), and U. Sen, *Ultracold atomic gases in optical lattices: mimicking condensed matter physics and beyond,* Adv. Phys. **56**, 243 (2007).

[156] O. Dutta, M. Gajda, P. Hauke, M. Lewenstein, D.-S. Lühmann, B. A. Malomed, T. Sowiński, and J. Zakrzewski, *Non-standard Hubbard models in optical lattices: a review,* Reports on Progress in Physics **78**, 066001 (2015).

[157] P. Sengupta, L. P. Pryadko, F. Alet, M. Troyer, and G. Schmid, *Supersolids versus phase separation in two-dimensional lattice bosons,* Phys. Rev. Lett. **94**, 207202 (2005).

[158] M. Lewenstein, A. Sanpera, and V. Ahufinger, *Ultracold Atoms in Optical Lattices: Simulating quantum many-body systems* (Oxford University Press, 2012).

[159] D. van Oosten, P. van der Straten, and H. T. C. Stoof, *Quantum phases in an optical lattice,* Phys. Rev. A **63**, 053601 (2001).

[160] M. P. Gelfand, R. R. P. Singh, and D. A. Huse, *Perturbation expansions for quantum many-body systems,* Journal of Statistical Physics **59**, 1093–1142 (1990).

[161] J. K. Freericks and H. Monien, *Strong-coupling expansions for the pure and disordered bose-hubbard model,* Phys. Rev. B **53**, 2691–2700 (1996).

[162] D. S. Rokhsar and B. G. Kotliar, *Gutzwiller projection for bosons,* Phys. Rev. B **44**, 10328 (1991).

[163] F. E. A. dos Santos and A. Pelster, *Quantum phase diagram of bosons in optical lattices,* Phys. Rev. A **79**, 013614 (2009).

[164] N. Teichmann, D. Hinrichs, M. Holthaus, and A. Eckardt, *Process-chain approach to the Bose-Hubbard model: Ground-state properties and phase diagram,* Phys. Rev. B **79**, 224515 (2009).

[165] T. D. Graß, F. E. A. dos Santos, and A. Pelster, *Excitation spectra of bosons in optical lattices from the schwinger-keldysh calculation,* Phys. Rev. A **84**, 013613 (2011).

[166] U. Schollwöck, *The density-matrix renormalization group,* Rev. Mod. Phys. **77**, 259–315 (2005).

[167] J. Carrasquilla, S. R. Manmana, and M. Rigol, *Scaling of the gap, fidelity susceptibility, and bloch oscillations across the superfluid-to-mott-insulator transition in the one-dimensional bose-hubbard model,* Phys. Rev. A **87**, 043606 (2013).

[168] N. Prokof'ev, B. Svistunov, and I. Tupitsyn, *"worm" algorithm in quantum monte carlo simulations,* Physics Letters A **238**, 253–257 (1998).

[169] K. Sheshadri, H. R. Krishnamurthy, R. Pandit, and T. V. Ramakrishnan, *Superfluid and insulating phases in an interacting-boson model: Mean-field theory and the RPA,* EPL **22**, 257 (1993).

[170] W. Krauth, M. Caffarel, and J.-P. Bouchaud, *Gutzwiller wave function for a model of strongly interacting bosons,* Phys. Rev. B **45**, 3137–3140 (1992).

[171] E. Anderson, Z. Bai, C. Bischof, S. Blackford, J. Demmel, J. Dongarra, J. Du Croz, A. Greenbaum, S. Hammarling, A. McKenney, and D. Sorensen, *LAPACK Users' Guide* (Society for Industrial and Applied Mathematics, Philadelphia, PA, 1999), 3rd ed.

[172] D.-S. Lühmann, *Cluster gutzwiller method for bosonic lattice systems,* Phys. Rev. A **87**, 043619 (2013).

[173] C. Lanczos, *An iteration method for the solution of the eigenvalue problem of linear differential and integral operators,* J. Res. Natl. Bur. Stand. B **45**, 255–282 (1950).

[174] C. Lanczos, *Solution of systems of linear equations by minimized iterations,* J. Res. Nat. Bur. Standards **49**, 33–53 (1952).

[175] D. Calvetti, L. Reichel, and D. C. Sorensen, *An implicitly restarted lanczos method for large symmetric eigenvalue problems,* Electron. Trans. Numer. Anal. **2**, 1–21 (1994).

[176] R. B. Lehoucq, D. C. Sorensen, and C. Yang, *ARPACK: Solution of Large Scale Eigenvalue Problems by Implicitly Restarted Arnoldi Methods*, Available from netlib@ornl.gov (1997).

[177] R. Bai, *Synthetic magnetic fields and multi-component becs in optical lattices,* Ph.D. thesis, Indian Institute of Technology Gandhinagar (2018).

[178] B. Capogrosso-Sansone, i. m. c. G. m. c. Söyler, N. Prokof'ev, and B. Svistunov, *Monte carlo study of the two-dimensional bose-hubbard model,* Phys. Rev. A **77** (2008).

[179] J. Zakrzewski, *Mean-field dynamics of the superfluid-insulator phase transition in a gas of ultracold atoms,* Phys. Rev. A **71**, 043601 (2005).

[180] P. M. Chaikin and T. C. Lubensky, *Principles of Condensed Matter Physics* (Cambridge University Press, 1995).

[181] A. W. Sandvik and J. Kurkijärvi, *Quantum monte carlo simulation method for spin systems,* Phys. Rev. B **43**, 5950–5961 (1991).

[182] A. W. Sandvik, *A generalization of handscomb's quantum monte carlo scheme-application to the 1d hubbard model,* Journal of Physics A: Mathematical and General **25**, 3667 (1992).

[183] P. Henelius and A. W. Sandvik, *Sign problem in monte carlo simulations of frustrated quantum spin systems,* Phys. Rev. B **62**, 1102–1113 (2000).

[184] P. Buonsante, V. Penna, A. Vezzani, and P. B. Blakie, *Mean-field phase diagram of cold lattice bosons in disordered potentials,* Phys. Rev. A **76**, 011602 (2007).

[185] A. W. Sandvik, *Computational Studies of Quantum Spin Systems,* AIP Conference Proceedings **1297**, 135–338 (2010).

[186] J.-H. Jung and J. D. Noh, *Guide to exact diagonalization study of quantum thermalization,* Journal of the Korean Physical Society **76**, 670–683 (2020).

[187] H. Lin, J. Gubernatis, H. Gould, and J. Tobochnik, *Exact Diagonalization Methods for Quantum Systems,* Computer in Physics **7**, 400–407 (1993).

[188] S. Liang, *A perfect hashing function for exact diagonalization of many-body systems of identical particles,* Computer Physics Communications **92**, 11–15 (1995).

[189] Z. Wang, *Quantum basis: Exact diagonalization library for general models, https://github.com/wztzjhn/quantum_basis,* .

[190] A. Ekert and P. L. Knight, *Entangled quantum systems and the Schmidt decomposition,* American Journal of Physics **63**, 415–423 (1995).

[191] A. Kitaev and J. Preskill, *Topological entanglement entropy,* Phys. Rev. Lett. **96**, 110404 (2006).

[192] M. Levin and X.-G. Wen, *Detecting topological order in a ground state wave function,* Phys. Rev. Lett. **96**, 110405 (2006).

[193] J. Eisert, M. Cramer, and M. B. Plenio, *Colloquium: Area laws for the entanglement entropy,* Rev. Mod. Phys. **82**, 277–306 (2010).

[194] L. S. Blackford, J. Choi, A. Cleary, E. D'Azevedo, J. Demmel, I. Dhillon, J. Dongarra, S. Hammarling, G. Henry, A. Petitet, K. Stanley, D. Walker, and R. C. Whaley, *ScaLAPACK Users' Guide* (Society for Industrial and Applied Mathematics, Philadelphia, PA, 1997).

[195] K. Jiménez-García, L. J. LeBlanc, R. A. Williams, M. C. Beeler, A. R. Perry, and I. B. Spielman, *Peierls substitution in an engineered lattice potential,* Phys. Rev. Lett. **108**, 225303 (2012).

[196] P. G. Harper, *Single band motion of conduction electrons in a uniform magnetic field,* Proc. Phys. Soc. A **68**, 874 (1955).

[197] D. Jaksch and P. Zoller, *Creation of effective magnetic fields in optical lattices: the Hofstadter butterfly for cold neutral atoms,* New J. Phys. **5**, 56 (2003).

[198] X. G. Wen and Q. Niu, *Ground-state degeneracy of the fractional quantum hall states in the presence of a random potential and on high-genus riemann surfaces,* Phys. Rev. B **41**, 9377–9396 (1990).

[199] Y. Hatsugai, *Characterization of topological insulators: Chern numbers for ground state multiplet,* Journal of the Physical Society of Japan **74**, 1374–1377 (2005).

[200] K. J. Maschhoff and D. C. Sorensen, *P_arpack: An efficient portable large scale eigenvalue package for distributed memory parallel architectures,* in "Applied Parallel Computing Industrial Computation and Optimization," , J. Waśniewski, J. Dongarra, K. Madsen, and D. Olesen, eds. (Springer Berlin Heidelberg, Berlin, Heidelberg, 1996), pp. 478–486.

[201] Y.-F. Wang, Z.-C. Gu, C.-D. Gong, and D. N. Sheng, *Fractional quantum hall effect of hard-core bosons in topological flat bands,* Phys. Rev. Lett. **107**, 146803 (2011).

[202] N. Regnault and B. A. Bernevig, *Fractional chern insulator,* Phys. Rev. X **1**, 021014 (2011).

[203] H. Miyake, G. A. Siviloglou, C. J. Kennedy, W. C. Burton, and W. Ketterle, *Realizing the Harper Hamiltonian with laser-assisted tunneling in optical lattices,* Phys. Rev. Lett. **111**, 185302 (2013).

[204] M. Atala, M. Aidelsburger, M. Lohse, J. T. Barreiro, B. Paredes, and I. Bloch, *Observation of chiral currents with ultracold atoms in bosonic ladders,* Nature (London) **10**, 588 (2014).

[205] C. J. Kennedy, W. C. Burton, W. C. Chung, and W. Ketterle, *Observation of Bose-Einstein condensation in a strong synthetic magnetic field,* Nature (London) **11**, 859 (2015).

[206] E. H. Rezayi, N. Read, and N. R. Cooper, *Incompressible liquid state of rapidly rotating bosons at filling factor* $3/2$*,* Phys. Rev. Lett. **95**, 160404 (2005).

[207] T. Yoshida, K. Kudo, and Y. Hatsugai, *Non-hermitian fractional quantum hall states,* Scientific Reports **9** (2019).

[208] T. Yoshida, K. Kudo, H. Katsura, and Y. Hatsugai, *Fate of fractional quantum hall states in open quantum systems: Characterization of correlated topological states for the full liouvillian,* Phys. Rev. Res. **2**, 033428 (2020).

[209] Z. Liu, E. J. Bergholtz, and J. C. Budich, *Dissipative preparation of fractional chern insulators,* Phys. Rev. Res. **3**, 043119 (2021).

[210] H. Z. Shen, M. Qin, and X. X. Yi, *Single-photon storing in coupled non-markovian atom-cavity system,* Phys. Rev. A **88**, 033835 (2013).

[211] R. Zhang, T. Chen, and X.-B. Wang, *Deterministic quantum controlled-phase gates based on non-markovian environments,* New Journal of Physics **19**, 123001 (2017).

[212] H.-P. Breuer and F. Petruccione, *The Theory of Open Quantum Systems* (Oxford University Press, 2007).

[213] H.-P. Breuer, E.-M. Laine, J. Piilo, and B. Vacchini, *Colloquium: Non-markovian dynamics in open quantum systems,* Rev. Mod. Phys. **88**, 021002 (2016).

[214] D. A. Abanin, E. Altman, I. Bloch, and M. Serbyn, *Colloquium: Many-body localization, thermalization, and entanglement,* Rev. Mod. Phys. **91**, 021001 (2019).

[215] H. Nishimori and G. Oritz, *Elements of Phase Transitions and Critical Phenomena* (Oxford University Press (Oxford), 2010).

[216] W. Zurek, *Cosmological experiments in condensed matter systems,* Physics Reports **276**, 177 (1996).

[217] B. Damski and W. H. Zurek, *Adiabatic-impulse approximation for avoided level crossings: From phase-transition dynamics to landau-zener evolutions and back again,* Phys. Rev. A **73**, 063405 (2006).

[218] G. Biroli, L. F. Cugliandolo, and A. Sicilia, *Kibble-zurek mechanism and infinitely slow annealing through critical points,* Phys. Rev. E **81**, 050101 (2010).

[219] K. Jeong, B. Kim, and S. J. Lee, *Growth kinetics of the two-dimensional ising model with finite cooling rates,* Phys. Rev. E **99**, 022113 (2019).

[220] K. Roychowdhury, R. Moessner, and A. Das, *Dynamics and correlations at a quantum phase transition beyond kibble-zurek,* Phys. Rev. B **104**, 014406 (2021).

[221] J. Dziarmaga, M. Tylutki, and W. H. Zurek, *Quench from mott insulator to superfluid,* Phys. Rev. B **86**, 144521 (2012).

[222] W. Weiss, M. Gerster, D. Jaschke, P. Silvi, and S. Montangero, *Kibble-zurek scaling of the one-dimensional bose-hubbard model at finite temperatures,* Phys. Rev. A **98**, 063601 (2018).

[223] H. Sable, D. Gaur, S. Bandyopadhyay, R. Nath, and D. Angom, *Quantum quench dynamics of tilted dipolar bosons in 2d optical lattices,* arXiv:2106.01725v2 (2021).

[224] H. Sable, D. Gaur, and D. Angom, *Fine-grained domain counting and percolation analysis in 2d lattice systems with linked-lists,* arXiv:2112.15527 (2021).

[225] P. kaur, K. Suthar, D. Angom, and S. Gautam, *Out-of-equilibrium dynamics of bose-bose mixtures in optical lattices,* arXiv:2307.13057 (2023).

List of Publications

Thesis related Publications

1. **Deepak Gaur**, Hrushikesh Sable, and D. Angom,
   Fractional quantum Hall effect in optical lattices,
   Frontiers in Physics **10**, 1106491 (2023).
   doi: 10.3389/fphy.2022.1106491

2. **Deepak Gaur**, Hrushikesh Sable, and D. Angom,
   Exact-diagonalization method for characterization of topological entanglement in lattice systems using hierarchical wavefunctions, (under review)
   arXiv:2308.07147.
   10.48550/arXiv.2308.07147

3. **Deepak Gaur**, Hrushikesh Sable, and D. Angom,
   Quench dynamics across the MI-SF quantum phase transition with cluster mean field theory,
   arXiv:2309.06272.
   10.48550/arXiv.2309.06272

Other Publications

1. Hrushikesh Sable, **Deepak Gaur**, and D. Angom,
   Fine-grained domain counting and percolation analysis in 2D lattice systems with linked-lists,
   Phys. Rev. E **108**, 045307 (2023).
   doi: 10.1103/PhysRevE.108.045307

2. Soumik Bandyopadhyay, Hrushikesh Sable, **Deepak Gaur**, Rukmani Bai, Subroto Mukerjee, and D. Angom,
   Quantum phases of dipolar bosons in a multilayer optical lattice,
   Phys. Rev. A **106**, 043301 (2022).
   doi: 10.1103/PhysRevA.106.043301

3. Rukmani Bai, **Deepak Gaur**, Hrushikesh Sable, Soumik Bandyopadhyay, K. Suthar, and D. Angom,
   Segregated quantum phases of dipolar bosonic mixtures in two-dimensional optical lattices,
   Phys. Rev. A **102**,043309 (2020).
   doi: 10.1103/PhysRevA.102.043309

4. Hrushikesh Sable, **Deepak Gaur**, Soumik Bandyopadhyay, Rejish Nath, and D. Angom,
   Quantum quench dynamics of tilted dipolar bosons in 2D optical lattices,
   arXiv:2106.01725.
   10.48550/arXiv.2106.01725